Copyright
by
Bruce George Klappauf
1998

EXPERIMENTAL STUDIES OF QUANTUM CHAOS WITH TRAPPED CESIUM

by

BRUCE GEORGE KLAPPAUF, B.S.

DISSERTATION

Presented to the Faculty of the Graduate School of
The University of Texas at Austin
in Partial Fulfillment
of the Requirements
for the Degree of

Doctor of Philosophy

THE UNIVERSITY OF TEXAS AT AUSTIN
December 1998

EXPERIMENTAL STUDIES OF QUANTUM CHAOS WITH TRAPPED CESIUM

APPROVED BY
DISSERTATION COMMITTEE:

Supervisor: ______________________________

____

____

____

____

Dedicated my parents for their never ending support no matter what.

Acknowledgments

I am very grateful to have had the good fortune of working in the Atom Optics Laboratory of Mark Raizen at the University of Texas. Mark's dedication not only to physics, but to his family, his students, and the physics department provided both inspiration and challenge. His enthusiasm has provided this lab with a constant supply of both the creative and material wealth necessary for the tremendous success we've all enjoyed.

One Mark's most important talents is his ability to hire talented people who can work together pleasantly and fruitfully. Though we often joke about not having a life as grad students, my coworkers in this lab have been a constant source of support, entertainment, and professional collaboration. I would like to thank Pat Morrow who got me started in this lab, and taught me the in's and out's of daily lab operation. I would also like to thank John Robinson who provided a wonderful example to follow as a person and a physicist, as well as patient and endless help. Our postdoc Fred Moore not only was an amazing experimentalist with an uncanny intuition for physics, but he could sometimes beat me at pool.

Two of my contemporaries worked on *the other experiment*, but became great friends. Cyrus Bharucha had a wonderful ability to organize a variety of complex physical concepts into simple and intuitive packages. He was always ready to help and cheerfully at that. Kirk Madison could take the best notes in the world. But more than that he was always able to come away from any talk with the basic concepts of the subject, and his own connections to other topics in physics. I feel very fortunate that he found time for me both in and out of the lab. He is a unique individual, and a good friend.

This success of these experiments would not have been possible without the tireless help of two amazing individuals who worked with me on building this experiment.

Dan Steck is the most talented and productive student I have known. He has an ever expanding wealth of knowledge, and is always willing to share when asked. He is responsible for most of the theoretical background we've uncovered, all of the simulations we present, and many of the experimental designs we used. His patient explanations of physics, music, electronics, and how to kill basil plants have helped me tremendously. He will go far.

Windell Oskay never sleeps. Much. This may explain his amazing volume and variety of successful endeavors. In the lab he is always ready and eager to do what ever is necessary to improve the lab and advance the experiment, and he takes it on himself to do so. He handled almost all of our computer automation and did a fantastic job. In addition to his classes, teaching, and research, he is an award winning cartoonist, musician, inventor, artist, chef, and rebel leader. He also fancies coffee now and then.

Several other people have made important contributions as well. Steve Wilkinson was a great help in starting our Ti:sapphire laser project, and graciously accepted defeat by the Packers. Martin Fischer has my appreciation for answering so many off-the-cuff questions, and for adding solidarity to the PC faction of our lab. Finally I would like to thank Valery Milner, our new postdoc, for the energetic contributions he has already made, both in the lab and on the rocks.

Many others have come through the lab and I would like to thank them all for their contributions to my life and work here.

EXPERIMENTAL STUDIES OF QUANTUM CHAOS WITH TRAPPED CESIUM

Publication No. ____________________

Bruce George Klappauf, Ph.D.
The University of Texas at Austin, 1998

Supervisor: Mark Raizen

This dissertation describes experimental studies of quantum chaos with trapped atoms in a time-dependent dipole potential. Our starting point is the use of a pulsed standing wave of light to generate an experimental realization of the quantum kicked rotor. The classical counterpart of this system, the delta-kicked rotor is a paradigm for the study of chaotic dynamics, and this quantum realization allows us to study the correspondence between quantum and classical behavior under a variety of conditions. The generality of this system makes our research important to the fundamental understanding of quantum mechanics. This work also provides an experimental connection to the wealth of theoretical and numerical studies in chaos and quantum chaos, and we hope it will inspire new directions for future work.

The first of our three experiments characterizes the *momentum boundary*, a classical limit on momentum growth due to the non-zero pulse width of any real system. Since our primary measurement in these experiments consists of the momentum distribution of atoms after an interaction with the standing wave, it is important to understand this boundary.

The second experiment studies the effects of noise and dissipation on the quantum kicked rotor. It is well accepted that the quantum version of this system exhibits a suppression of the diffusive energy growth that characterizes the classical behavior. This coherent quantum effect is known as *dynamical localization*, and theoretical predictions suggest that noise added to the quantum system may destroy this effect, driving the system back toward the classical limit. We present experimental evidence to support these predictions.

Finally, we study the quantum dynamics of the kicked rotor as a function of the interaction strength and the kicking frequency. The classical system exhibits an oscillatory dependence of the momentum diffusion on the interaction strength and, for certain parameters, exhibits *anomalous diffusion.* Our results show a similar oscillatory dependence on the interaction strength, and an additional dependence, predicted for the quantum case, on the kicking frequency. We also observe an unpredicted qualitative variation in the momentum distributions near those parameters exhibiting classical anomalous diffusion.

Table of Contents

Acknowledgments **v**

Abstract **viii**

List of Tables **xii**

List of Figures **xiii**

Chapter 1. Introduction **1**
1.1 Background 1
1.2 Atoms in a Standing Wave of light 5
  1.2.1 The Coherent Interaction 5
  1.2.2 The Incoherent Interaction 8
  1.2.3 Natural Units 9
1.3 Chaos and the Kicked Rotor 15
  1.3.1 The Pendulum Phase Space 15
  1.3.2 The Perturbed Pendulum 18
  1.3.3 The Delta-Kicked Rotor 22
1.4 Quantum Chaos 28

Chapter 2. Experimental Method **32**
2.1 Introduction 32
2.2 The Cesium Chamber 34
2.3 The MOT Lasers 40
  2.3.1 The Trapping Laser 40
  2.3.2 The Repump Laser 44
2.4 The Interaction Laser 52
2.5 Measurement 56
  2.5.1 Initial Conditions 56

2.5.2 Interaction 60
2.5.3 Free Drift 67
2.5.4 Imaging 68
2.6 Computer Control 71

Chapter 3. Pushing Back the Boundaries 75
3.1 Introduction 75
3.2 Classical Analysis of the Momentum Boundary 77
3.3 Experimental Parameters 83
3.4 Results 85

Chapter 4. Noise and Dissipation 92
4.1 Introduction 92
4.2 Experimental Parameters 93
4.3 Results 95

Chapter 5. Anomalous Diffusion 101
5.1 Introduction 101
5.2 Theory and Background 102
5.3 Experimental Parameters 109
5.4 Results 110

Bibliography 114

Vita 122

List of Tables

2.1 DBR Data 41
2.2 Repump Diode Data 46
2.3 Gold Coating Data 47

4.1 Fit results for noise data 99

List of Figures

1.1 Hyperfine stucture for the cesium D_2 line 10
1.2 Energy band structure versus well depth 14
1.3 Classical pendulum phase space 16
1.4 Classical pendulum surface of section 20
1.5 Delta-kicked rotor surface of section for K=1 21
1.6 Physical model for the DKR 23
1.7 Evolution of DKR phase space as a function of K 26
1.8 Characteristics of classical diffusion 27
1.9 Depiction of typical signatures of dynamical localization . . . 29

2.1 Schematic diagram of the experimental setup 33
2.2 Picture of UHV chamber 35
2.3 Schematic for anti-Helmholtz coil current driver 37
2.4 Oscilloscope trace of magnetic field ring down 38
2.5 Picture of cesium ampoule 39
2.6 FM lock setup 42
2.7 Picture of grating stabilized laser for repumping 45
2.8 CAD drawings of grating stabilized diode laser 50
2.9 Diagram of saturated absorbtion lock 51
2.10 Diagram Ti:sapphire laser cavity 55
2.11 Drawings of design for Ti:sapphire crystal mount 55
2.12 Measurement sequence 57
2.13 Initial conditions comparison to Gausssian 58
2.14 Example of a LabVIEW temperature measurement 59
2.15 Example of actual pulse profile for delta kick 61
2.16 Example of knife edge program 64
2.17 Beam profile program 65
2.18 CCD images 70

2.19 Computer control diagram 72
2.20 Timing diagram 74

3.1 Comparison of sodium data to cesium data 76
3.2 Graph of K_{eff} versus momentum 78
3.3 Phase space comparison for finite pulse kicked rotor and DKR 80
3.4 Simulations of finite pulse distributions 82
3.5 Experimental time evolution for DKR momentum distributions 86
3.6 Comparison of momentum distributions for different pulsewidths 87
3.7 Overlay comparison of 2 distributions 88
3.8 Comparison of energy growth versus boundary 89
3.9 Comparison of simulation to experiment 90

4.1 Pulse sequence for amplitude noise 94
4.2 Comparision of momentum distributions with noise 96
4.3 Graph of increased energy growth due to noise 97

5.1 DKR surface of section with accelerator modes 104
5.2 Simulation of a single particle DKR trajectory showing Levy flights 105
5.3 Simulations of D(K) 107
5.4 Comparison of momentum distributions near diffusion peaks . 111
5.5 Energy versus K_q for different $\not{k}$ 112

Chapter 1

Introduction

1.1 Background

In the mid-1980's a great deal of interest developed in looking at the interaction of atoms with a standing wave of light. This primarily involved studying the interaction itself, and atomic analogues of optical scattering effects [1, 2, 3, 4]. In 1992 it was recognized by Graham *et al.*[5] that for sufficiently far detuning, the dipole potential of the standing wave could produce a versatile conservative interaction potential for the atoms, which could be used to take this research in a new direction: quantum chaos.

The proposed experiment was for an atomic beam passing through a far-detuned, modulated standing wave. The dipole interaction with the modulated standing wave was shown to be mathematically equivalent to the periodically driven pendulum, one of the classically chaotic systems used theoretically to develop the emerging field of quantum chaos. The key to studying coherent quantum evolution over long times with the standing wave was that the rate of incoherent scattering could be made arbitrarily small, given enough laser power.

Shortly thereafter, the research group of Mark Raizen (at the University of Texas) realized that they could go one step further, by using ultra-cold atoms from a *magneto-optic trap* (MOT) rather than an atomic beam [6]. This allowed the atoms to experience the more uniform intensity at the center of the laser beam for the entire interaction, rather than traversing the beam during the interaction. The time-of-flight momentum measurement could still be accomplished by simply imaging the atoms after a free expansion. The cold atom approach also opened the door for much longer, well defined, and easily controlled interaction times, up to milliseconds in the latest series of experiments. The first series of experiments used trapped sodium, and demonstrated several important quantum phenomena predicted for these systems [7, 8].

The first of these effects, studied with a phase-modulated standing wave, was dynamical localization. This effect is a quantum suppression of classical diffusion predicted for several quantum systems whose classical dynamics exhibit chaotic behavior. A control parameter in the modulated standing wave allowed the system to be continuously varied from a regime where the classical dynamics are nearly integrable, to one where they are chaotic, allowing the study of the transition to chaos [6, 9]. The next experiment realized one of the simplest and most important systems for the study of classical chaos and quantum chaos, the delta-kicked rotor (DKR). Dynamical localization was again observed in this system, and in addition, the group went on to demonstrate and begin analysis of another quantum effect inherent in this realization of the DKR, quantum resonances [10]. Finally, the group was able to test the resonance overlap criterion for the onset of global stochasticity by studying the effects of applying just a single temporal pulse of the standing wave as a function of the pulse duration [11].

Subsequent sodium experiments involved exploring the detailed band structure and tunneling properties of atoms in an accelerating periodic optical potential [12]. These experiments, and the chaos experiments, advanced the understanding of momentum transfer to atoms in an optical lattice. However, they also demonstrated the utility of this experimental system for studying both general properties of periodic lattices, which relate to solid state problems, and for studying the relationship between quantum and classical chaos, which is being found in an ever increasing number of problems. The work described in this dissertation represents a continuation of the work on quantum chaos that began with the earlier experiment, this time focusing on our quantum realization of the delta-kicked rotor.

Due to a variety of technical limitations with the original sodium experiment, we have built a new experiment using cesium atoms instead of sodium. Chapter 2 describes the new experimental apparatus and control systems. One immediate benefit of this change was that the wavelength of the cesium transition used is readily accessible by currently available diode lasers. These proved to be more efficient in terms of table space, energy, alignment time, and cost as compared with the argon-pumped dye lasers required by the sodium experiment.

The primary limitation of the sodium experiment that prompted this change was related to pulses themselves. Our experimental approximation to a "delta-kick" has a non-zero pulse width which limits the maximum momentum that can be transferred to the atoms [13]. This limitation, which places a momentum *boundary* in phase space that depends on mass and wavelength, is reduced in cesium. The effects of this issue are studied in Chapter 3.

After characterizing the effect of the boundary, and having verified our ability to again observe localization, we began to study the effects of applying amplitude noise to the kicks and of inducing a controlled level of spontaneous emission [14]. Theoretically, it was believed that either of these perturbations should destroy the coherent quantum evolution necessary for dynamical localization. It has also been suggested that sufficient decoherence might drive the system back to its classical behavior, despite the very quantum regime in which we operate (the relevant phase space structures are small relative to $\hbar$). These results are presented in Chapter 4.

Finally, in Chapter 5 we consider more detailed structures in the phase space, and study what effects these have on the global transport properties of the system. One of the most striking and unique features of the DKR system is the existence of resonant stable structures called *accelerator modes.* These features have a dramatic effect on momentum transport, causing anomalous diffusion of the momentum distribution in phase space when they are present. The occurence accelerator modes appears to be related to the periodic variation of the momentum diffusion rate with the strength of the delta kicks. While this is a classical effect, we have observed very similar oscillations in our quantum system. However, in this case the oscillation period depends also on the relative size of the phase space structure to $\hbar$, the quantum unit of phase space volume [15]. This dependence was predicted by Shepelyansky in 1987 [16].

As we stated in the beginning, these studies of the quantum behavior of a simple classically chaotic system are made possible by the ability to generate a non-dissipative, spatially periodic dipole force in a far-detuned standing wave of light, in which we can treat the atom as a point particle in a classical sinusoidal potential. Thus, our starting point is a quantum pendulum, the details of which are outlined in the Section 1.2. The connection to quantum chaos is made in Sections 1.3 and 1.4.

1.2 Atoms in a Standing Wave of light

The physics of an atom in a standing wave of light is central to all of the work discussed here. In general there is both coherent (stimulated), and incoherent (spontaneous) scattering of the photons by atoms. The spontaneous scattering is used primarily for the trapping and cooling of the atoms via the near-resonant optical molasses and MOT beams [7, 17, 18]. The description of the coherent interaction, which generates the dipole potential, was sketched out by Graham *et al.* [5], and has been presented in iteratively more detail in subsequent work [7, 19, 8, 12, 20]. Here we present some of the main points of the coherent and incoherent interaction, and then discuss the relevant units and scales.

1.2.1 The Coherent Interaction

For now we assume a two-level atom with ground and excited states labeled $|g\rangle$ and $|e\rangle$ respectively, separated by energy $\hbar\omega_0$. This interacts with a standing wave formed by two linearly polarized, counterpropagating laser beams, each with frequency ω_{L} and propagation vectors corresponding to $\pm k_{\mathrm{L}}$. Assuming a plane wave approximation at the center of the beams, this gives an electric field of the form

$$\mathbf{E}(x,t) = \hat{\mathbf{z}}\, E_1 \cos(k_{\mathrm{L}}x - \omega_{\mathrm{L}}t) + \hat{\mathbf{z}}\, E_2 \cos(k_{\mathrm{L}}x + \omega_{\mathrm{L}}t). \tag{1.1}$$

In the ideal case where $E_1 = E_2 = E_0$, we have

$$\mathbf{E}(x,t) = \hat{\mathbf{z}}\, E_0 \cos(k_{\mathrm{L}}x)(e^{+i\omega_{\mathrm{L}}t} + e^{-i\omega_{\mathrm{L}}t}), \tag{1.2}$$

resulting in an intensity standing wave given by

$$I(x) = \epsilon_0 c \,\langle \mathbf{E}\cdot\mathbf{E}\rangle = \frac{\epsilon_0 c E_0^2}{2}\left[1 + \cos(2k_{\mathrm{L}}x)\right]. \tag{1.3}$$

This one-dimensional field, in the absence of inelastic scattering by the atoms, can only transfer momentum to the atom in units of two photon recoils. That is, it absorbs a photon and its momentum from one beam, and emits it into the opposite beam. The recoil in momentum given to the atom is then

$$\Delta \mathbf{p} = \pm \hat{\mathbf{x}}\, 2\hbar k_{\mathrm{L}}. \tag{1.4}$$

Because of this well-defined unit of momentum, it is useful to define a unit of frequency (and energy) which corresponds to the kinetic energy from one photon recoil. Given in terms of the wave number, the energy is

$$\hbar\omega_{\mathrm{r}} = \hbar \left(\frac{\hbar k_{\mathrm{L}}^2}{2M} \right), \tag{1.5}$$

where ω_{r} is called the *recoil frequency*. The recoil frequency depends on both the atomic mass and the transition frequency. For the cesium D_2 line,

$$\omega_{\mathrm{r}} \cong 2\pi \times 2.066 \text{ kHz}, \tag{1.6}$$

which is the value that will apply in all of our work.

The Hamiltonian for the atom can be broken up into three parts given by

$$H = H_{\mathrm{cm}} + H_{\mathrm{internal}} + H_{\mathrm{interaction}}, \tag{1.7}$$

where

$$\begin{aligned} H_{\mathrm{cm}} &= \frac{p^2}{2M}, && (1.8) \\ H_{\mathrm{internal}} &= \hbar\omega_0 |\mathrm{e}\rangle\langle \mathrm{e}|, && (1.9) \end{aligned}$$

and

$$H_{\mathrm{interaction}} = -e\mathbf{r}'_{\mathrm{e}} \cdot \mathbf{E}(\mathbf{r}_{\mathrm{e}}, t) = -\mathbf{d} \cdot \mathbf{E}(\mathbf{r}_{\mathrm{e}}, t). \tag{1.10}$$

In these equations p is the atomic center-of-mass momentum, $\mathbf{r}'_\mathrm{e}$ is the electron position relative to the atom, $\mathbf{r}_\mathrm{e}$ is the electron position relative to the field, and $\mathbf{d}$ is the dipole operator. In the dipole approximation the electron displacement $\mathbf{r}'_\mathrm{e}$ is small compared to the wavelength of the the interacting field $\mathbf{E}$. Therefore, we can evaluate $\mathbf{E}$ at the center of mass position of the atom, $\mathbf{r}$, and write the dipole moment in terms of the internal atomic state. The dot product yields the z component d_z of the dipole moment and we have the interaction term

$$\begin{aligned} -e\mathbf{r}_\mathrm{e}\cdot\mathbf{E}(\mathbf{r},t) &= \frac{-|\langle\mathrm{e}|d_\mathrm{z}|\mathrm{g}\rangle|E_0}{2}\cos(k_\mathrm{L}x)(a^\dagger e^{+i\omega_\mathrm{L}t}+ae^{-i\omega_\mathrm{L}t}) \qquad (1.11)\\ &= \frac{-d\,E_0}{2}\cos(k_\mathrm{L}x)(a^\dagger e^{+i\omega_\mathrm{L}t}+ae^{-i\omega_\mathrm{L}t}), \qquad (1.12)\end{aligned}$$

where $a \equiv |\mathrm{g}\rangle\langle\mathrm{e}|$ is the atomic lowering operator, and d is the dipole matrix element shown in Eq. (1.11).

With the definition of the maximum resonant Rabi frequency as

$$\Omega_0 \equiv -\frac{2dE_0}{\hbar}, \qquad (1.13)$$

we have

$$H = \frac{p^2}{2M} + \hbar\omega_0|\mathrm{e}\rangle\langle\mathrm{e}| + \frac{\hbar\Omega_0}{2}\cos(k_\mathrm{L}x)(a^\dagger e^{+i\omega_\mathrm{L}t}+ae^{-i\omega_\mathrm{L}t}). \qquad (1.14)$$

This Hamiltonian can be cast into a simpler form by a series of manipulations presented in the references above. We substitute it into Schrödinger's equation and apply the rotating wave approximation to remove the terms at optical frequencies. We may also adiabatically eliminate the excited state amplitude in the limit of large detuning from resonance. We then make the definition

$$V_0 \equiv \frac{\hbar\Omega_0^2}{8\Delta_\mathrm{L}} = \frac{d^2E_0^2}{2\hbar\Delta_\mathrm{L}}, \qquad (1.15)$$

where $\Delta_\mathrm{L} \equiv \omega_\mathrm{L} - \omega_0$ is the detuning from the atomic resonance. Finally, we have the resulting autonomous Hamiltonian

$$H = \frac{p^2}{2M} + V_0\cos(2k_\mathrm{L}x). \qquad (1.16)$$

This is the Hamiltonian for a pendulum.

The equation for V_0 is valid for cesium, despite the fact that cesium is far from being a two level atom. We simply need to be careful how we determine the dipole coupling. This is described in the next section. Also, if the counterpropagating lasers have different intensities, then the E_0^2 in the definition of V_0 can be replaced by E_1E_2 as defined in Eq. (1.1).

1.2.2 The Incoherent Interaction

In order to include spontaneous emission in our treatment we need to replace the Schrödinger equation with the optical Bloch equations, including a dissipation term involving the radiative lifetime Γ [21]. The resulting scattering rate for a two level atom is

$$R_{\mathrm{sc}} = \left(\frac{\Gamma}{2}\right) \frac{(I/I_{\mathrm{sat}})}{1 + 4(\Delta_{\mathrm{L}}/\Gamma)^2 + (I/I_{\mathrm{sat}})}, \tag{1.17}$$

where

$$I_{\mathrm{sat}} = \frac{c\epsilon_0 \Gamma^2 \hbar^2}{4d^2} \tag{1.18}$$

is the saturation intensity.

The hyperfine structure of cesium, shown in Fig. 1.1, is far from a two level atom. In fact, there is a different coupling to each hyperfine sublevel, which is contained in the dipole moment within I_{sat}. This means that the saturation intensity depends both on the polarization of the driving light, and the hyperfine population distribution of the atoms. Nonetheless, we can see from this equation that if the driving light is far enough detuned, the coupling term in the denominator is irrelevant. If, in addition, the detuning is much larger than the hyperfine splitting, then $(\Delta_{\mathrm{L}}/\Gamma)$ in the denominator will be roughly the same for each hyperfine excited state F'. Therefore we can add up all of the contributions from all of the relevant transitions from a given ground state $|F\,m\rangle$ to get an overall scattering rate

$$R_{\mathrm{sc}} = \left(\frac{\Gamma}{2}\right) \frac{I\left(\frac{4}{c\epsilon_0\Gamma^2\hbar^2}\right)\sum\limits_{F'm'}|\hat{\epsilon}\cdot\mathbf{d}_{F,m,F'm'}|^2}{4(\Delta_{\mathrm{L}}/\Gamma)^2}. \tag{1.19}$$

For far-detuned, linearly polarized light, $|\hat{\epsilon}\cdot\mathbf{d}|^2 = d^2$, and only the $m = m'$ states couple. By a happy property of the dipole operator, the sum over the excited F' states for any given ground state $|F\,m\rangle$ is a constant, independent of m. This constant is given by

$$d^2 = \frac{1}{3}|\langle J\|e\mathbf{r}\|J'\rangle|^2, \tag{1.20}$$

where $|\langle J\|e\mathbf{r}\|J'\rangle|$ is the $J \longrightarrow J'$ reduced dipole operator that is determined from lifetime measurements by

$$\frac{1}{\tau} = \frac{\omega^3}{3\pi\epsilon_0\hbar c^3}\frac{2J+1}{2J'+1}|\langle J\|e\mathbf{r}\|J'\rangle|^2. \tag{1.21}$$

The resulting values of d and I_{sat} for our far-detuned interaction transition, $(6\mathrm{S}_{1/2}, F = 4) \longrightarrow (6\mathrm{P}_{3/2}, F' = 3, 4, 5)$, are given by

$$d = 2.19\times10^{-29}\ \mathrm{C{\cdot}m} \qquad \text{and} \qquad I_{\mathrm{sat}} = 1.65\ \mathrm{mW/cm^2}. \tag{1.22}$$

These are the same values that determine the coherent interaction strength in Eq. (1.15).

1.2.3 Natural Units

Now a word about units. As appealing as it is to use "real" MKS units, the standing wave Hamiltonian lends itself nicely to a set of "natural" dimensionless variables, obtained from a set of natural units. The main advantage of the natural units is that they restate our problem in a language that is independent

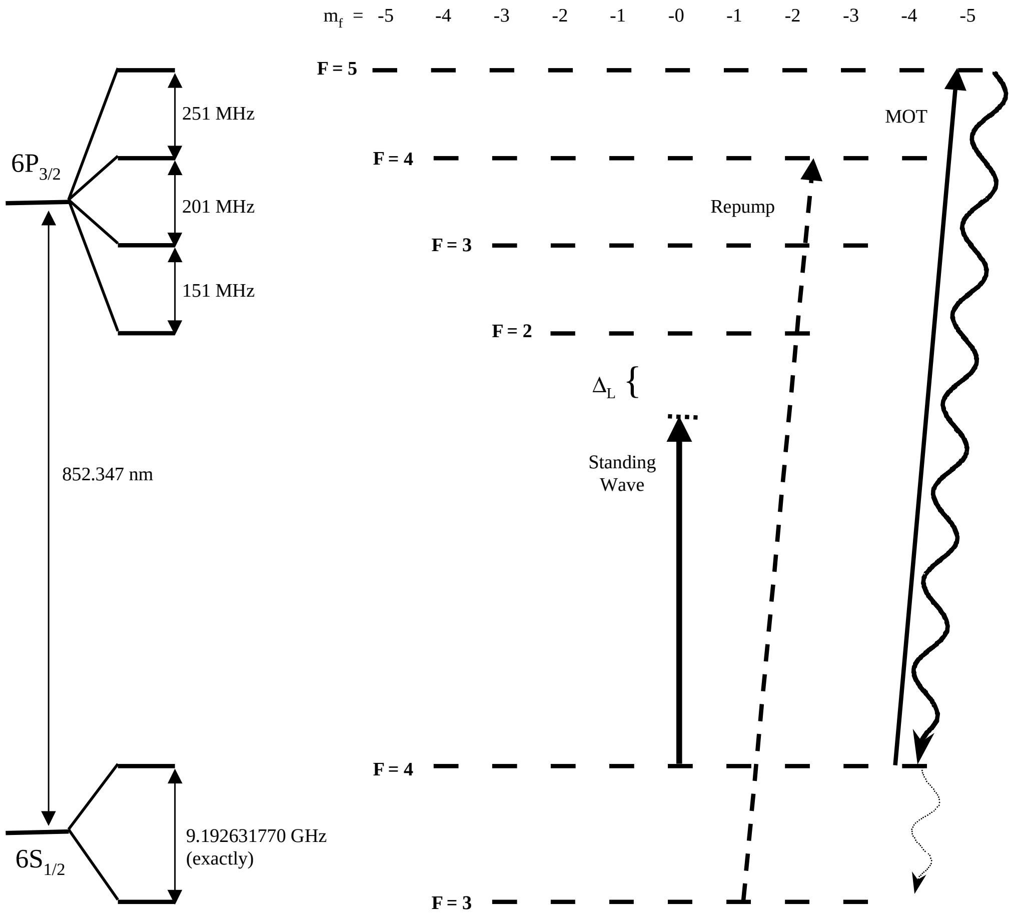
m_f = -5 -4 -3 -2 -1 -0 -1 -2 -3 -4 -5
F = 5
F = 4
F = 3
F = 2
F = 4
F = 3
$6P_{3/2}$
$6S_{1/2}$
251 MHz
201 MHz
151 MHz
852.347 nm
9.192631770 GHz
(exactly)
MOT
Repump
Δ_L {
Standing
Wave

Figure 1.1: Hyperfine stucture for the cesium D_2 line

of our particular experimental setup. This facilitates communication and collaboration with other interested parties, theorists and experimentalists alike. Also, it makes the equations a little simpler, and eliminates five experimental parameters $(T, M, k_{\mathrm{L}}, \omega_{\mathrm{r}}, \hbar)$, to leave only two dimensionless parameters, κ and $\bar{k}$, which determine all of the dynamics for the ideal delta-kicked rotor.

I will reiterate the unit conversions decribed in previous work, adjusted for our cesium experiment, and elaborate on some of the especially relevant scaling factors [8, 12]. The basic units we are interested in will be labeled with the subscript “u”.

t_u	$\equiv$	T	time unit	T is some natural time period of the system.
d_u	$\equiv$	$\dfrac{1}{2k_\mathrm{L}}$	distance unit	This is $1/2\pi$ times the spatial period ($\lambda/2$) of the standing wave.
M_u	$\equiv$	M_atom	mass unit	Mass of the atom

The following units are derived from those above.

p_u	$\equiv$	$M_\mathrm{u}\dfrac{d_\mathrm{u}}{t_\mathrm{u}}$	momentum unit
E_u	$\equiv$	$\dfrac{{p_\mathrm{u}}^2}{M_\mathrm{u}}$	energy unit
$\hbar_\mathrm{u}$	$\equiv$	$d_\mathrm{u}p_\mathrm{u}$	phase space volume unit

With these we make the conversion to the scaled, dimensionless variables.

$$\begin{aligned}
\tau &\equiv \frac{t}{t_\mathrm{u}} \\
\phi &\equiv \frac{x}{d_\mathrm{u}} = 2k_\mathrm{L}x \\
\mu &\equiv \frac{M}{M_\mathrm{u}} = 1 \\
\rho &\equiv \frac{p}{p_\mathrm{u}} = \frac{p}{2\hbar k_\mathrm{L}}\bar{k} \\
\mathcal{E} &\equiv \frac{E}{E_\mathrm{u}} = \frac{E}{8\hbar\omega_\mathrm{r}}\bar{k}^2 \\
\kappa &\equiv \frac{V_0}{E_\mathrm{u}} \\
\mathcal{H} &\equiv \frac{\mathrm{H}}{E_\mathrm{u}} \\
\bar{k} &\equiv \frac{\hbar}{\hbar_\mathrm{u}} = 8\omega_\mathrm{r}t_\mathrm{u} \qquad (1.23)
\end{aligned}$$

Now, by substitution Eq. (1.16) becomes

$$\mathcal{H} = \frac{\rho^2}{2} + \kappa\cos(\phi), \tag{1.24}$$

resulting in the simplified classical equations of motion

$$\dot{\phi} = \frac{\partial\mathcal{H}}{\partial\rho} = \rho \quad \text{and} \quad \dot{\rho} = \frac{-\partial\mathcal{H}}{\partial\phi} = \kappa\sin(\phi). \tag{1.25}$$

The term *well depth* usually refers to the value of 2κ or $2V_0$, since this is the the energy at the separatrix, below which particles would be classically bound.

Notice the effect of the choice of time unit. This scales the momentum, the energy, and the phase space volume. Although this scaling sometimes distorts our intuition of the system when connecting it to experimental parameters, it has a very useful consequence in the quantum mechanical interpretation of the variables. Now the quantum commutators will depend on the quantity $\bar{k}$, such that

$$[\phi, \rho] = [\tau, \mathcal{H}] = i\bar{k}. \tag{1.26}$$

Thus $\bar{k}$, and hence, the chosen unit of time, determine the quantum scale of the phase space, and the size of a minimum uncertainty state. Typically, T will correspond to some periodic drive in the potential that we can control. Therefore, in terms of the correspondence principle, we can control the degree to which our system should be more quantum or more classical by changing T, and thus changing $\bar{k}$. This study of the correspondence between classical and quantum behavior, especially in the context of chaos, decoherence, and its dependence on the quantum scaling, is at the heart of this research.

For the case of the pendulum, there is no single time scale to use. In fact, this is one of the important properties of the pendulum; it has a wide spectrum of oscillation frequencies. Therefore, for the pendulum and other such cases where there is no obvious characteristic timescale, it is convenient to choose $T = 1/8\omega_{\mathrm{r}}$ so that $\bar{k} = 1$. For cesium this sets the following natural units, which gives an indication of the scales involved.

$$\begin{aligned}
t_{\mathrm{u}} &= 9.63\ \mu\mathrm{s} \\
2\pi x_{\mathrm{u}} &= 426\ \mathrm{nm}\ * \\
M_{\mathrm{u}} &= 132.905\ \mathrm{amu}\ * \\
p_{\mathrm{u}} &= M\ 7.0\ \mathrm{mm/s}{=}\ M{\times}\text{two photon recoil velocities} \\
E_{\mathrm{u}} &= 16.531\ \mathrm{kHz}\ \cdot h = 6.834 \times 10^{-11}\ \mathrm{eV} \\
\bar{k} &= 1 \qquad (1.27) \\
&* \quad \text{independent of the choice of time unit}
\end{aligned}$$

Typically our interaction beam can attain peak intensities of 8.5 W/cm^2, and detunings of $\Delta_{\mathrm{L}}/2\pi \sim 6$ GHz. This generates the following well depths:

$$\begin{aligned}
2V_0 &= 4.8 \times 10^{-8}\ \mathrm{eV} = 1.2 \times 10^4\ \mathrm{kHz}\ \cdot h \\
2\kappa &= 700.
\end{aligned}$$

For this well depth, the libration period for the ground state of the well is about 0.33 $t_{\mathrm{u}} = 3.2\ \mu$s. The frequency is $\omega = \sqrt{\kappa} = 18.7$, corresponding to 300 kHz, which means that if this were a harmonic well we would have more than 37 bound states (up to the well depth). Even though quantum mechanically the states near the separatrix break up into bands as the transition to the continuous energy spectrum of the unbound states is made, the harmonic approximation is quite close. Fig. 1.2 shows the actual Bloch state band structure for the range of well depths attainable in our experiment. Our minimum uncertainty ground state wave function has width of

$$\sigma_\phi/2\pi = \frac{1}{2\pi(4\kappa)^{1/4}} \cong 0.026 \qquad \Rightarrow \qquad \sigma_\rho = \frac{1}{2\sigma_\phi} \cong 3. \qquad (1.28)$$

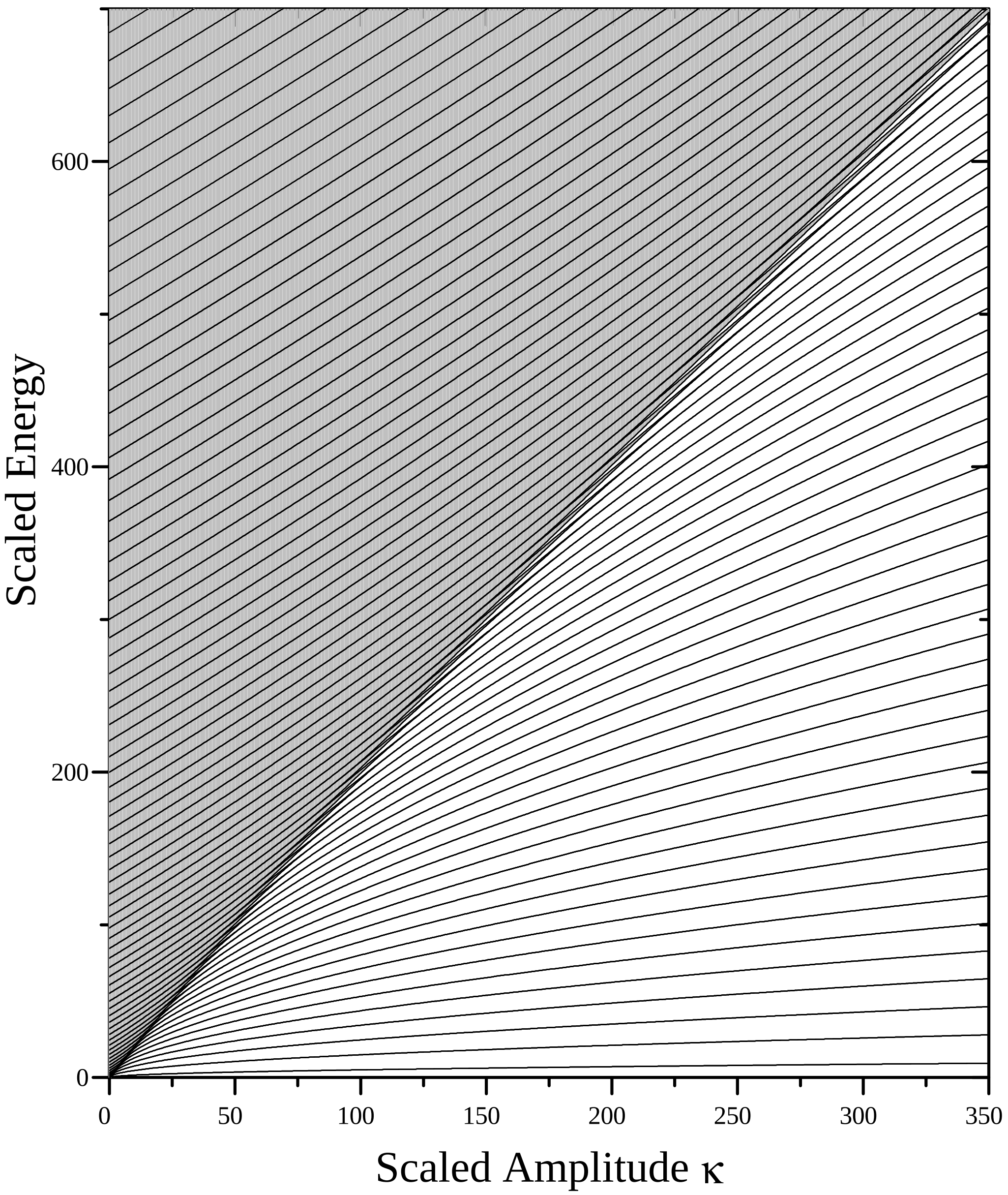

Figure 1.2: Energy band structure versus well depth for the scaled dimensionless variables $\mathcal{E}$ and κ (For $\bar{k} = 1$).

1.3 Chaos and the Kicked Rotor

Chaos describes the apparently random behavior of a deterministic system in which the separation of nearby trajectories grows exponentially in time. Since this only occurs in non-integrable systems, the only way to determine the long-time position of a trajectory is to numerically iterate the solution to the desired time. From a practical standpoint, it means that regardless of the precision of a calculation, each minute error will cause an exponentially increasing deviation from the trajectory intended, thereby making the time dependence seem unpredictable, despite the deterministic nature of the system. Nonetheless, there are many universal characteristics of chaotic systems that are predictable, and the existence of chaotic behavior in the fields of mechanics, electrical engineering, laser physics, biology, fluid flows, and others, makes understanding these characteristics an important endeavor [22].

For the work described here, I will point out some important relevant characteristics of classically chaotic systems, which can be found in several standard textbooks [22, 23, 24]. This description will start off with the pendulum Hamiltonian which we encountered in the last section. We use this to demonstrate some basic principles of the *phase space*, or *surface of section* views of a system's long-term behavior, and to show how the (completely integrable) pendulum is a good starting point to study chaos.

1.3.1 The Pendulum Phase Space

Any N-"degree of freedom" (N-DOF) Hamiltonian system which has N constants of motion is completely integrable. Therefore, any 1-DOF, autonomous system (like the pendulum, for example) has the Hamiltonian as a constant of the motion, and is therefore integrable. Trajectories of the canonical coordinates, $p(t)$ and $q(t)$, in an integrable system move along smooth continuous curves in time (except for fixed points). If we plot the two variables, $p(t)$ and

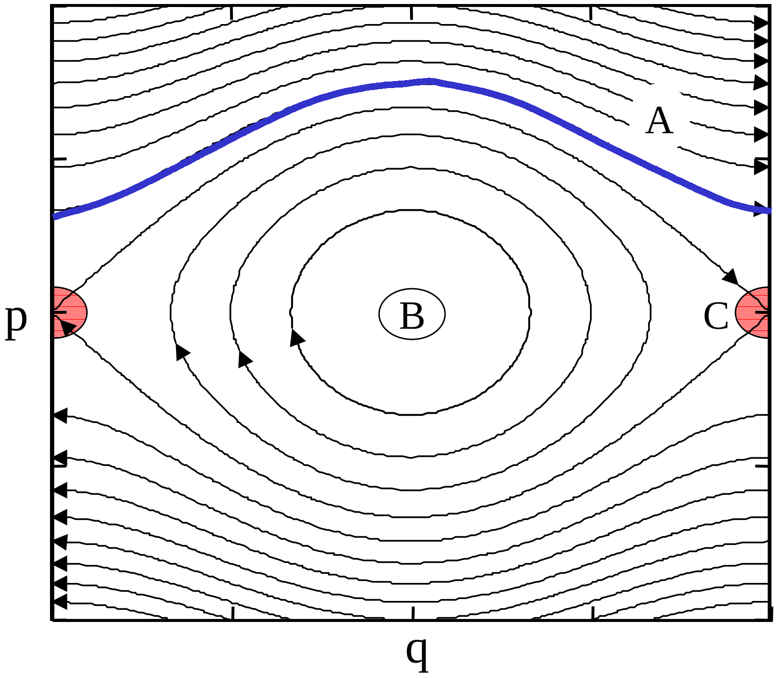

Figure 1.3: Example of a classical pendulum phase space. The trajectories near A show unbounded rotation in q. Trajectories near B show the stable oscillations that make up the island around the central stable fixed point. The points at C are the unstable fixed points which are the limit points for separatrix trajectories.

$q(t)$, against each other for all t, and for a representative set of initial conditions, we get a *phase space* plot. This type of plot is shown for the pendulum in Fig. 1.3 and shows, in a useful way, all of the possible types of motion for the system. It is important to understand this particular plot, not only because of the close relationship that the phase space plot has to the Poincaré *surface of section* plot, which is used extensively to characterize chaotic systems, but because of the central role that the pendulum plays in the analysis of near-integrable systems [23].

The phase space plot shows three important types of motion, each corresponding to a different energy/momentum regime. Each is represented by a different contour (trajectory) in the phase space. The first type connects the effect of the potential to the free motion of the rotor, and the last two are related to the hyperbolic and elliptical fixed points of the system.

The first type, which occurs at large momentum values where the total energy is larger than the maximum potential energy, is unbounded rotation ("A" in Fig. 1.3). One can see that as the kinetic energy gets higher, the effect of the potential becomes more and more just a perturbation to free motion of the rotor, represented by the flattening of the trajectories.

The second type of motion is related to the elliptic or stable fixed point at the center ("B"). This is the normal resting point of a pendulum. The closed contours surrounding this point represent periodic trajectories in phase space corresponding to the simple small amplitude swinging or libration of the pendulum. This collection of closed curves is called an island for that fixed point. On each curve, p and q oscillate with exactly the same frequency. Near the fixed point at the center this frequency approaches a fixed value, that of the harmonic oscillator approximation to the pendulum $\omega = K^{1/2}$. Toward the edge of the island ω approaches zero.

The edge of the island is defined by the *separatrix* ("C"), which directs the third type of motion. The separatrix is the trajectory which connects the hyperbolic, or unstable, fixed points on either side of the stable fixed point. The separatrix divides the two previous regions, and it's the unstable nature of its endpoints which provide the seed for the growth of stochastic behavior under the slightest perturbative provocation.

We should note that these curves are trajectories, and that the arrows on each represent a direction of flow. Also note that trajectories cannot cross themselves or each other, due to the deterministic nature of the motion. Finally note that if we consider the set of points inside a closed curve in the phase space, the trajectories of these points will remain inside the trajectory of the closed curve and the area spanned by these points will remain constant as they flow in the phase space.

1.3.2 The Perturbed Pendulum

Now suppose we consider a T-periodic time modulation of this interaction potential, where T sets the time unit, such that

$$\mathcal{H} = \frac{\rho^2}{2} + \kappa \cos(\phi) \sum_n f(\tau - n), \tag{1.29}$$

where $f(\tau)$ is the single period form of the unit amplitude modulation function. We assume that

$$\int_{-\infty}^{\infty} f(\tau) \mathrm{d}\tau = \int_{-1/2}^{1/2} f(\tau) \mathrm{d}\tau = \alpha \leq 1. \tag{1.30}$$

We have two points to make about this modulation.

First, a time-dependent, 1-DOF system is equivalent to a two degree of freedom time independent system. This is accomplished by extending the phase space to include τ and $\mathcal{H}$ as another canonical position/momentum pair. We can then apply all of the usual analysis done for autonomous 2-DOF Hamiltonian systems.

One of the most important tools in this analysis is the *surface of section* plot, which we mentioned previously. We begin with an integrable system such as the now extended pendulum, which has a four-dimensional phase space. First we fix $\mathcal{H}$, to make it three dimensional. Then we consider the position of a trajectory in the $\rho - \phi$ coordinate plane once every period of τ. The unperturbed pendulum is a trivial case of this, where the periodicities of τ and (ϕ, ρ) are uncoupled, and so this is simply a stroboscopic version of the continuous phase space plot shown earlier. However, in the presence of a periodic perturbation at frequency Ω_{p}, such a plot will reveal resonances between the periodic motion of the plot coordinates and the plotting frequency, when the ratio of the frequencies (or periods) is rational. Such a plot is shown for the unperturbed pendulum in Fig. 1.4 for an arbitrarily-chosen temporal period. In comparison to the phase-space plot, we can see that it shows all of the same structure, but now we can see that trajectories with periods that are rational multiples of the strobe period appear as fixed points. Meanwhile, the irrational trajectories quickly fill in the invariant curves, or tori, on which they started. In the unperturbed (integrable) case, however, it doesn't matter where you start on the rational trajectory, you will still get the same number of fixed points on a given curve, but their positions on the curve will just be shifted by the difference in starting points. These are, in reality, the same invariant curves.

The second point relates the resonances to chaos and the pendulum. Because the pendulum is nonlinear, the oscillation frequency ω is a function of amplitude. This means that there are an infinite number of resonant trajectories where $\omega = (r/s)\Omega_{\mathrm{p}}$, for any integers r and s. Unlike the unperturbed case, the Poincaré-Birkhoff Theorem states that rational tori, in the case of a small perturbation, will have $2ks$ fixed points (k integer), alternating between hyperbolic and elliptical. Each elliptic fixed point generates an island around it, essentially the same as the main island of the original pendulum, and each of these, again, have a similar structure on a smaller scale, and so on. Thus this rational torus has become a chain of ks islands. The creation of these island chains and their resemblance to the pendulum is very general in near-integrable systems. Because it can be used to analyze the behavior near resonances of these systems, much like the harmonic oscillator is used in linear dynamics, the pendulum Hamiltonian has been called the *standard Hamiltonian.* This makes our standing wave very useful since we can use it to

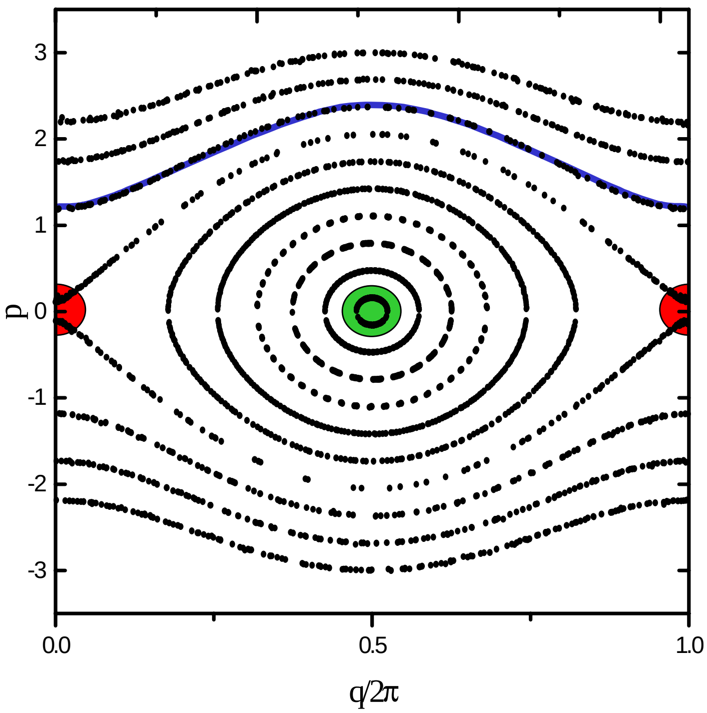

Figure 1.4: Example of a classical pendulum surface of section, demonstrating how rational winding numbers appear as fixed points in this stroboscopic view.

readily model variations of the pendulum system.

The hyperbolic fixed points are where the action is. Each one looks similar to the original separatrix intersection, except that these regions are no longer regular. One should refer to the previously given sources for details of the phase space structure around the perturbed hyperbolic points, as it is quite complex. The trajectories in this region no longer remain on smooth one-dimensional trajectories in the two-dimensional phase space, but instead fill some area of stochasticity. This is where the chaos begins, and it continues to grow and engulf more of the phase space as the perturbation increases. The coexistence of these two regions of behavior give rise to the description of islands of stability in a sea of chaos for cases like that shown in Fig. 1.5.

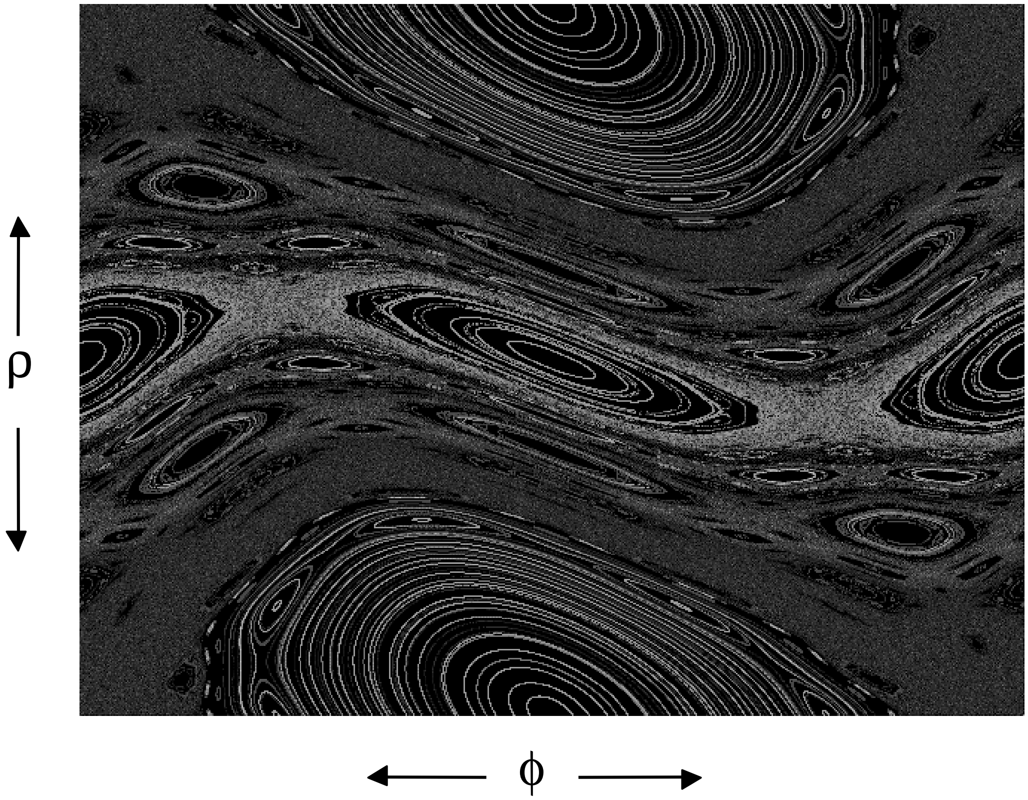

Figure 1.5: Delta-kicked rotor surface of section for K=1, showing a globally-chaotic mixed phase space.

The chaotic nature is normally defined by the exponential divergence of two nearby trajectories in the phase space. Mathematically, this rate of separation in time is often described by a positive Lyapunov exponent, λ [25].

What keeps these regions somewhat structured for small perturbations are the irrational tori that fill the space inbetween the rational ones. Some of these can remain as intact, continuous trajectories, only slightly distorted from the original unperturbed trajectories. A theorem by Kolmogorov, Arnold, and Moser guarantees the existence of these invariant tori for certain near-integrable conditions. Therefore these remaining curves are called KAM tori.

Like their unperturbed versions, they cannot be crossed by any other trajectories, and hence confine the chaotic regions they surround. When the perturbation gets too large, and the last KAM torus is broken, we have *global chaos*. At this point it is possible for a stochastic trajectory to drift unrestricted (except by islands) through the phase space. Fig. 1.5 shows a globally chaotic phase space just after the last KAM torus is broken. Its remains can just barely be seen in the plot as two curvy horizontal lines above and below the center islands.

1.3.3 The Delta-Kicked Rotor

Now we consider a specific and important variation of the pendulum Hamiltonian: the delta-kicked rotor. A realization of this system is the starting point for all of our experiments. It is a paradigm system for studying chaotic behavior.

The simplicity of the DKR, as shown in Eqs. (1.31 - 1.35), lends itself readily to experimental and numerical reproduction. Mathematically it can be described by a discrete map, often called the *standard map* for the same reason the pendulum is called the standard Hamiltonian. It locally describes other more complex chaotic maps, and its properties can be used to study general characteristics of chaotic behavior near a perturbed resonance. Casati *et al.* named it the simplest Hamiltonian system known to display chaotic behavior when they chose it to study quantum chaos [26]. For now let us consider its classical properties. It will be helpful to keep in mind a physical picture to understand the delta-kicked rotor, its relation to the pendulum, and why it is chaotic.

In Fig. 1.6 we can see that the pendulum is just a freely rotating rigid mass where the *constant* force of gravity provides torque of $\mathcal{T} = mgr\sin(\phi)$. In the DKR we turn this gravitational force on at discrete times, independent

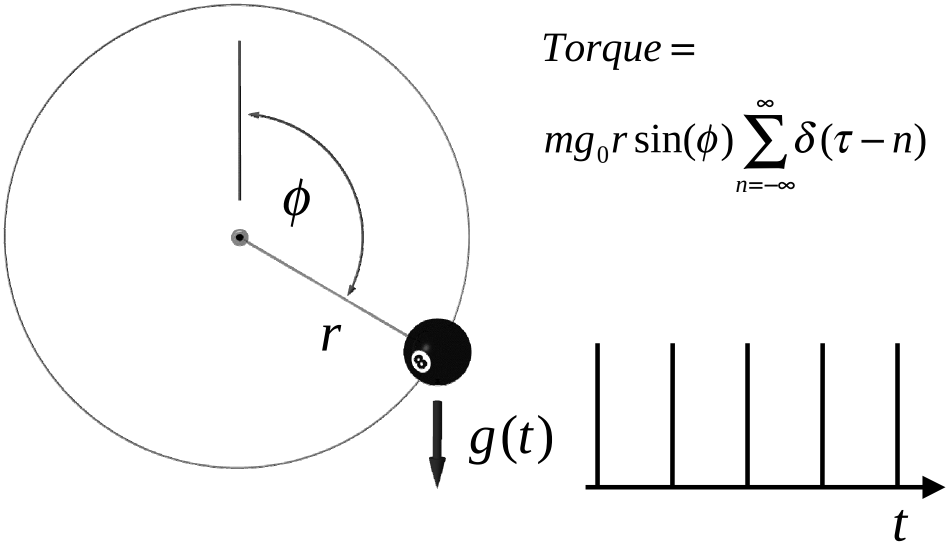
Torque =
$mg_0 r \sin(\phi) \sum_{n=-\infty}^{\infty} \delta(\tau - n)$
ϕ
r
$g(t)$
t

Figure 1.6: The physical picture of a rotor can provide intuition on many of the characteristics of the DKR.

of the position of the rotor, and so, can apply a different impulse each time step depending on where the rotor is when the kick arrives. Notice that the scaled DKR is 2π periodic in both ρ and ϕ, and is therefore normally plotted modulus 2π. The surface of section plots for the DKR all reflect this.

Clearly if the rotor doesn't move very far between pulses, the position will be very predictable and in the limit of continuous small pulses, will look like the pendulum. However, if a single kick is large enough to change the momentum enough to make the position change significantly before the next kick, then the $\sin(\phi)$ dependence allows the subsequent kick to be completely different in size and direction. A series of such kicks, though technically well determined, will have the appearance of a random walk in phase space. This explains why the degree of chaos depends both on the well depth V_0 and the period T in the unscaled units, since both conspire to increase the displacement between kicks.

In the case where $f(\tau)$ in Eq. (1.29) is a Dirac delta function, then we get

$$\mathcal{H} = \frac{\rho}{2} + K\cos(\phi)\sum_n \delta(\tau - n). \tag{1.31}$$

This is the Hamiltonian for the delta-kicked rotor.

The sum of delta functions provides an instantaneous impulse, or kick, once every period, where we have chosen the time unit to be T so that the scaled period $T' = 1$. The kick strength, K , is called the *stochasticity parameter*, and is proportional to V_0T in the MKS system. In general $K = \kappa/T'$ in the scaled units, where for many references where the preference is to set $\bar{k} = 1$ rather than $T' = 1$.

The resulting equations of motion are then

$$\begin{aligned} \dot{\phi} &= \rho, && (1.32)\\ \dot{\rho} &= \begin{cases} K\sin(\phi) & \text{if} \quad \tau = (0, \pm 1, \pm 2, \dots) \\ 0 & \text{if} \quad \text{otherwise.} \end{cases} && (1.33) \end{aligned}$$

This suggests a simple iterative map to describe the dynamics of a given trajectory. By integrating the equations of motion over one period we find

$$\begin{aligned} \rho_{n+1} &= \rho_n + K\sin(\phi_n) && (1.34)\\ \phi_{n+1} &= \phi_n + \rho_{n+1}. && (1.35) \end{aligned}$$

This is the *standard map* which was used to generate Fig. 1.7, and other surfaces of section for the DKR in this work.

Notice that the single parameter K completely determines the behavior of this system, and thus its phase space, as shown in Fig. 1.7. For $K = 0$ we see lines of constant momentum (KAM-tori) corresponding to the free rotor. Then, as we increase K, we see the KAM-tori distort and break apart as resonances form. By $K = 2$ we see large regions of chaos with isolated islands. At $K \approx= 4$ the primary island has become unstable, making the phase space for $K > 4$ predominently chaotic. Our experiments work in this range, $5 < K \lesssim 25$, where except for a few special exceptions, no structure is large enough to see on these phase space plots. A plot for $K = 10$ is shown in Fig. 5.1. The uniform stochasticity in this region makes it reasonable to consider the average motion of a phase space distribution. In particular, it is most common to consider the evolution of momentum distributions as a function of K.

In the absence of large islands we consider the average energy $\mathcal{E}$ of a distribution of trajectories, which is proportional to the variance $\langle \rho^2 \rangle$ of the momentum distribution. Calculations show that the random walk nature of the trajectories leads to diffusive growth in energy following the Fokker-Planck equation. The momentum distribution grows as a Gaussian whose variance increases linearly in time such that

$$\mathcal{E} = \frac{\langle \rho^2 \rangle}{2} = Dt, \tag{1.36}$$

where D is the diffusion coefficient. These characteristics are depicted in Fig. 1.8. D is actually a very complicated function of K which we will discuss later in Chapter 5, but to first order

$$D(K) = \frac{K^2}{4}. \tag{1.37}$$

is called the quasi-linear approximation.

Studying the energy growth turns out to be a very practical form of analysis, since most experiments lend themselves to measurement of the average energy of a distribution, rather than individual trajectories. For example,

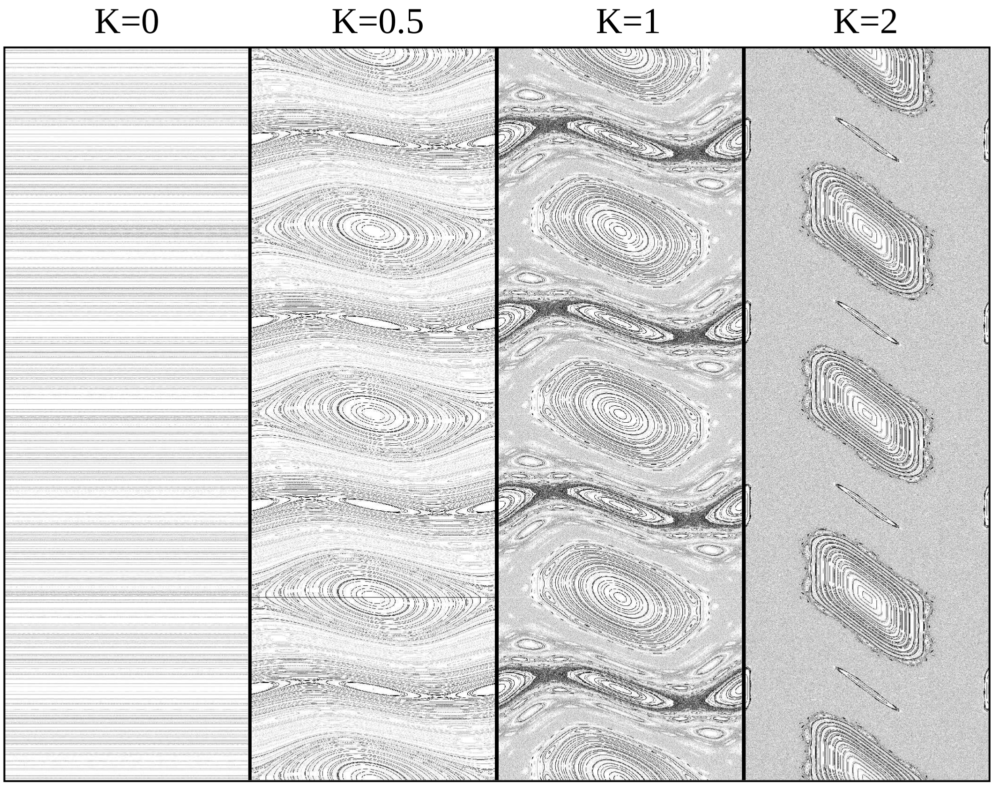

Figure 1.7: Evolution of DKR phase space as a function of the stochasticity parameter, K. $K \approx 1$ marks the onset of global chaos which is seen at $K = 2$ by the diffuse "sea of chaos" surrounding the stable islands, and allowing unbounded transport through the phase space. Note that each tile is 2π wide in ϕ, and 8π high in ρ, with $(\phi, \rho) = (0, 0)$ corresponding to the lower left corner of each. $K = 10$ is shown in Fig. 5.1.

the field intensity dependence of microwave ionization of highly excited hydrogen observed in the mid 70's showed that ionization can take place below the one photon ionization threshold [27]. This was later found to have an explanation in classical chaos. Considering the orbits classically, the effect was just due to the onset of global chaos leading to a diffusion to higher orbital energy levels until ionization occurred [25].

Other Rydberg experiments consider the distribution of the excited

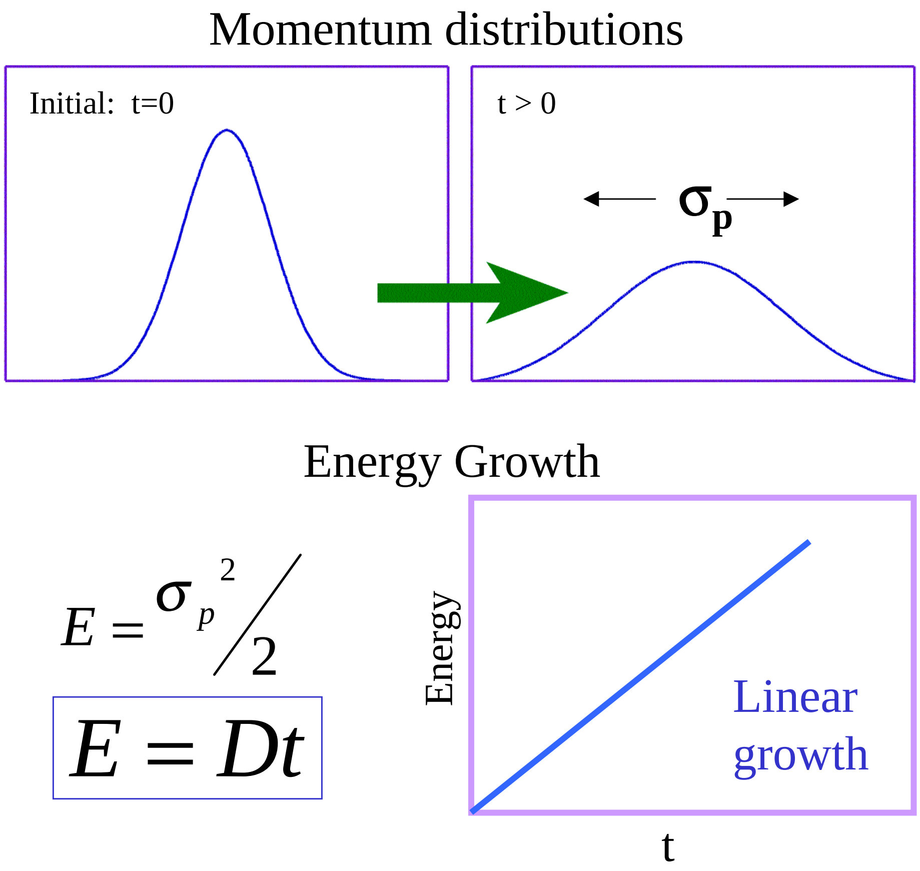
Momentum distributions
Initial: t=0
t > 0
σp
Energy Growth
E = σp2/2
E = Dt
Energy
Linear growth
t

Figure 1.8: Characteristics of classical diffusion

states rather than the just the energy [28]. Our work with trapped atoms looks at both changes in the form of the momentum distribution, and the growth of the average energy over time. Our results show that classical modeling is not, in general, sufficient to describe the observed distributions. Quantum effects interfere.

1.4 Quantum Chaos

There is much debate over what is meant by "quantum chaos." The differences between quantum mechanics and classical mechanics raise questions about whether chaotic behavior exists in quantum mechanics, how one would define it if it does, and how one could measure it [22]. Blümel would claim that not only does it exist, but that there are three different categories, all of which have valid examples [25]. These are:

a) A completely quantum system which shows exponential sensitivity to initial conditions.

b) A semiclassical system in which both quantum and classical variables can behave chaotically due to the quantum coupling to at least one classical degree of freedom.

c) A quantum system for which the classical analog is chaotic.
(This is the most common case)

If we believe that quantum mechanics can, in some limit, describe macroscopic, classical systems like the delta-kicked rotor, then it must allow chaotic behavior. With this assumption, one might wonder what conditions are necessary to see classically chaotic behavior. In our work we consider the third category of quantum chaos by studying the quantum kicked rotor. We experiment in regimes where the classical dynamics would be chaotic, but where quantum effects should be apparent. Much theoretical research has already been done on the classical DKR. It is very familiar to researchers in the field of nonlinear dynamics and quantum chaos, and its simplicity allows for reasonable numerical simulations. For these reasons it is an ideal system with which to compare the quantum and classical behavior of a classically chaotic system. We observe the differences from the classical kicked rotor, attempt to

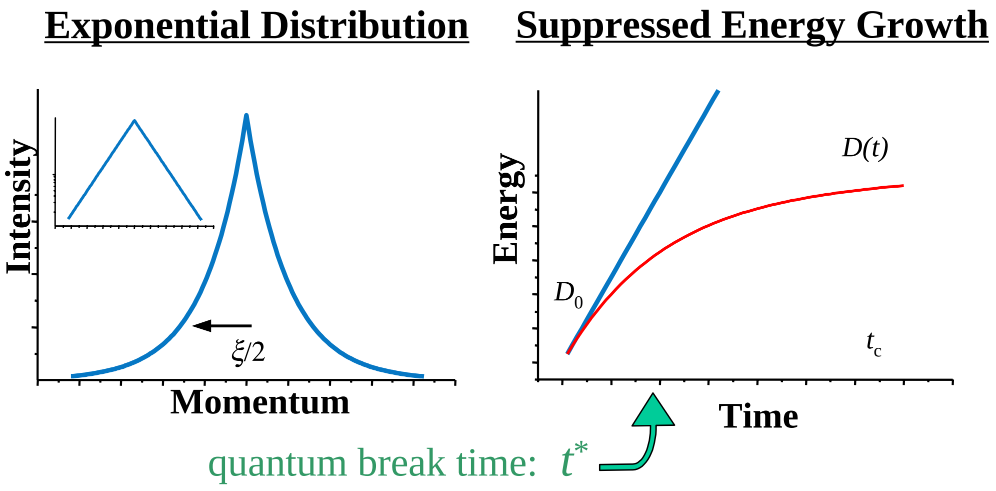

Figure 1.9: Depiction of typical signatures of dynamical localization showing the suppression of classical diffusion, and the exponentially localized momentum distribution. The inset on the left shows the exponential distribution in a semilog plot usually used in the analysis of these distributions.

find any quantum signatures of the underlying classically chaotic dynamics, and look for conditions under which the classical behavior might be recovered.

The primary difference between the quantum and classical cases is *dynamical localization*. This is a suppression of the previously described classical diffusion which was shown in Fig. 1.8. It was first observed in simulations of the DKR in 1979 by Casati *et al.* [26], and later connected to Anderson localization by Fishman *et al.* in 1982 [29]. This connection supported the expectation of exponentially localized eigenstates, which is a hallmark for Anderson localization [30]. These two characteristics, suppressed diffusion and exponential distributions, are considered the signatures of dynamical localization and are depicted in Fig. 1.9.

Several quantities are important for the characteriztion of the quantum dynamics shown in Fig. 1.9. I will follow the notation of Fishman and

Cohen [31, 32], though others present the similar material [33, 34]. Because of the periodic time dependence, the quantum kicked rotor system can be described by a Floquet basis of quasienergy eigenstates (analagous to Bloch states), designated by quasienergy ω. It has been shown that these states are exponentially localized in momentum space with some *localization length* ξ. Note that this is the $1/e$ value for the quasienergy states Ψ_ω. The momentum distribution $\langle \Psi_\omega^* \Psi_\omega \rangle$ will have a characteristic length of $\xi/2$. The argument for the dynamics of localization assumes that the quantum effects will become important after the time that is required to resolve the separation between the quasienergy states. This time is called the *quantum break time*, usually denoted by t^*. Scaling arguments lead to the conclusion that in the dimensionless units $t^* \approx \xi$. Before this time the quantum evolution will closely follow the classical diffusion, growing with an initial rate D_0. After this time, quantum localization will set in to halt the momentum growth, settling into some quasiperiodic state with an average length ξ.

Localization is a purely quantum effect and depends on the coherent interaction of the quasienergy states involved. Therefore, if some effect were present to destroy this coherence it seems likely that the localization should be destroyed as well. This thought has prompted many predictions regarding the effect of noise on dynamical localization, which is the subject of our research presented in Chapter 4. This problem presents two other quantities shown in Fig. 1.9, the coherence time t_c and the quantum diffusion rate $D(t)$. The first is the characteristic time over which the state can maintain coherence (this should be longer than t^* in order to observe localization), and the second is a noise dependent diffusion function which characterizes the transition after the break time from the initial rate D_0 to some final quantum diffusion rate lying between 0 and D_0.

Together, these characteristics determine the conditions neccessary to see dynamical localization. First we must have an initial condition small compared to the localization length. We must also have an interaction time longer than the break time. Finally, we must have a sufficiently isolated system to have a coherence time longer than the break time, and a quantum diffusion rate less than D_0.

The effects of dynamical localization were first considered experimentally in 1988-89, where the suppression of microwave ionization of Rydberg atoms was attributed to dynamical localization [35, 36]. Subsequently, our research group produced textbook examples of dynamically localized momentum distributions from cold sodium atoms in a periodically driven standing wave. Our current experiments use the localized momentum distributions as a reference from which we start to look for deviations. Discovering these variations from localized behavior enables us to better understand the mechanisms involved in creating or destroying dynamical localization, and the correspondence (or lack thereof) between classical and quantum dynamics.

Chapter 2

Experimental Method

2.1 Introduction

The experimental setup to study the physics described previously has several requirements. First, we need atoms isolated in a vacuum. Second, we need trapping and cooling lasers to create the initial conditions. Third we need the interaction beam to create the desired potential. Fourth, we need a method of measurement to analyze the initial and final conditions. Finally, it is highly desirable to have computer automation to coordinate all the steps and help in the analysis. The overall table layout for this experiment is shown in Fig. 2.1, indicating the major components that will be described in this chapter.

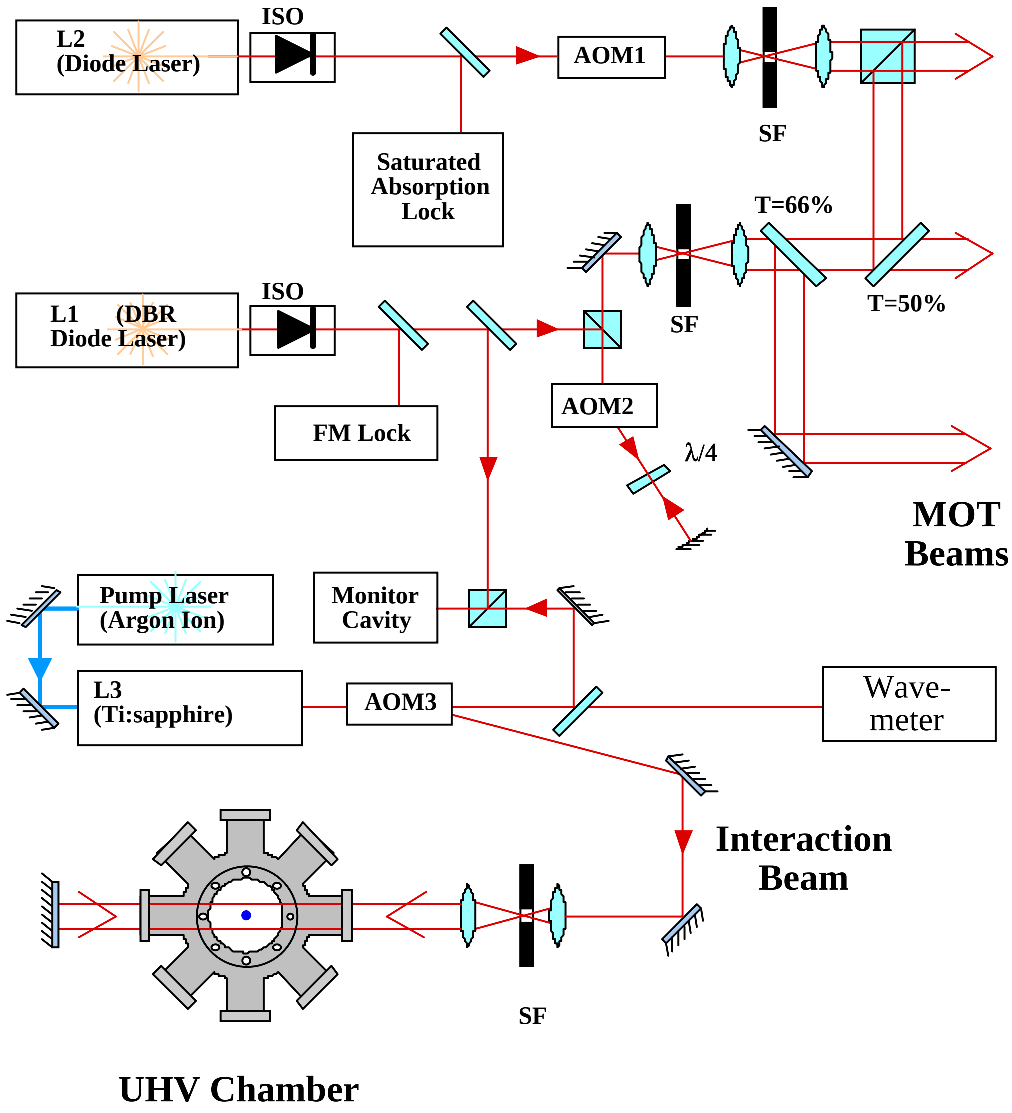
L2
(Diode Laser)
ISO
AOM1
SF
Saturated Absorption Lock
T=66%
SF
T=50%
L1 (DBR Diode Laser)
ISO
AOM2
FM Lock
λ/4
MOT Beams
Pump Laser (Argon Ion)
Monitor Cavity
L3 (Ti:sapphire)
AOM3
Wave-meter
Interaction Beam
SF
UHV Chamber

Figure 2.1: Schematic diagram of the experimental setup. Two diode lasers provide the light for the MOT, and a Ti:sapphire laser provides the far-detuned standing wave.

2.2 The Cesium Chamber

I will give a detailed description of the chamber since it has several characteristics which directly impact the quality of our experiment. Relevant factors include the size of the chamber, the stainless steel construction, the coated windows, and the control of the cesium supply.

Our ultra-high vacuum (UHV) chamber is based on a modified 6-way stainless steel cross, custom manufactured by HPS (Fig. 2.2). The six main ports are capped with 4.5 inch diameter viewport flanges, with the four horizontal windows defining the x- and y-axes of the MOT, and the other two defining the (vertical) z axis. Four 2.75 inch diameter horizontal ports form a cross 45 degrees off from the MOT x-y axes. Two of these ports define the 1-D interaction axis, with one of the perpendicular ports providing the camera viewing window. The final port supplies a dark background for viewing of the MOT, and provides access to the chamber for the Cs source, the 20 l/s Star-Cell Vac-Ion Plus 20 pump from Varian (model 919-0236), and the HPS model 10000 5836 tungsten filament hot cathode ion gauge. We used a SensaVac 919 controller from HPS for the gauge.

All of the viewports were antireflection coated on both sides for less than 1% reflection per surface. This was one important improvement over previous experiments where the bare surface reflections caused interference fringes in the MOT. Even with the anti-reflection coating, we observed effects of the window reflections creating a weak standing wave from our Hamiltonian beam.

The entire chamber is surrounded by three large pairs of Helmholtz coils for nulling the DC magnetic field at the center of the MOT. They are roughly square, 15 inches to a side, and the coils in each pair are separated by about 8 inches. These have about 44 turns of 0.020" diameter copper magnet

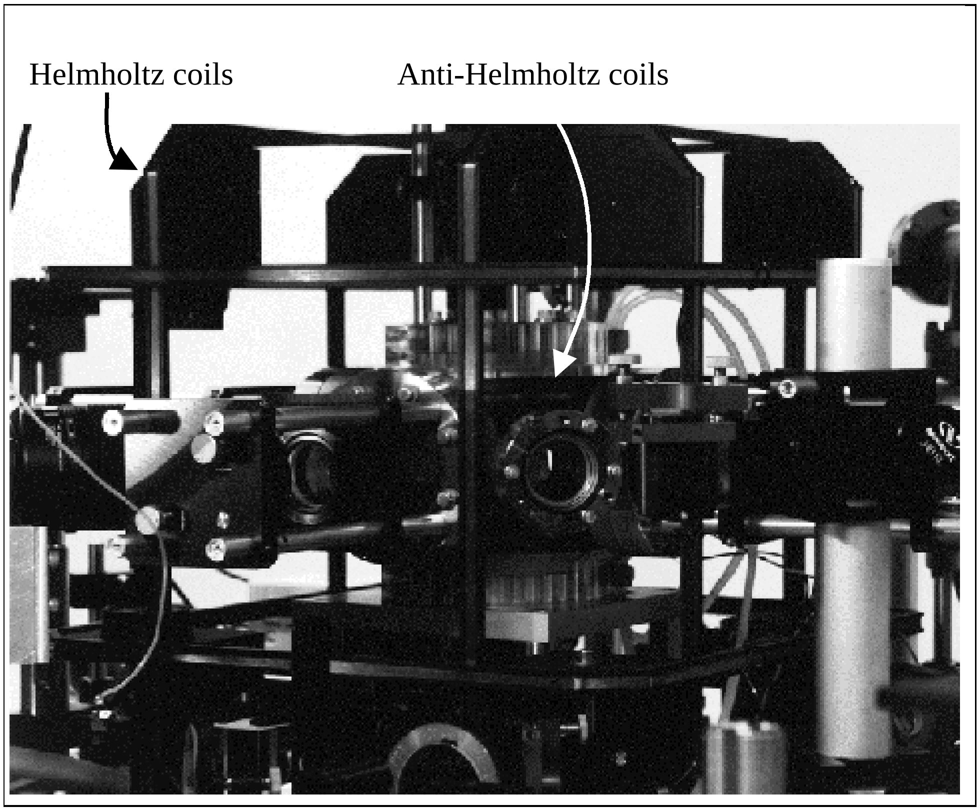

Figure 2.2: Picture of the stainless steel UHV chamber, looking into the interaction beam input window. Large Helmholtz coils can be seen surrounding the apparatus, while the smaller anti-Helmholtz coils can be seen attached to the upper and lower windows.

wire, with a total resistance of 6 ohms in each coil. These produce nearly 2 gauss/Amp of homogeneous magnetic field along each of their respective axes.

Surrounding the large windows on the top and bottom of the chamber are mounted the anti-Helmholtz configured coils for the magneto-optic confinement of the atoms. These coils are each 6.2 inches in diameter, with 202 turns of the same wire. The resistance of each coil is about 8.7 ohms. Typical operating currents of about 3 Amps provide gradients of 11 G/cm along the coil pair axis, and half that perpendicular to the axis. Under these operating conditions, each coil dissipates about 80 watts of power. To cool these coils, the wire is wrapped around an anodized aluminum housing through which we run chilled water.

The current in each coil is driven independently by its own pair of LM12 36 volt, high power op-amps in a push-pull configuration as shown in Fig. 2.3. The push-pull circuit allows a coil to be driven in either direction with a single high power source. The independent drives allow us to electronically move the zero point of the trapping field in order to reposition the MOT. In order to electronically switch the coils on and off we installed a TTL input on the coil control box. This acts as an inhibit switch to set the current control signal to zero when TTL input is high. The circuit brings the 3 Amps of current in each coil to zero in about 100 μs. Unfortunately, the actual magnetic field does not shut down so fast because of our chamber design.

The use of large conflat windows on a stainless steel chamber has a significant drawback. First, it made the overall size of our chamber much larger than the glass chamber used in the previous experiments with sodium [7]. Therefore the anti-Helmholtz coils had to be roughly 50% larger. This, in turn, meant that we needed roughly twice the current in the coils to create the same confinement, and hence twice the magnetic field near the chamber. Combined with the large conductive mass of the steel chamber, we found that the eddy currents generated in the chamber housing slowed our magnetic field ring-down time to nearly 10 ms (Fig. 2.4). In contrast, the glass chamber field had shut off in about 200 μs. The effect of this magnetic field persistence will be discussed more in the description of our cooling. Additionally, the high current demanded the elaborate water cooling scheme for the coils.

We introduced cesium to the chamber via two UHV all-metal bakeable 1-1/2 inch diameter valves (Varian model 951-5027). One gram of the cesium was stored in a glass ampule attached to the outermost valve (Fig. 2.5). The

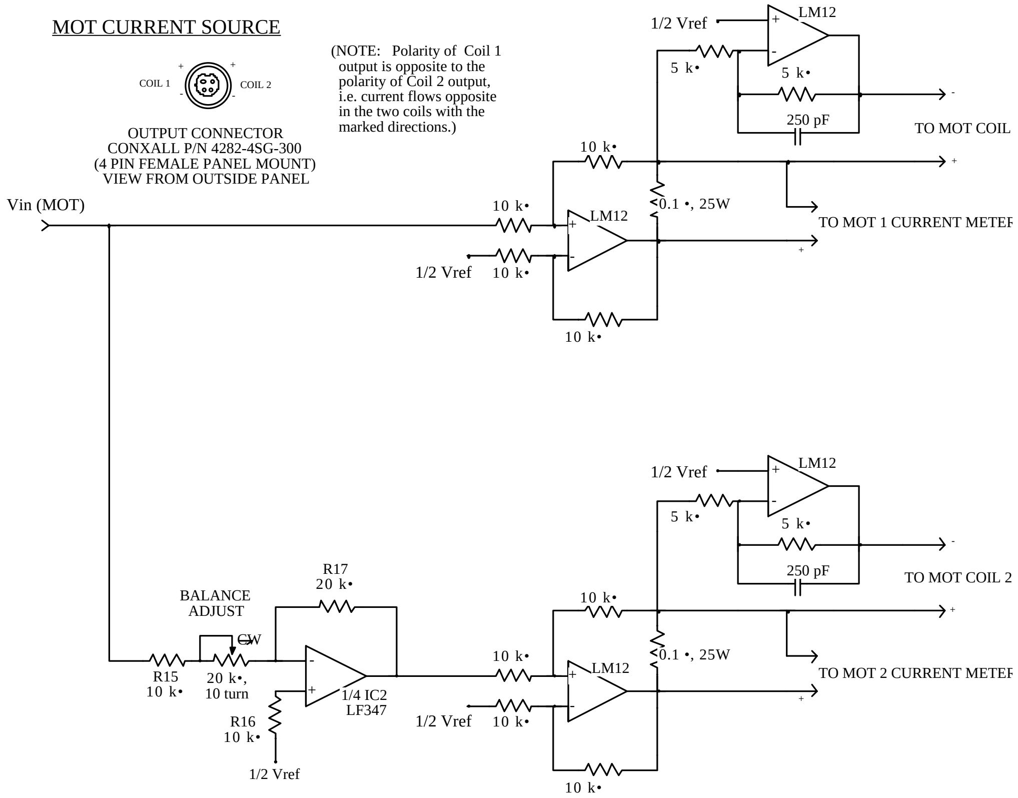
MOT CURRENT SOURCE
COIL 1
COIL 2
+
+
-
-
OUTPUT CONNECTOR
CONXALL P/N 4282-4SG-300
(4 PIN FEMALE PANEL MOUNT)
VIEW FROM OUTSIDE PANEL
(NOTE: Polarity of Coil 1 output is opposite to the polarity of Coil 2 output, i.e. current flows opposite in the two coils with the marked directions.)
Vin (MOT)
1/2 Vref
LM12
5 k•
5 k•
250 pF
TO MOT COIL
10 k•
0.1 •, 25W
TO MOT 1 CURRENT METEF
10 k•
LM12
1/2 Vref
10 k•
10 k•
1/2 Vref
LM12
5 k•
5 k•
250 pF
TO MOT COIL 2
10 k•
0.1 •, 25W
TO MOT 2 CURRENT METEF
R17
20 k•
BALANCE
ADJUST
CW
R15
10 k•
20 k•,
10 turn
R16
10 k•
1/2 Vref
1/4 IC2
LF347
10 k•
LM12
1/2 Vref
10 k•
10 k•

Figure 2.3: Schematic for the MOT coil current driver circuit (D. A. Steck). V_{ref} is set by a precision voltage reference to 17.5 volts. The input signal can swing from positive $V_{\mathrm{ref}}/2$ to negative $V_{\mathrm{ref}}/2$ to completely reverse the magnetic field direction. The “balance adjust” is included to vary the relative amplitude of the upper and lower coils in order to vary the vertical position of the MOT center.

inner valve was left wide open and will only be used in the event that we want to remove the cesium without breaking vacuum. The outer valve was normally left lightly closed (full closure would shorten the limited lifetime of the valve seal), and just opened one or two turns to allow cesium to enter the chamber as needed. The room temperature cesium vapor pressure of 2×10^{-5} torr was adequate to fill the chamber through these valves [21]. Our ion pump current of 45 μA indicates that our chamber pressure was typically 8×10^{-8} torr.

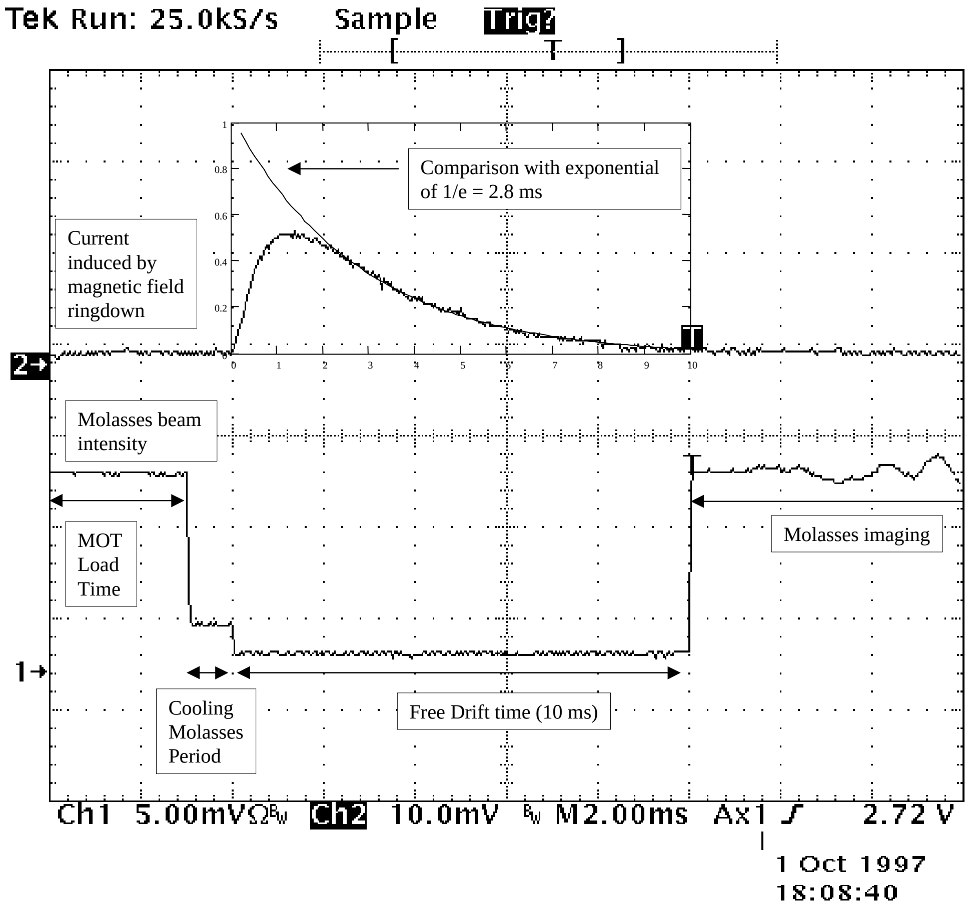

Figure 2.4: Display from a digital oscilloscope showing the ringdown time of the magnetic field for the MOT. The top trace is the signal from a wire loop placed just above the top chamber viewport, and represents the derivative of the magnetic field as it is shut down. For reference, the bottom trace (1) shows the signal from a photodiode measuring the molasses beam intensity. Various steps of the measurement cycle are labled on this trace, showing that the B-field is switched off at the beginning of the free drift time. Comparison with exponential curve shows a ringdown time constant of about 3 ms.

Originally we tried a variable leak valve (Varian 951-5106) to let the cesium in but we had to bake the ampule at nearly 100 °C in order to get

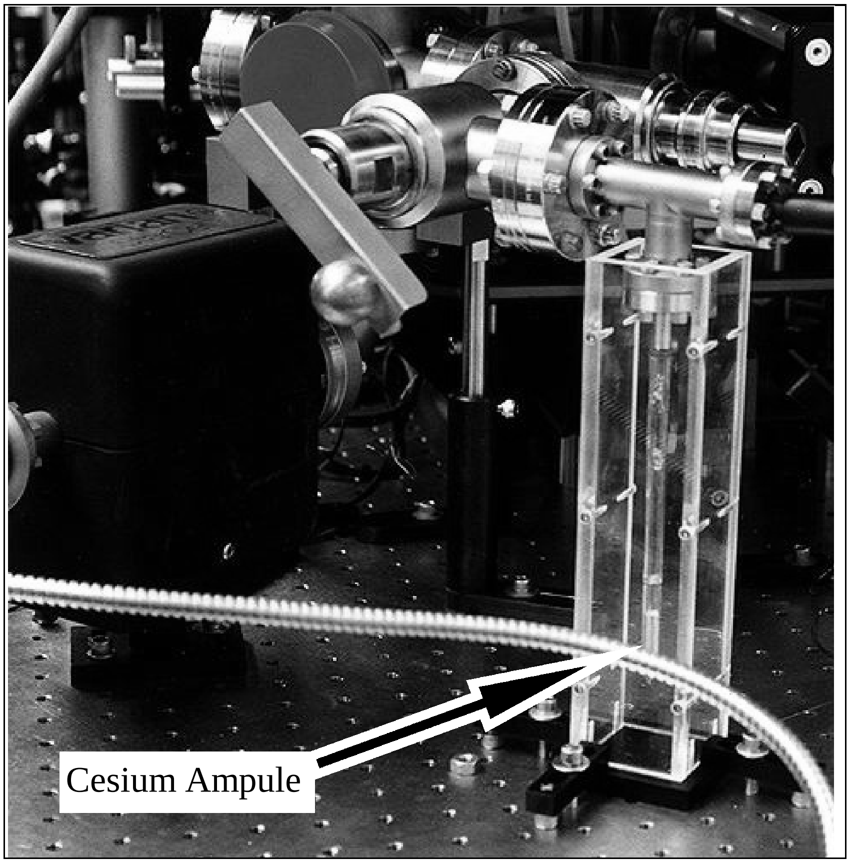

Figure 2.5: Picture of our Cs source attached to the chamber via two ultra-high vacuum all metal valves.

enough throughput to overcome the pumping rate (there seems to be a dramatic increase in cesium evaporation at around 90 °C). Since an initial coating of the chamber was required to achieve an equilibrium pressure high enough to obtain a visible cloud of atoms in the MOT, we left this valve full open for one week with the heaters on and still could not see any sign of cesium atoms. Over a month later we detected trapped atoms, but very few. We switched to the large-aperature two-valve system to avoid using heaters, although it was still required to heat the ampule to 100 °C for a few days to initialize the chamber.

2.3 The MOT Lasers

As stated previously one of the great advantages of using cesium is that the wavelength is accessible with currently available diode lasers. The reliability and ease of use that diode lasers provide made the day-to-day operation of our trap a nearly turn-key operation.

2.3.1 The Trapping Laser

Our main trapping laser for the MOT uses an SDL-5712-H1 Distributed Bragg Reflector (DBR) laser diode (L1 in Fig. 2.1). It is rated for 100 mW CW operation at 852 nm, and the product characteristics are listed in Table 2.3.1. It is mounted to an SDL-800-H, 5 W passive heatsink, with the active temperature control from an internal thermoelectric cooler. The thermistor lock point of ~ 15 kΩ indicated a temperature of ~ 15°C for the diode.

We collimate the beam with a Rodenstock 5 mm AR coated lens (N.A. = 0.5). The lens is mounted on a Line Tool x-y-z micropositioner in order to precisely position the lens. A high degree of stability and sensitivity is required of this micropositioner, since the lens is the most important and sensitive element of this laser setup. The horizontally elongated elliptical beam is then shaped by an anamorphic prism pair to be roughly circular and about 1 mm in diameter. We put this through two Conoptics model 713 optical isolators, which we measured to have isolation values of 40 dB and 37 dB, leaving us roughly 80 mW of light to work with.

We split 10% of this light off to a saturated absorption FM spectroscopy setup (FM Lock in Fig. 2.1), similar to that used in our previous experiments [7]. This method has the advantage that it does not modulate the beam that is actually going to the experiment. The setup is shown schematically in Fig. 2.6. With this we lock the DBR using the crossover transition between

Table 2.1: DBR Data

Data for SDL-5712-H1 DBR Laser Diode		
Tuning [a]		
Temperature	0.07	nm/deg
Current	0.003	nm/mA
	1.24[b]	GHz/mA
Mode hop seperation	0.08	nm
	27	mA
Efficiency and Electronic Characteristics [c]		
Differential Q.E.	0.47	
Slope Efficiency	0.68	mW/mA
I_{th}	29	mA
$I_{\max}$	179	mA
$P_{\max}$	100	mW
R	3.21	ohms
Beam Characteristics [d]		
Beam Divergence θ_{FWHM}		
$\perp$ to facet	30	deg
$\parallel$ to facet	10	deg
Bandwidth	3	MHz

---

[a] SDL Operators Manual

[b] conversion @ 852 nm

[c] Laser Data Sheet

[d] SDL Catalog

the $(6\mathrm{S}_{1/2}, F = 4) \longrightarrow (6\mathrm{P}_{3/2}, F' = 4)$ transition and the $(6\mathrm{S}_{1/2}, F = 4) \longrightarrow (6\mathrm{P}_{3/2}, F' = 5)$ molasses cycling transition (f_{ct} in Fig. 2.6).

The locking is achieved via direct modulation of the laser current in response to the error signal generated by the FM setup. This error signal is sent to a homebuilt lock box which generates an output voltage using both proportional and integrated feedback from the input. This box can lock to the zero point, or a manually selected offset, and provides a modulation input and control for sweeping of the spectrum.

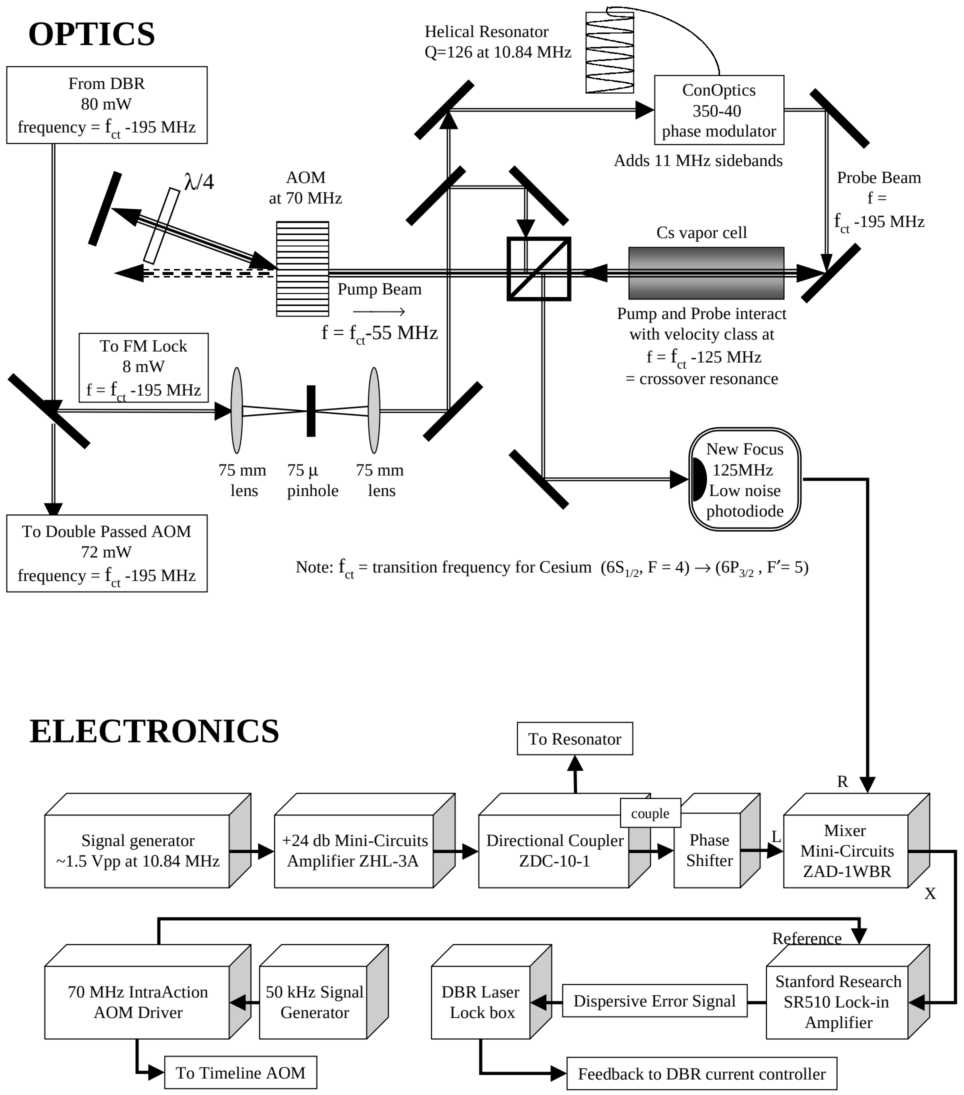
OPTICS
From DBR
80 mW
frequency = f_{ct} -195 MHz
Helical Resonator
Q=126 at 10.84 MHz
ConOptics
350-40
phase modulator
Adds 11 MHz sidebands
$\lambda/4$
AOM
at 70 MHz
Probe Beam
f =
f_{ct} -195 MHz
Cs vapor cell
Pump Beam
⟶
f = f_{ct}-55 MHz
Pump and Probe interact
with velocity class at
f = f_{ct} -125 MHz
= crossover resonance
To FM Lock
8 mW
f = f_{ct} -195 MHz
75 mm
lens
75 µ
pinhole
75 mm
lens
New Focus
125MHz
Low noise
photodiode
To Double Passed AOM
72 mW
frequency = f_{ct} -195 MHz
Note: f_{ct} = transition frequency for Cesium $(6S_{1/2}, F = 4) \rightarrow (6P_{3/2}, F' = 5)$
ELECTRONICS
To Resonator
R
Signal generator
~1.5 Vpp at 10.84 MHz
+24 db Mini-Circuits
Amplifier ZHL-3A
Directional Coupler
ZDC-10-1
couple
Phase
Shifter
L
Mixer
Mini-Circuits
ZAD-1WBR
X
Reference
70 MHz IntraAction
AOM Driver
50 kHz Signal
Generator
DBR Laser
Lock box
Dispersive Error Signal
Stanford Research
SR510 Lock-in
Amplifier
To Timeline AOM
Feedback to DBR current controller

Figure 2.6: Schematic of optical setup for the FM saturated absorption lock for the molasses beam.

The output from the lock box goes to a NIST-built laser diode current controller, mounted in a Canberra 1400 NIM crate. Next to the current controller is the NIST Type II temperature controller which controls the temperature via the TE cooler and thermistor in the laser. The crate also contains identical current and temperature controllers for the repump laser described below, and an alternative homebuilt lock box used for the repump laser.

Due to the 140 MHz frequency shift from the double-passed AOM in the FM lock, and the use of the crossover transition, the output of the DBR is set 195 MHz to the red of the $F = 4 \rightarrow F' = 5$ cycling transition ($f_{\text{ct}} - 195$ MHz). This is compensated by AOM1 in Fig. 2.1, which is a tunable, double-passed AOM centered at 80 MHz. This gives us the ability to electronically detune the molasses beam from the cycling transition over the range $f_{\text{ct}} - 75$ MHz to $f_{\text{ct}} +$ 5 MHz. We typically use $f_{\text{ct}} - 15$ MHz for cooling and trapping.

At this point we have 36 mW of light in a 1 mm diameter beam whose spatial quality is roughly Gaussian, but still contains some residual distortion. We obtain a large Gaussian beam by putting it through a Newport model 900 spatial filter with a 15 μm pinhole. The output is a rapidly diverging Gaussian beam with some faint rings that we block with an iris. We collimate this beam using a 200 mm focal length, 2 inch diameter lens, leaving a 26 mW beam with a Gaussian $1/e^2$ radius of $w_0 = 1.4$ cm. This gives a maximum intensity of 8.5 mW/cm^2, which is roughly 3 times the resonant saturation intensity for the atomic transition. While this power is not always desirable for cooling, it is important for uniform imaging of the atomic sample.

The molasses is formed by splitting this beam with two 2 inch beam splitters ($T = 50\%$, $T = 60\%$) into three beams of equal intensity for the x, y, and z axes of the molasses. Each beam is passed through a quarter-wave plate oriented 45° to the beam polarization, through the chamber, through an identically oriented quarter-wave plate on the other side, and then retroreflected back. Along with the previously described magnetic field coils, this generates the $\sigma^+ - \sigma^-$ beam configuration for the molasses.

2.3.2 The Repump Laser

Although the molasses is tuned near the $(6\mathrm{S}_{1/2}, F = 4) \longrightarrow (6\mathrm{P}_{3/2}, F' = 5)$ transition, there is still about a 0.01% chance per scattering event of making a transition to the $(6\mathrm{S}_{1/2}, F = 3)$ ground state. This undesired transition would remove atoms from the molasses interaction, and therefore cause the MOT to decay. We measured the time constant for the MOT decay to be about 3 ms. Therefore we follow the standard practice of illuminating the MOT with some light tuned to repump atoms out of this lower ground state. In our case we built a separate laser (L2 in Fig. 2.1) which supplies light tuned on resonance to the $(6\mathrm{S}_{1/2}, F = 3) \longrightarrow (6\mathrm{P}_{3/2}, F' = 4)$ absorption line.

The repumping laser that we built is Littrow-configured grating-stabilized diode laser system, shown in Fig. 2.7. These are popular items in physics labs and have many designs, including several commercial models. Useful review articles on such devices are cited in References [37] and [38]. Our system was modeled after a design used in Konstanz, Germany. The rotation points for the grating adjustments in this design depend on thin metal flexible joints rather than ball-bearing joints (Fig. 2.8). The hope was that a more monolithic design would be simpler to assemble and have better stability. We have found that once aligned, this laser may be used for months without making any mechanical adjustments.

The laser source used in the repumping laser is a 150 mW, single mode SDL model 5421-G1 diode laser. The specifications for this laser are shown in Table 2.3.2. The G1 9 mm housing is mounted in a Thorlabs LT230P-B, $f = 4.5$ collimation tube system, with a numerical aperture of 0.55. This tube is then mounted in the 954 aluminum bronze housing as shown in Fig. 2.8.

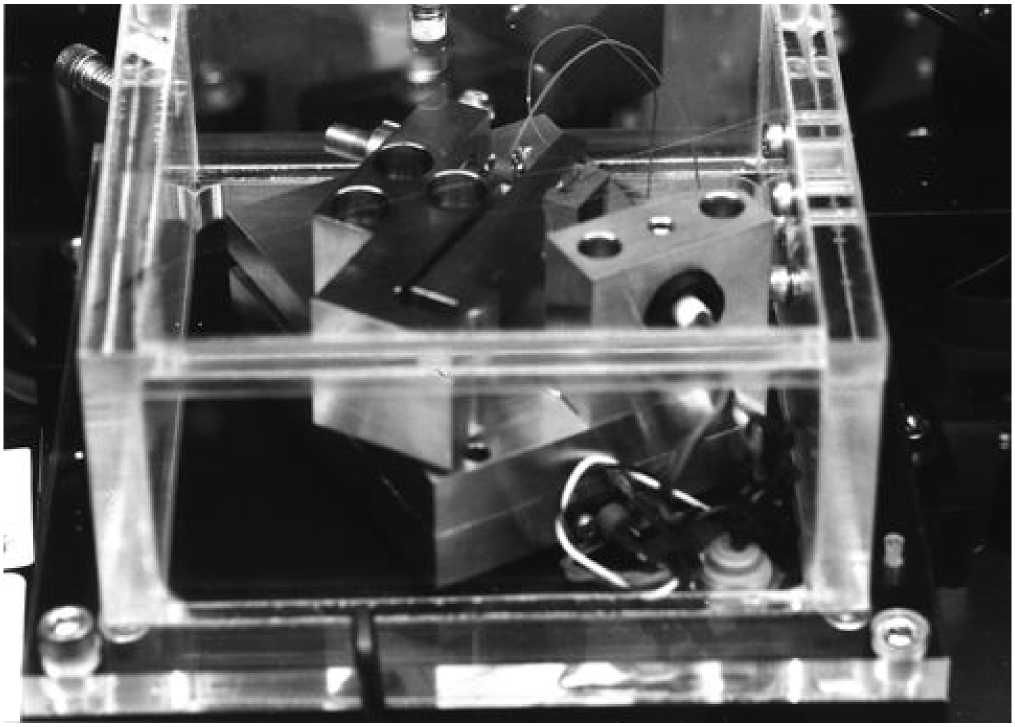

Figure 2.7: Photograph of grating stabilized diode laser for the repump beam

The bronze used for the laser mount and grating adjustment parts was chosen as a compromise between the resilient springiness of steel, needed for the flexible joints, and the high thermal conductivity of copper, needed for responsive temperature stabilization. The bronze base plate sits on top of a Melcor CP1.0-127-05L thermoelectric cooler which is controlled by the second NIST Type II temperature controller. The feedback comes from a 50 kΩ thermistor inserted into the bronze baseplate.

The entire bronze assembly is mounted on the aluminum base of the housing. There is a Lucite cover over the top to provide some degree of thermal and acoustical isolation, as well as protection from dust. The housing is bolted to the optical table with steel posts.

The optical design is a simple Littrow configured grating feedback sys-

Table 2.2: Repump Diode Data

Data for SDL-5721-G1 Single Mode Laser Diode		
Tuning [a]		
Temperature (between hops)	0.07	nm/deg
Temperature (including hops)	0.3	nm/deg
Current	0.005	nm/mA
	2.07[b]	GHz/mA
Efficiency and Electronic Characteristics [c]		
Differential Q.E.	0.6	
Slope Efficiency	0.87	mW/mA
I_{th}	23	mA
I_{max}	197	mA
P_{max}	150	mW
R	2.86	ohms
Beam Characteristics [d]		
Beam Divergence θ_{FWHM}		
$\perp$ to facet	30	deg
$\|$ to facet	9	deg
Bandwidth	15	MHz

---

[a] SDL Operators Manual

[b] conversion @ 852 nm

[c] Laser Data Sheet

[d] SDL Catalog

tem. This means that the $m = -1$ order interference peak is directed directly back into the laser, forming a cavity with the rear facet of the laser. The angular dependence of the frequency dispersion of this diffracted light means that the maximum Q of this cavity will be at a frequency that depends on small deviation of the grating angle around this peak. This narrow band tunable feedback then tunes and narrows the frequency output of the laser.

Our grating is an inexpensive Edmund Scientific ruled aluminum grating with 1200 grooves/mm, a 500 nm (17°) blaze, and a size of 25 mm × 25 mm. For improved efficiency we evaporated a 500 Å gold coating over the aluminum (with chromium underneath for better adherence to the aluminum). The results of our efficiency tests are shown in Table 2.3, indicating a small improvement in the efficiency due to the gold coating. Since we only need a half-inch wide grating for the laser, we divided the grating into 4 half inch squares by coating the large square with fingernail polish, cutting it with a diamond saw, and then soaking it in acetone to remove the polish.

Table 2.3: Gold Coating Data

Reflectivity of gold coating versus thickness [a]			
Coating thickness [b]	Incident power	0^{th} order	1^{st} order
8 Å	9.4 mW	6.0 mW (64%)	1.6 mW (17%)
250 Å	9.4 mW	6.3 mW (67%)	2.0 mW (21%)
500 Å	9.4 mW	6.3 mW (67%)	2.0 mW (21%)

---

[a] Set up in Littrow autocollimation configuration

[b] 60 Å of Cr over under gold

We designed the tuning angle plane to be horizontal. Therefore, we mounted the grating as shown in Fig. 2.8 with the with the grooves vertical and the blaze towards the laser. The laser diode then had to be oriented so the long axis of the elliptical far-field cross section is horizontal in order to maximize the number of grooves used on the grating. Fortunately, this also orients the polarization in the S-direction (vertical in this case), which significantly increases the diffraction efficiency in comparison to P-polarized light.

Electronic control of the grating position is done with a stack of three American Piezo Ceramics piezoelectric discs. They are 8 mm in diameter by 2.54 mm thick with an expansion coefficient of $d_{33} = \Delta l/V = 450 \times 10^{-12}$ m/V. Our Trek model 601B high voltage amplifier is set to a gain of 50 for an input range of -5 V to +5V. This give us a displacement capability of 675 nm, which translates to about 8 GHz of frequency sweep.

In order to maximize the continuous electronic tuning range, we designed the rotation point of the grating mount to be at the intersection of plane of the diode facet and the plane of the grating. This condition maintains the phase of the cavity as the grating angle sweeps the wavelength, and thus minimizes the mode hops that would otherwise occur at the free spectral range of $\sim$ 6 GHz [39, 40].

The current is controlled with the same type of NIST controller as the DBR laser, but the locking scheme is slightly different. In this case we use the saturated absorption scheme shown in Fig. 2.9 which feeds back to the grating rather than the current for frequency control. Since we use the 100.5 MHz AOM1 as a shutter to electronically control the repump laser, we must compensate for the +100 MHz frequency shift by locking the laser output 100 MHz red of the repump transition. By using the $(6\mathrm{S}_{1/2}, F = 3) \longrightarrow (6\mathrm{P}_{3/2}, F' = 3, 4)$ crossover line of the saturated absorption spectrum (100.5 MHz red of the resonance) for the locking error signal, we not only obtain the proper frequency, but have a stronger signal to lock to. This can be seen in the spectrum in Fig. 2.9. A differential photodiode subtracts the Doppler background from the absorption signal, giving the relatively flat spectrum shown in the figure. We obtain a dispersive error signal by dithering the laser frequency via a small 20 kHz modulation of the grating piezo stack. We then feed this into an EG&G model 5204 lock-in amplifier, and lock to the resulting dispersive signal with a home built NIM mounted lock box.

Driving the laser diode at 93 mA produces an output from the grating of about 40 mW. After the beam is passed through AOM1 it is filtered and expanded in a similar fashion as the molasses beam (Fig. 2.1), and combined with the vertical component of the molasses light to intersect with the MOT.

This configuration provides approximately 16 mW of repumping light in a 2 cm diameter beam.

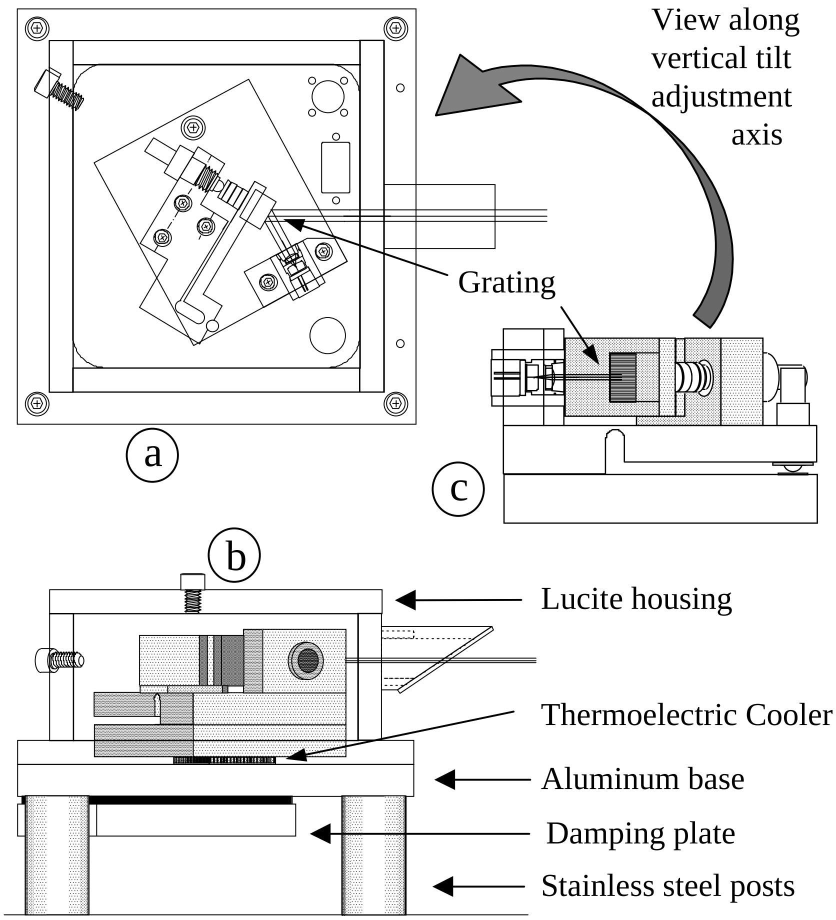
View along
vertical tilt
adjustment
axis
Grating
a
c
b
Lucite housing
Thermoelectric Cooler
Aluminum base
Damping plate
Stainless steel posts

Figure 2.8: CAD drawings of grating stabilized diode laser used for repump beam. The top view is shown in (a), with the beam path of the laser depicted. The rotation point of the grating arm is shown to be in the optimum position for maximum continuous tuning. The side view is depicted in (b), and shows the mounting assembly. In drawing (c) we can see another horizontal view of the laser which shows the tilt adjustment for the grating. The parts in (c) are all of the aluminum bronze parts. Views (a) and (c) show, respectively, the horizontal and vertical flexible joints and the associated 1/4 - 80 adjustment screws

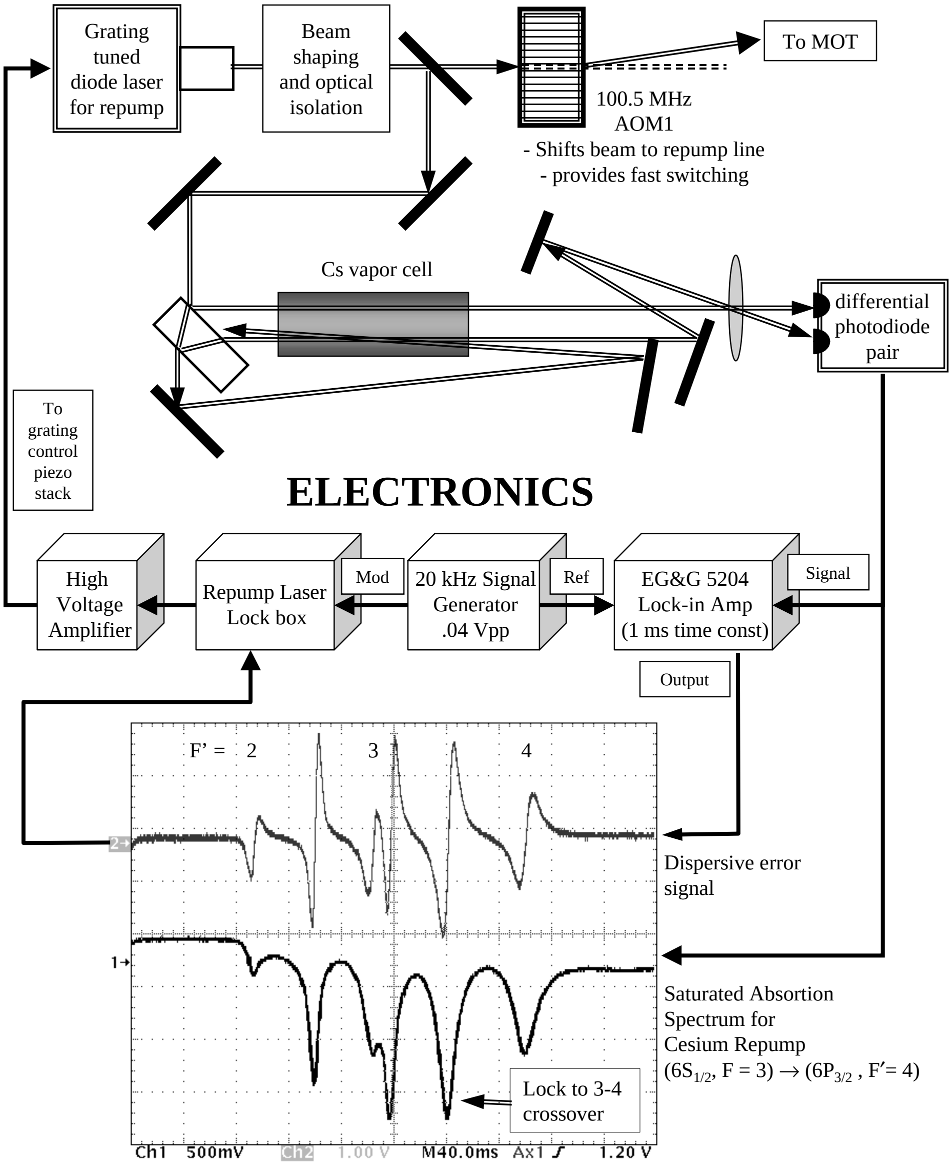
Grating tuned diode laser for repump
Beam shaping and optical isolation
To MOT
100.5 MHz AOM1
- Shifts beam to repump line
- provides fast switching
Cs vapor cell
differential photodiode pair
To grating control piezo stack
ELECTRONICS
High Voltage Amplifier
Repump Laser Lock box
Mod
20 kHz Signal Generator .04 Vpp
Ref
EG&G 5204 Lock-in Amp (1 ms time const)
Signal
Output
F' = 2
3
4
2
1
Dispersive error signal
Saturated Absorption Spectrum for Cesium Repump
(6S1/2, F = 3) → (6P3/2 , F′= 4)
Lock to 3-4 crossover
Ch1 500mV
Ch2 1.00 V
M40.0ms Ax1 ʃ 1.20 V

Figure 2.9: Diagram of saturated absorbtion lock for the grating tuned repump laser. The laser is locked to the strong $(6\mathrm{S}_{1/2}, F = 3) \longrightarrow (6\mathrm{P}_{3/2}, F' = 3, 4)$ crossover resonance via modulation and feedback to the grating piezos. The acousto-optic modulator used for the electronic switching then shifts the beam 100.5 MHz higher to the repump frequency.

2.4 The Interaction Laser

The interaction beam comes from a home built Ti:sapphire laser (L3 in Fig. 2.1), pumped with 8 W of blue and green light from a multi-line Coherent Innova 90 argon-ion laser (Pump laser in Fig. 2.1). The overall cavity layout is shown in Fig. 2.10. The main structure was originally used as a dye laser fashioned after the one used in our sodium experiments and described by previous students [7, 41]. We replaced the mirrors and the optical diode with elements coated for 852 nm. We also replaced the entire dye jet assembly with an adjustable mount for a Ti:sapphire crystal shown in Fig. 2.11 based on a crystal holder design by Jim Bergquist at NIST in Boulder Colorado.

The Ti:sapphire crystal, from Union Carbide, is 6 mm in diameter by 20 mm long. It is doped with 0.05% titanium, Brewster cut and polished on both ends for 852 nm, and has a guaranteed figure of merit ≥ 450.

We mounted it in a copper disk as shown in Fig. 2.11. A hole was cut through the disk at a 60° angle of incidence, and 0.002" smaller in diameter than the crystal. We then split the disk through almost the entire diameter of the disk with an electron drilling machine wire cut, 0.010" wide. This allowed the hole to spring open enough to insert the crystal, and then hold it in place.

Unfortunately, copper is not soft enough to deform around the crystal, so it only makes contact at three points. This is certainly not ideal for heat transfer, and probably applies some uneven stresses to the crystal as well. A suggestion for improvement would be to completely split the ring, and lay the crystal in an over-sized hole with some soft metal, such as indium, as a contact surface, then attaching the other half with some light tension.

We were able to cool the crystal somewhat by attaching a small copper tube to the top of the copper disk with thermal epoxy, and then running 10°C water through it. When the laser is off, the temperature of the copper disk stabilizes at about 17°C, then quickly (< 5 min) restabilizes to 26°C when the laser is turned on.

We tried several different output couplers to find the best reflection coefficient. We tried R = 90, 92, 95 and 97 percent values and ended up using the 6° P-polarized flat mirror with $R = 97.3\%$ at 852 nm. This ultimately gave us a total output power of 480 mW in a 1.5 mm diameter Gaussian beam, tunable around 852 nm.

The laser is tuned and stabilized in the same way as the dye lasers of the previous experiments mentioned earlier. The laser cavity is locked via the Hänsch-Couillaud lock scheme to a stable Invar reference cavity with a free spectral range of 1.5 GHz [42]. We then sweep tune the reference cavity with an internal Brewster plate attached to a galvo.

In order to accurately determine our wavelength, we first split part of the light to a NIST LM10 wavemeter which allows us to measure to within 500 MHz of the absolute wavelength. Then we split another beam into a 1.5 GHz free spectral range (FSR) scanning Fabry-Perot cavity ("Monitor Cavity" in Fig. 2.1), along with a collinear beam from the DBR laser which is locked 195 MHz below the $(6\mathrm{S}_{1/2}, F = 4) \longrightarrow (6\mathrm{P}_{3/2}, F' = 5)$ transition. Since the Ti:sapphire laser is shifted up by 80 MHz before going to the chamber, aligning the two Fabry-Perot signals assures us that the Ti:sapphire is 115 MHz below the line, plus some multiple of the 1.5 GHz FSR. Combining the fine Fabry-Perot measurement and the coarse wavemeter measurement gives us the absolute wavelength to within approximately 200 MHz. There is some drift of the reference cavity on the order of 100 MHz per hour, but this is small compared to the 6 GHz detuning we typically use and can be easily monitored and corrected. By default, the beam is directed to these devices whenever AOM3 is not switching the Ti:sapphire beam toward the chamber.

The beam that is used for the interaction is focused through a 50 μm pinhole for spatial filtering and collimated to produce a nearly Gaussian beam with a $1/e^2$ radius at the chamber of $w_0 = 1.5$ mm $\pm$ 10%.

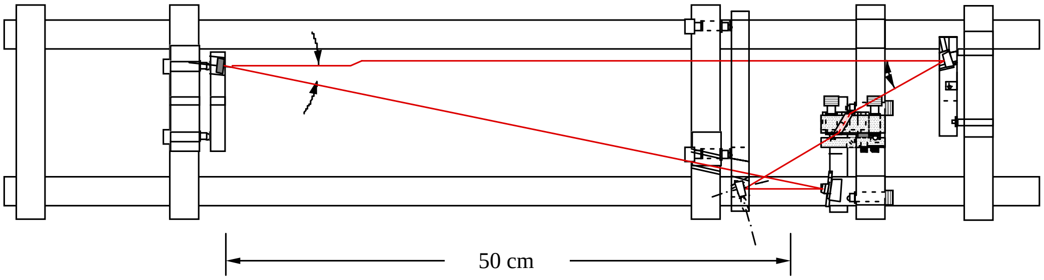

Figure 2.10: Diagram of overall layout of the Ti:sapphire laser cavity.

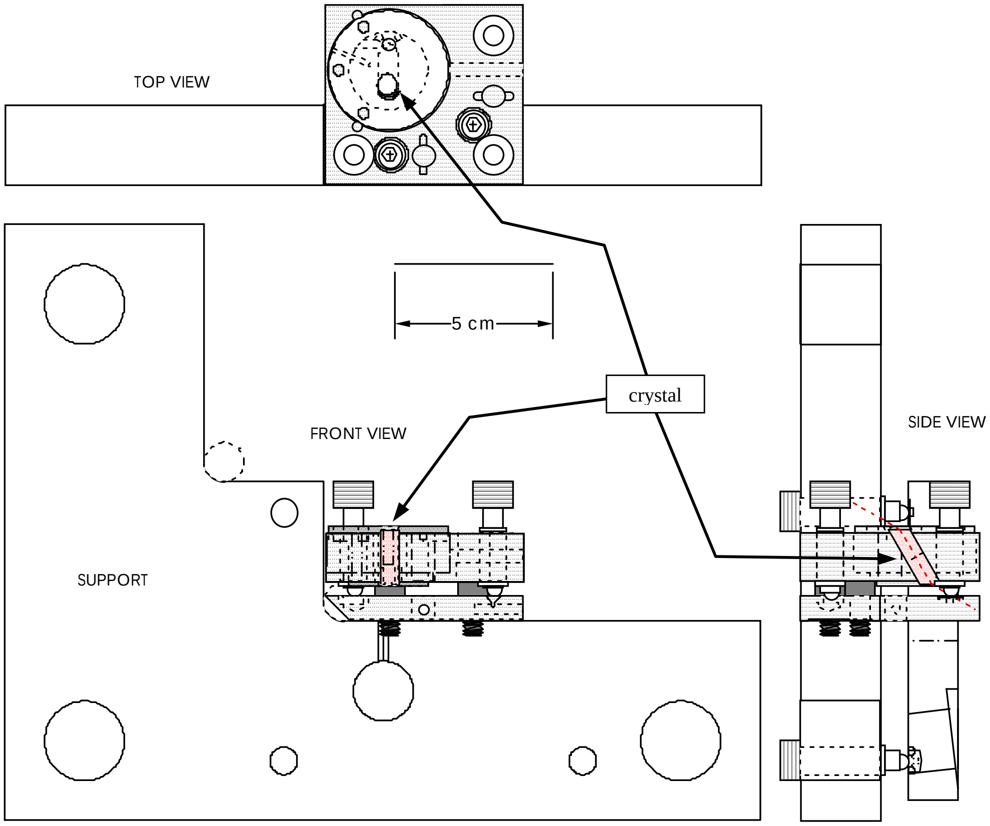
TOP VIEW
5 cm
crystal
FRONT VIEW
SIDE VIEW
SUPPORT

Figure 2.11: Drawings of design for Ti:sapphire crystal mount.

2.5 Measurement

Our observations of the dynamics of the atoms in the MOT all come from measurements of the atomic momentum distributions. The procedure for obtaining these atomic momentum distributions is outlined in Fig. 2.12. It consists of generating the initial conditions of a small cloud of cold trapped atoms, applying the desired interaction with the modulated standing wave, allowing the atoms to expand ballistically, and imaging them with a CCD camera.

2.5.1 Initial Conditions

We collect, localize, and cool our atoms in a magneto-optic trap (MOT) [18]. We use the trapping beams, repump beams, and magnetic trapping fields described previously to collect about 10^6 atoms in a radius of $\sigma_x = 150\,\mu\text{m}$. This initial load time takes about 5 to 7 seconds.

The momentum distribution is 94% Gaussian, as shown in Fig. 2.13. The remaining 6% forms a wide pedestal which raises the standard deviation of the distribution from the $4 \times 2\hbar k_L$ width of a Gaussian fit, to the roughly $9 \times 2\hbar k_L$ standard deviation which is seen in the analysis of our data in the following chapters. Previous work with molasses cooling has also produced non-Gaussian distributions [43]. While this pedestal is important for analysis of the momentum distributions, we use the Gaussian fit to characterize our temperature.

Our temperature measurement is done with a LabVIEW program, which automatically repeats the expansion sequence with no interaction phase, for a sequence of drift times ranging from about 10 to 30 ms. For each time step a Gaussian is fit to the integrated intensity distribution to extract the standard deviation width $\sigma_x(t)$. These values are recorded and plotted in the program versus the drift time, and then this data is fit to a function that

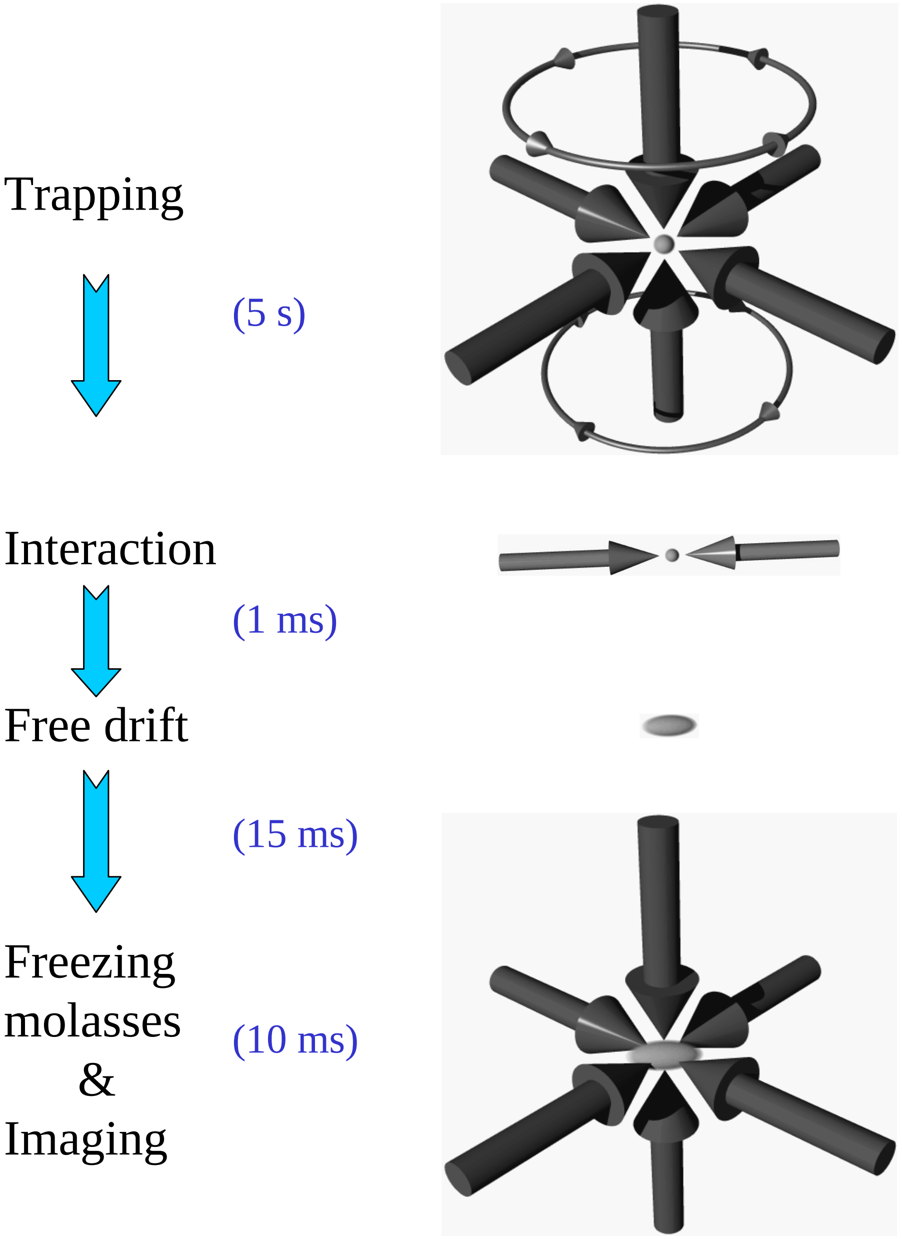
Trapping
(5 s)
Interaction
(1 ms)
Free drift
(15 ms)
Freezing
molasses
&
Imaging
(10 ms)

Figure 2.12: Experimental sequence for measurement of the momentum transfer caused the applied interaction.

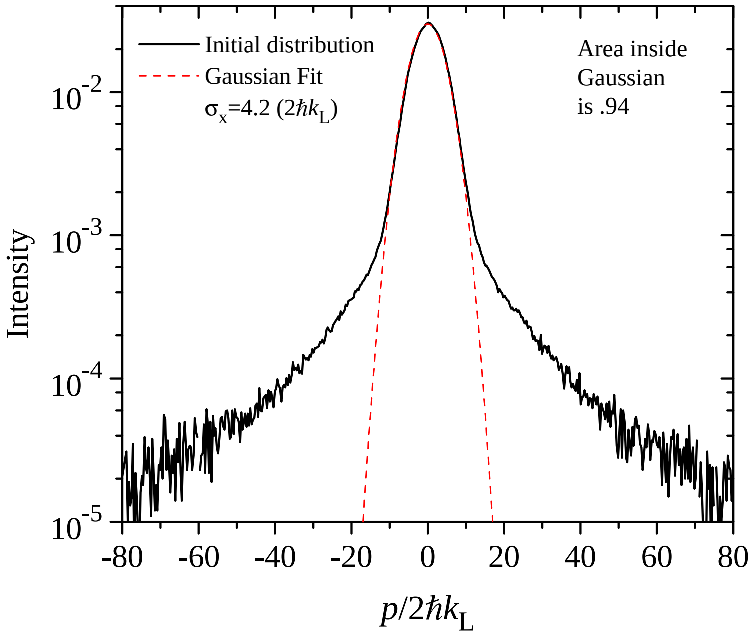

Figure 2.13: Example of our typical initial conditions and a comparison with a Gaussian fit. 94% of the atoms lie within the Gaussian profile.

includes the Gaussian convolution with the initial spatial width σ_{x0}.

$$\sigma_x(t) = \sqrt{\sigma_{x0}{}^2 + \left(\frac{\sigma_p}{M}\,t\right)^2} \tag{2.1}$$

An example of this measurement is shown in graph “G” in Fig. 2.14. It can be seen that the function is very linear after 15 ms, justifying the assumption that the initial spatial width of the MOT has little effect on our time-of-flight momentum measurements. We can get some measure of the consistency of our shot-to-shot temperature from the scatter of the data in the graph. Additionally, the program tracks the vertical centroid of the cloud to verify that it freefalls, and the total fluorescence to see that this is not critically dependent on the location or expanded width of the MOT.

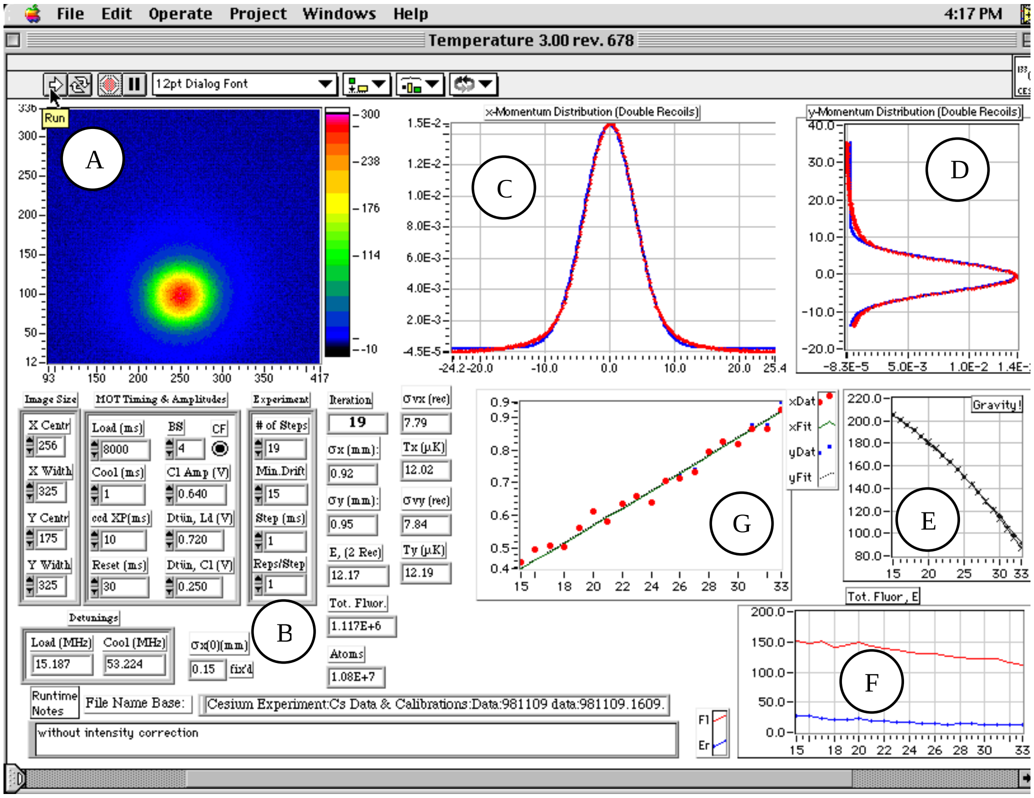
File
Edit
Operate
Project
Windows
Help
4:17 PM
Temperature 3.00 rev. 678
12pt Dialog Font
Run
A
B
C
D
E
F
G
x-Momentum Distribution (Double Recoils)
y-Momentum Distribution (Double Recoils)
xDat
xFit
yDat
yFit
Gravity!
Tot. Fluor, E
Fl
Er

Image Size
X Centr 256
X Width 325
Y Centr 175
Y Width 325

MOT Timing & Amplitudes
Load (ms) 8000
BS 4
CF ●
Cool (ms) 1
Cl Amp (V) 0.640
ccd XP(ms) 10
Dtün, Ld (V) 0.720
Reset (ms) 30
Dtün, Cl (V) 0.250

Experiment
# of Steps 19
Min.Drift 15
Step (ms) 1
Reps/Step 1

Iteration 19
σx (mm): 0.92
σy (mm): 0.95
E, (2 Rec) 12.17
Tot. Fluor. 1.117E+6
Atoms 1.08E+7

σvx (rec) 7.79
Tx (μK) 12.02
σvy (rec) 7.84
Ty (μK) 12.19

Detunings
Load (MHz) 15.187
Cool (MHz) 53.224

σx(0)(mm) 0.15 fix'd

Runtime Notes
File Name Base: Cesium Experiment:Cs Data & Calibrations:Data:981109 data:981109.1609.
without intensity correction

Figure 2.14: Example of a LabVIEW temperature measurement. Shows the last of a series of CCD pictures as the MOT expands (A), the measurement parameters (B), and the x (horizontal) and y (vertical) momentum distributions (C,D). Shown as a function of drift time are the vertical position of cloud (E), the total fluorescence (F), and the standard deviation of the x and y spatial distribution of the cloud as measured by the camera (G). The linearity of the data in (G) shows that the neither the magnetic field ringdown, nor the initial spatial width of the MOT are affecting the measurement. Also note that the overlay of the x and y data in (G) shows a uniform expansion.

The loading period leaves the atoms with a temperature of about 25 μK. During this time the trapping lasers are at full power, with the DBR detuned by 15 MHz. After this period we turn off the trapping fields, reduce the power of the DBR to about 40%, and increase the detuning to 40 MHz. Leaving this weakened molasses on for 1 ms produces some degree of polarization gradient cooling, and reduces our temperature to a typical value of 12 to 16 μK [17, 44]. Others have shown that this molasses cooling can reach less than 3 μK in cesium, but it depends on having residual magnetic fields of around 10 mG [43]. This is where the long decay time of our trapping field hurts us since most of our atoms are experiencing fields of hundreds of mG.

2.5.2 Interaction

Immediately after the final cooling stage the interaction sequence begins. Since the interaction beam detuning is roughly 10,000 times larger than the Zeeman shift due to the residual magnetic fields, and since the dipole force for the standing wave is independent of orientation or magnetic sublevel, the slow decay of our magnetic field should not affect the interaction. However, there are many other considerations associated with the interaction beam which are critical to characterizing the dipole potential in our Hamiltonian. We must characterize the temporal modulation, the spatial profile, the absolute power, and the quality of the standing wave both in the noise of the phase and amplitude, and the spatial purity (likeness to a perfect 1-D sinusoid). Finally, we must also consider the degree to which this is not a perfectly elastic dipole force interaction (i.e., the spontaneous emission rate).

The modulation of the interaction beam is accomplished using an 80 MHz AOM (AOM3 in Fig. 2.1) from IntraAction, which is specified to have a rise/fall time of 25 ns with its ME802 driver. In actuality we measure about 75 to 100 ns rise/fall time for the optical signal on a fast photodiode. This is primarily due to the 50 ns rise/fall time of the Stanford Research Systems DS345 arbitrary waveform generator creating our pulses, and to the AOM alignment being optimized for diffraction efficiency rather than speed. We anticipate improving this by incorporating a 2 ns RF switch between the oscillator and amplifier in the AOM driver. This modification would also

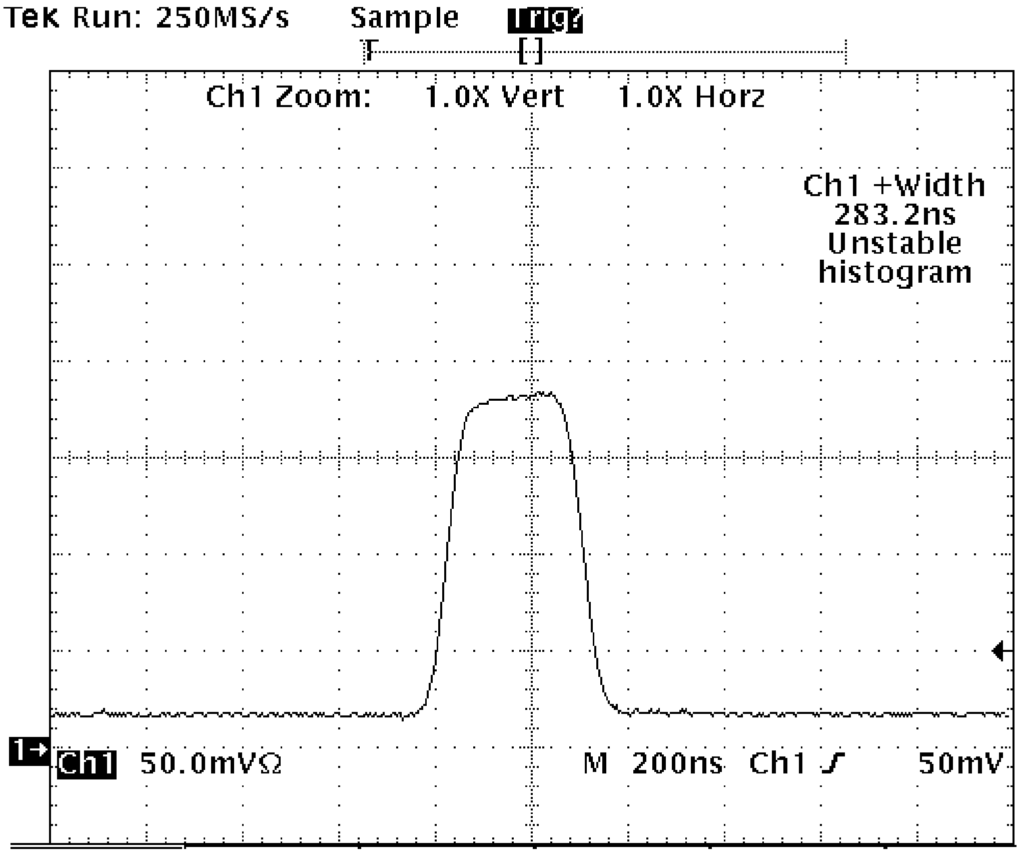

Figure 2.15: Example of actual pulse profile for delta kick

ensure that the RF signal driving the AOM is completely off, so that there is not any residual leakage of light through the AOM. We normally program square pulses of 300 ns, resulting in the pulse shape shown in Fig. 2.15, which has a FWHM of around 280 to 300 ns. The effect of this pulse shape will be discussed in the next chapter.

The absolute amplitude of our interaction beam is measured with a Newport 1825C power meter and a calibrated (±5%) 818SL attenuated detector. In order to monitor the pulse amplitude during the experiment we split off 1% of the interaction beam before it enters the chamber and focus it into the 50 MHz Thorlabs photodiode shown in Fig. 2.19. The diode is calibrated against the power meter using a dedicated LabVIEW program which simulaneously reads the analog output from each device as it steps through the entire power range of the interaction beam with AOM3. It then fits a line to this data and extracts a calibration value for the diode signal in mW/mV.

The pulse sequence for each interaction is stored by a Tektronix TDS 524A digital oscilloscope, and read via GPIB into the LabVIEW program controlling the experiment for analysis. Since the maximum kick strength K_{eff}, depends on the total pulse energy, as we will see in equation 3.4, we want to be able to extract a value for the average integrated energy per pulse. In order to store an entire 70 kick pulse sequence we had to decrease the scope resolution to a level which only sampled a few points per pulse. Therefore, rather than use this trace to integrate the pulse sequence, which would likely underestimate the true pulse energy because of the few data points, we made a reference table of pulse energy versus pulse amplitude for pulses of various pulse widths that were measured at high resolution. Hence, we needed only to extract the pulse amplitude from the low resolution trace. This can be done very reliably.

The inherent pulse-to-pulse amplitude noise on the laser can be determined from the standard deviation of the pulse amplitude measurements. This σ seems to be consistently less than 1% of the maximum pulse amplitude available.

We measure the beam radius in two ways. The first is with an improved "knife edge" method from the one described in detail by Robinson [7]. The second is with a home-made beam profiling system.

Our knife edge consists of two razor blades mounted perpendicular to each other on a 2-D translation device placed in the interaction beam path shortly after the spatial filter. We place a power meter after the razors, and then read the analog output into the computer via another LabVIEW program as we translate the razors through the beam. We do this first in one direction, and then in the other. The signals represents a 1-D integration of the beam profile in each direction, and the program fits an integrated 2-D Gaussian to the data as shown in Fig. 2.16. These fits suggest that the profile in each direction is nearly Gaussian with some overall ellipticity.

Our beam profiling system requires directing a split-off and attenuated beam right on to the chip of a small CCD camera, and then recording and analyzing the crossection with a frame grabber device and the computer. This has the advantage of analyzing both directions at the same time and directly comparing the results to a Gaussian fit. Measurements from the knife edge method and the CCD method are shown in Figs. 2.16 and 2.17. We complete this analysis for both the input and the retroreflected beams in order to see that it is not substantially converging or diverging on its way to the chamber.

While the CCD measurement of the beam width generally agrees with the knife edge to within 10%, it seems less reliable due to the pronounced interference pattern that reflections of the chip generate from the coherent input beam. These patterns distort the image, making the data harder to fit. Additionally the image seems sensitive to variation of laser intensity and location on the chip.

Once the beam profile was determined, we examined noise effects. Retroreflection of the interaction beam by an external mirror creates the standing wave and defines its spatial phase. The mirror is in an adjustable mirror mount attached to the opposite side of the chamber with four steel posts. Any motion of this mirror due to acoustic vibration during the interaction will constitute phase noise, the effect of which we have not yet been able to

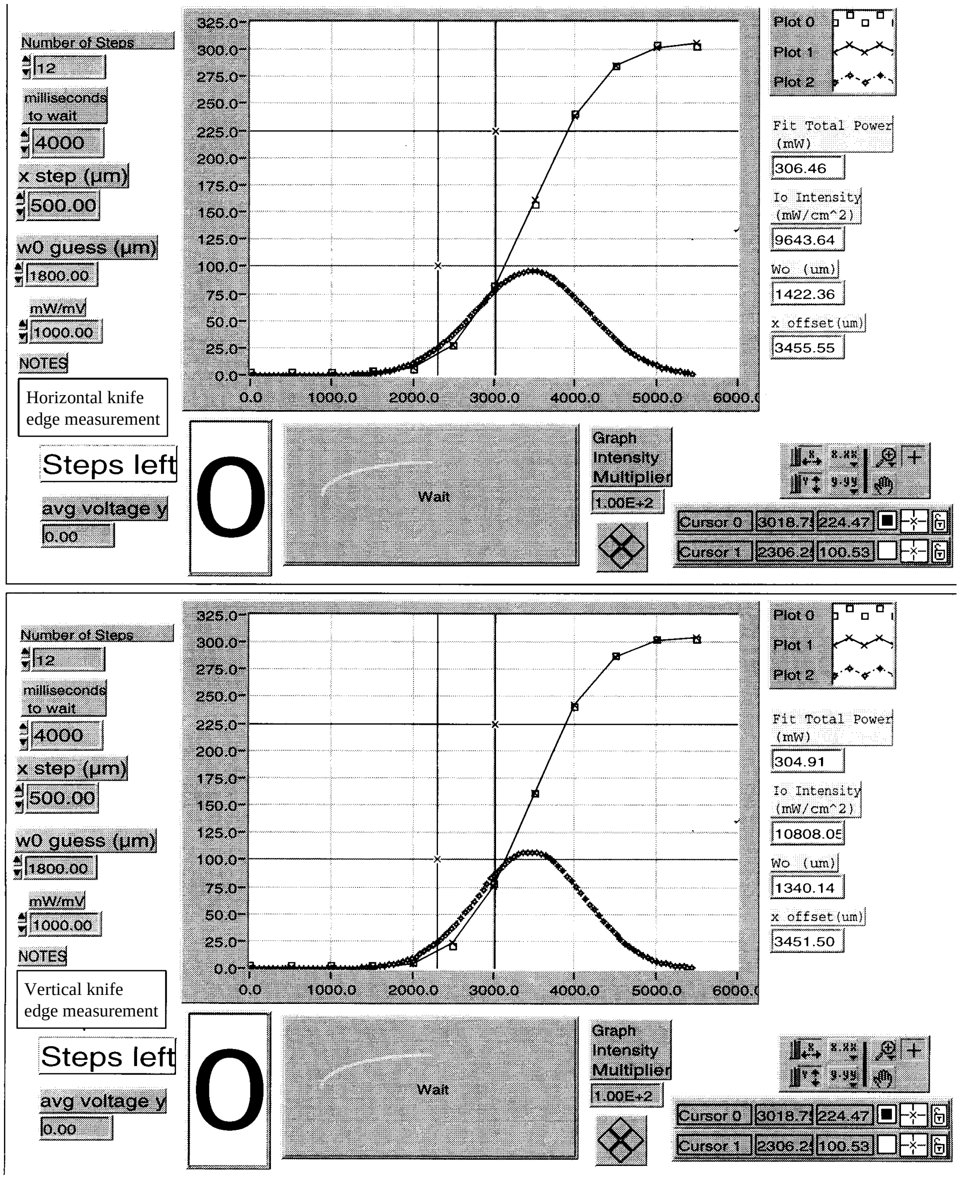
325.0
300.0
275.0
250.0
225.0
200.0
175.0
150.0
125.0
100.0
75.0
50.0
25.0
0.0
0.0
1000.0
2000.0
3000.0
4000.0
5000.0
6000.
Plot 0
Plot 1
Plot 2
Wait

Number of Steps 12

milliseconds to wait 4000

x step (μm) 500.00

w0 guess (μm) 1800.00

mW/mV 1000.00

NOTES

Horizontal knife edge measurement

Steps left 0

avg voltage y 0.00

Fit Total Power (mW) 306.46

Io Intensity (mW/cm^2) 9643.64

Wo (um) 1422.36

x offset(um) 3455.55

Graph Intensity Multiplier 1.00E+2

Cursor 0 3018.7 224.47

Cursor 1 2306.2 100.53

Number of Steps 12

milliseconds to wait 4000

x step (μm) 500.00

w0 guess (μm) 1800.00

mW/mV 1000.00

NOTES

Vertical knife edge measurement

Steps left 0

avg voltage y 0.00

Fit Total Power (mW) 304.91

Io Intensity (mW/cm^2) 10808.0

Wo (um) 1340.14

x offset(um) 3451.50

Graph Intensity Multiplier 1.00E+2

Cursor 0 3018.7 224.47

Cursor 1 2306.2 100.53

Figure 2.16: Example of knife edge program in LabVIEW for measuring the interaction beam profile is shown for both the horizontal and vertical directions. The squares are data points obtained from measuring power as the knife edge cuts accross the beam. The diamonds plot the Gaussian function obtained from the fit to the squares.

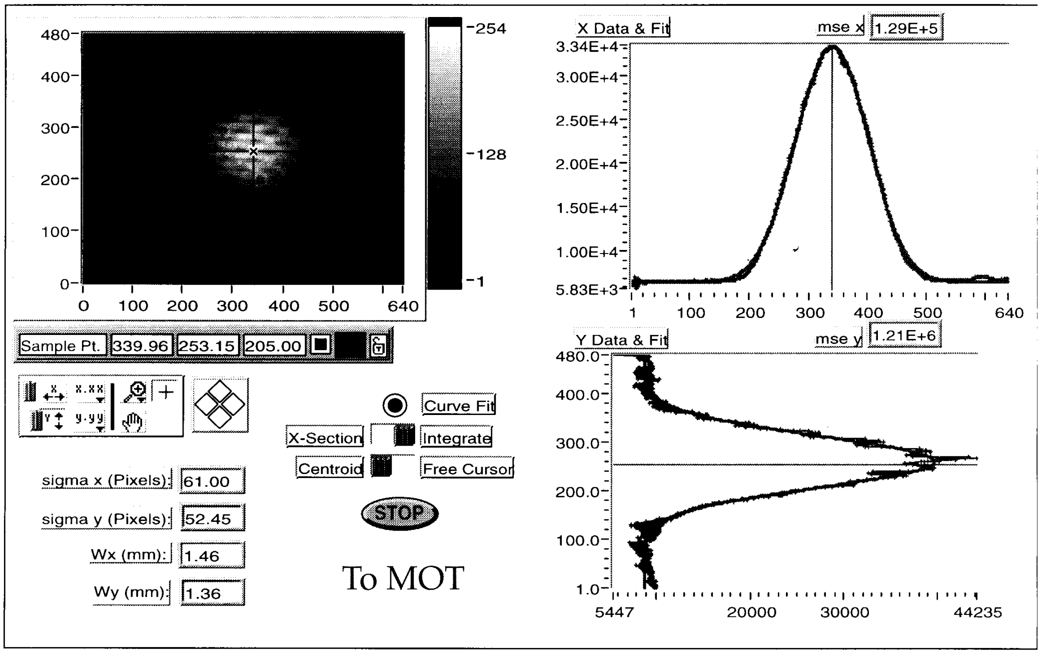
480
400
300
200
100
0
0 100 200 300 400 500 640
-254
-128
-1
X Data & Fit
3.34E+4
3.00E+4
2.50E+4
2.00E+4
1.50E+4
1.00E+4
5.83E+3
1 100 200 300 400 500 640
Y Data & Fit
480.0
400.0
300.0
200.0
100.0
1.0
5447 20000 30000 44235
● Curve Fit
X-Section
Integrate
Centroid
Free Cursor
STOP
To MOT

Sample Pt. 339.96 253.15 205.00

mse x 1.29E+5

mse y 1.21E+6

sigma x (Pixels): 61.00

sigma y (Pixels): 52.45

Wx (mm): 1.46

Wy (mm): 1.36

Figure 2.17: Example of a beam profile measurement using a CCD camera.

characterize. We have, however, attempted to characterize the level of phase noise present.

To do this we set up a Michelson interferometer on a large damped post (from Newport) set where the interaction beam enters the chamber. One arm is sent through the chamber to the retroreflecting mirror and the other to a mirror on the post. A helium-neon laser was used to generate the fringes, which were measured by a photodiode and viewed on an oscilloscope. The results showed that over the time of our longest interactions (100 kicks, or 2 ms) there was a phase shift of less than 8% of a spatial period of 0.5×852 nm, with the highest frequency oscillations being on the order of 600 Hz. This should represent an upper bound since the interferometer could not distinguish between motion of the retroreflecting mirror or motion of the other elements. We have since replaced a mechanical shutter, which was on the table and was the source of much of the acoustic noise during these measurements, with AOM1.

Finally, we consider the quality of the standing wave. Problems in the spatial profile can come from stray reflections, phase front distortion, or mismatch of the counter propagating beams. Recent work has shown that these experiments can be very sensitive to imperfections in the standing wave [45]. Also, the conservative interaction can be made dissipative by spontaneous emission events.

The 4σ radius of our MOT is about 0.5 mm, so we want the phase front to not change much over this transverse distance. For a beam radius of 1.5 mm, the radius of curvature of the phase front, even if the MOT is 4 m from the waist, is 20 m. This means that at most the phase shift in a given plane at this distance from the beam axis is 0.7%, which reduces the standing wave intensity by less than 1%. So curvature is not a problem. Our mirrors have flatness on the order of $\lambda/10$ so this also is less than a 1% change over this distance.

The coherence length of our interaction beam is at least $x_{\mathrm{c}} = c/\delta\nu_{\mathrm{c}} \approx 30$ m. This assumes an upper limit on the bandwidth of our Ti:sapphire laser of $\delta\nu = 10$ MHz, as determined by a Fabry-Perot cavity with 10 MHz resolution.

There is about a 3% drop in intensity in the retroreflected beam due to optical losses, which corresponds to a 1% drop in the standing wave amplitude. Reflections from the anti-reflection coated windows are on the order of 0.5% each, and so should only produce very weak fringes if any.

Ideally, our standing wave potential is non-dissipative. Any deviation from this would also have to be considered a degradation of our ideal interaction. Therefore we must consider to what degree residual spontaneous emission is present for our experimental parameters.

Spontaneous emission caused by the far-detuned, linearly polarized standing wave is given by Eq. (2.2) [21].

$$R_{\mathrm{sc}} = \left(\frac{\Gamma}{2}\right) \frac{(I/I_{\mathrm{sat}})}{1 + 4(\Delta/\Gamma)^2 + (I/I_{\mathrm{sat}})}, \tag{2.2}$$

where $I_{\mathrm{sat}} = 1.65$ mW/cm^2.

For our maximum power $P \sim 300$ mW. Including both beams, the average intensity is about $I_{\mathrm{av}} = 1.4 \times 10^4$ mW/cm^2, giving a scattering rate of $R_{\mathrm{sc}} = 32$ kHz, or 0.9% probabilty of spontaneous emission per 285 ns pulse for each atom. Our normal operating parameters use about 50% - 60% of that power, inducing a 0.4% - 0.5% probability of spontaneous emission per pulse.

2.5.3 Free Drift

The next step in the sequence after the interaction is the ballistic expansion (free drift) time. With all of the lasers off, the atoms are allowed to freefall and spread out in space in accordance with their respective velocities. There were two requirements here. The first is that the atoms are allowed to drift long enough to achieve a spatial spread much larger than the initial spatial width of the MOT, or any expansion occuring during the interaction. The second requirement was that they must not expand beyond the view of the camera or the uniform region of the detection molasses.

We typically use 15 ms of drift time, measured from the beginning of the interaction. We have already seen that the initial MOT size was insignificant for this expansion, but there was some error in the measurement from momentum gained toward the end of the interaction time. If atoms are largely accelerated toward the end of the 1.6 ms interaction time, they will have drifted with this added momentum for 10% less time than we are assuming (the ratio of the interaction time to the drift time). If the acceleration from the diffusion in momentum was constant during the 1.6 ms interaction time, a 5% error in the momentum calculation (10% in the energy) would result. In our kicked rotor experiments, however, most of the momentum is gained in the beginning of the interaction time, due to localization effects, so this error is reduced somewhat.

2.5.4 Imaging

The free drift time is terminated by switching on the molasses beams, this time without the magnetic fields. Without the B-field there is no restoring force, so the molasses simply cools the atoms in place down to the initial MOT temperature. The resulting fluorescence is imaged by a CCD camera.

The imaging is done with a TE/CCD-5122TK/1UV thermoelectrically cooled CCD camera from Princeton Instruments. The CCD chip itself is cooled to -50°C. It has a 512×512 pixel array, and each pixel is about a 20 μm square. A Nikon 105 mm f/2.8D lens provides a 1:1.8 magnification for about 36 μm resolution. There is a shutter opening/closing time of about 5 ms, so for accurate exposure timing we depend on the switching of the molasses with AOM1 and AOM2.

Sample images are shown in Fig. 2.18. Above each image is a graph of the vertically integrated intensity distribution, which gives the 1-D momentum distribution along the direction of the standing wave. The horizontal scale for the momentum is determined in the same way as for the temperature measurement; by appropriately considering the drift time that led to the expanded distribution.

Our large, powerful molasses beam, described earlier, ensures that we have a sufficiently uniform atomic fluorescence rate over the entire 1.8 cm image. In fact, at a distance of 9 mm from the center, the intensity has dropped by 35%. Because of the very small percentage of the distribution outside of the central region of the beam, this intensity drop has little effect on the distributions, and less than 10% reduction in measured average energy.

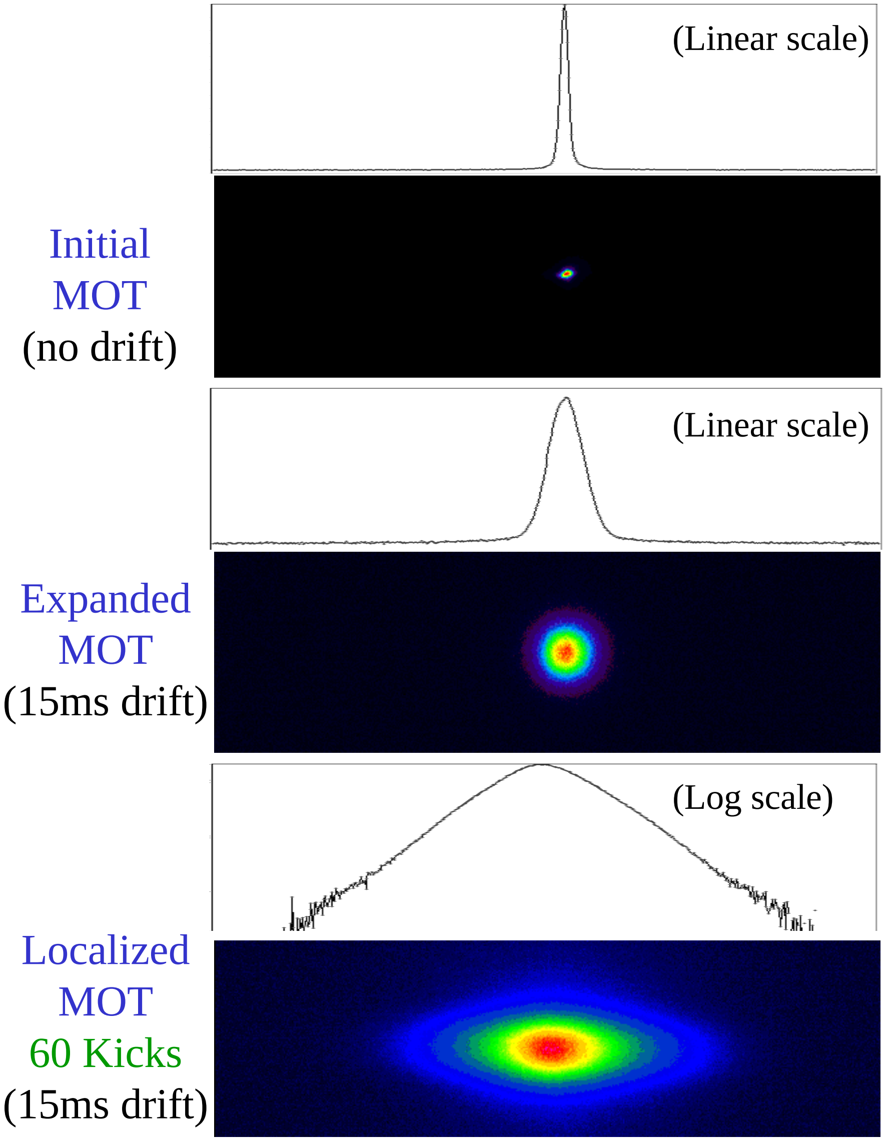

Figure 2.18: Examples of CCD images taken at the end of the experimental sequence, and the associated 1-D integrated intensity graphs. The unexpanded atomic cloud in the first frame represents the actual spatial dimensions of the MOT, and is clearly much smaller than the expanded clouds in the next two frames, which are used for the momentum measurements.

2.6 Computer Control

The entire measurement procedure was necessarily automated because of the need for precise timing. Our computer control chain is shown in Fig. 2.19. We use a Power Macintosh 7100/80 computer running LabVIEW 4.0. Three internal NuBus I/O boards provide the connection to all external instrumentation. The timing for the signals produced in the control sequence is depicted in Fig. 2.20.

The last of the three boards in the control diagram in Fig. 2.19 is a buffer board for the Princeton Instruments CCD camera. It has a serial connection to the ST-138 camera controller through which it passes programming commands to the camera, and receives image data from the camera. Once programmed, the camera shutter control is actually accomplished by an independent timing signal to the external trigger input on the controller.

The middle board is a National Instruments NB-MIO-16L-9 multipurpose I/O board. It is connected to a buffered interface panel which provides protection for the MIO board, and easy BNC connections to the various I/O data lines. While we often use the analog inputs for automated measurements, the actual experiment just uses two of this board's programmable clocks for timing signals. One controls the MOT coils, and the other provides the main trigger for initiating the experiment.

The first board is our GPIB interface. It is a National Instruments NB-DMA2800 which programs all of our timing and control devices, and reads our interaction beam waveform from the oscilloscope. We use three Stanford Research System DS345 arbitrary waveform generators to control the AOMs that precisely modulate the amplitudes of all of the laser beams used in the experiment. A SRS DG535 pulse generator provides two pulses which directly control the camera shutter and the molasses detuning frequency via AOM2.

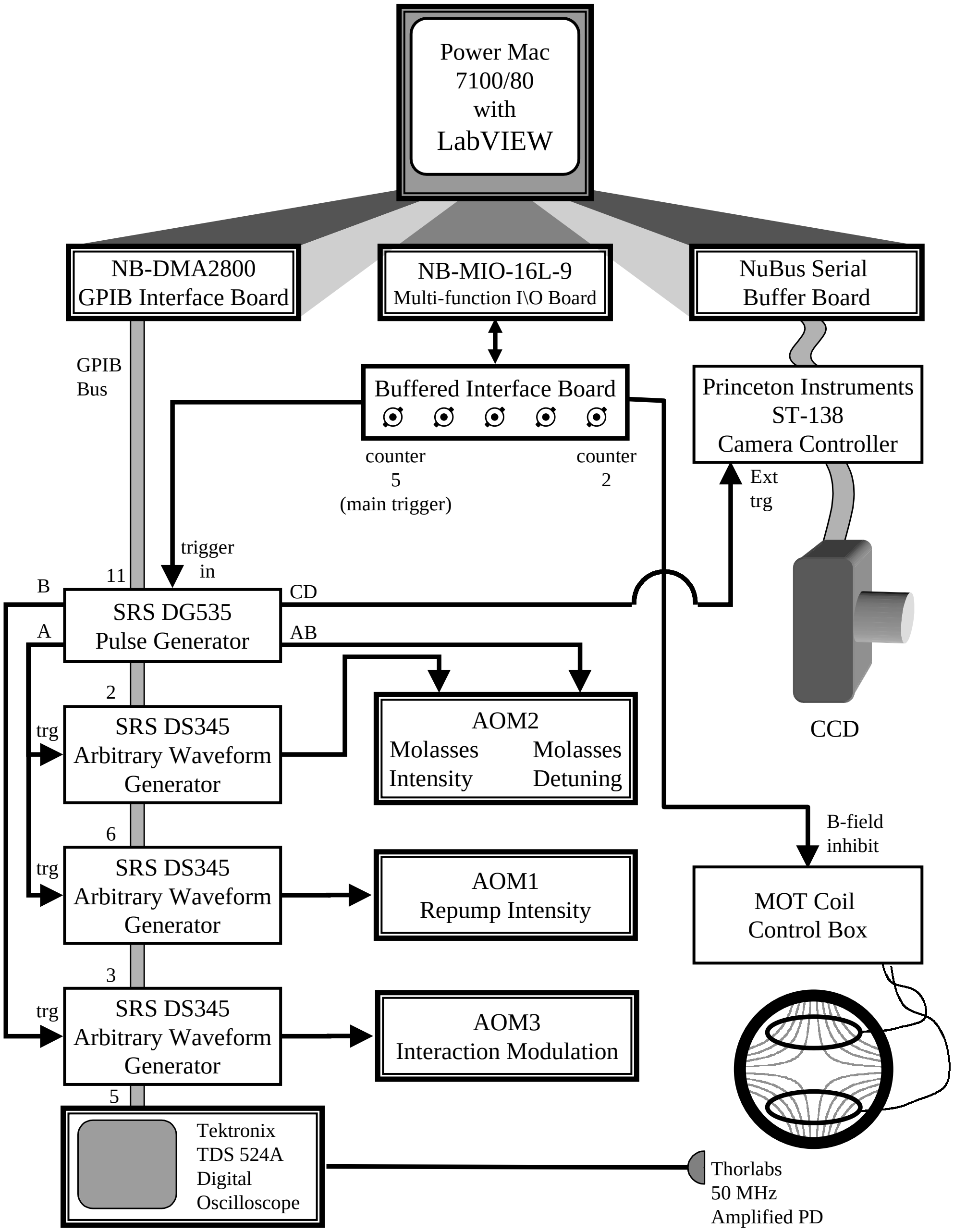
Power Mac
7100/80
with
LabVIEW
NB-DMA2800
GPIB Interface Board
NB-MIO-16L-9
Multi-function I\O Board
NuBus Serial
Buffer Board
GPIB
Bus
Buffered Interface Board
Princeton Instruments
ST-138
Camera Controller
counter
5
(main trigger)
counter
2
Ext
trg
trigger
in
B
11
CD
SRS DG535
Pulse Generator
A
AB
CCD
2
trg
SRS DS345
Arbitrary Waveform
Generator
AOM2
Molasses
Intensity
Molasses
Detuning
B-field
inhibit
6
trg
SRS DS345
Arbitrary Waveform
Generator
AOM1
Repump Intensity
MOT Coil
Control Box
3
trg
SRS DS345
Arbitrary Waveform
Generator
AOM3
Interaction Modulation
5
Tektronix
TDS 524A
Digital
Oscilloscope
Thorlabs
50 MHz
Amplified PD

Figure 2.19: Diagram of experimental control organization.

The edges of these pulses provide triggers for the DS345s.

LabVIEW provides a fast, easy, and flexible graphical programming language for automating the experiment. We have created a set of modular programs, each corresponding to a different type of experiment. Each program is designed to perform a sequence of experiments with preprogrammed parameter steps, displaying, analyzing, and storing the data as it goes. In addition to the main programs used for taking the data presented here, we regularly construct many other programs to automate calibration and analysis outside the experiment.

We eventually hope to upgrade the computer to a PC.

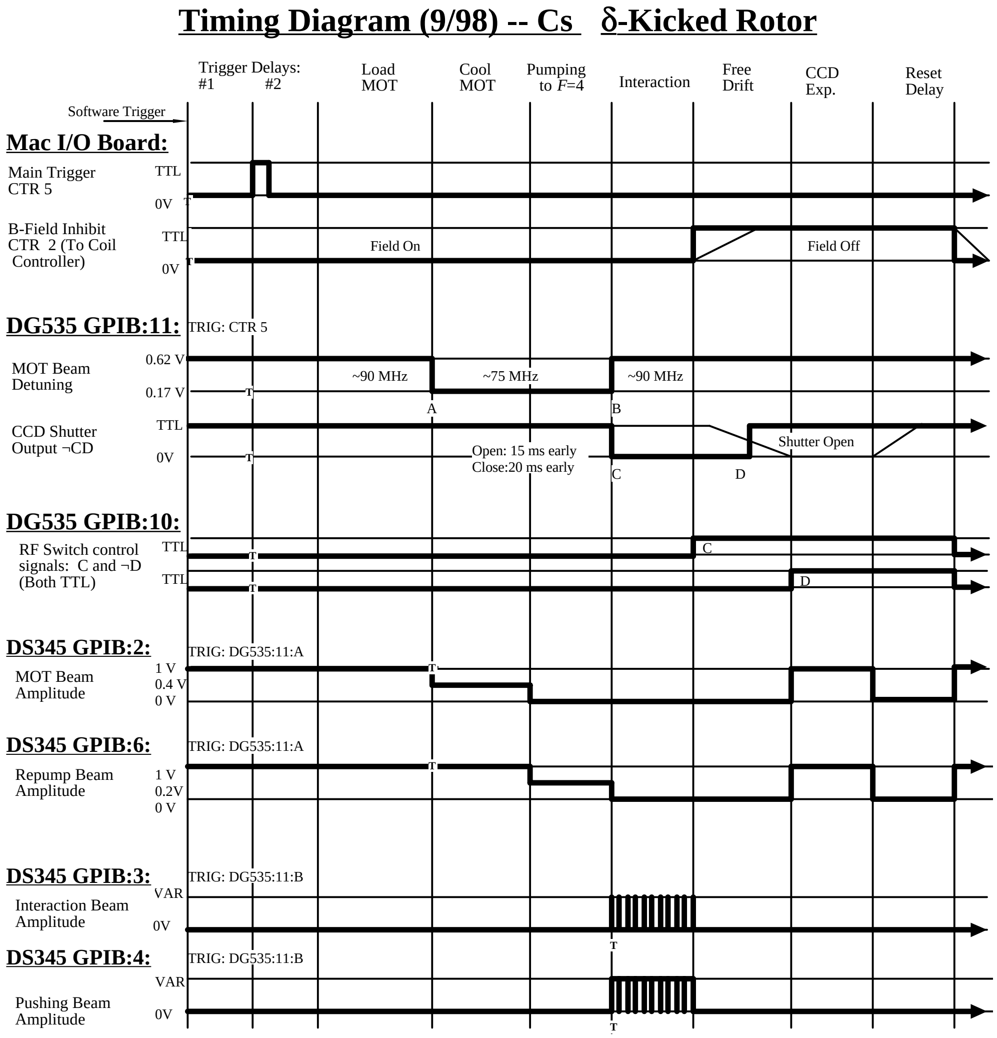
Timing Diagram (9/98) -- Cs δ-Kicked Rotor
Trigger Delays: #1 #2
Load MOT
Cool MOT
Pumping to F=4
Interaction
Free Drift
CCD Exp.
Reset Delay
Software Trigger
Mac I/O Board:
Main Trigger CTR 5
TTL
0V
B-Field Inhibit CTR 2 (To Coil Controller)
TTL
0V
Field On
Field Off
DG535 GPIB:11:
TRIG: CTR 5
MOT Beam Detuning
0.62 V
0.17 V
~90 MHz
~75 MHz
~90 MHz
A
B
CCD Shutter Output ¬CD
TTL
0V
Open: 15 ms early
Close:20 ms early
C
D
Shutter Open
DG535 GPIB:10:
RF Switch control signals: C and ¬D (Both TTL)
TTL
TTL
C
D
DS345 GPIB:2:
TRIG: DG535:11:A
MOT Beam Amplitude
1 V
0.4 V
0 V
DS345 GPIB:6:
TRIG: DG535:11:A
Repump Beam Amplitude
1 V
0.2V
0 V
DS345 GPIB:3:
TRIG: DG535:11:B
Interaction Beam Amplitude
VAR
0V
DS345 GPIB:4:
TRIG: DG535:11:B
Pushing Beam Amplitude
VAR
0V
T

Figure 2.20: Timing diagram. Once the main trigger is given by the computer, the high resolution timing and signal generation is accomplished by the Stanford Research Systems components.

Chapter 3

Pushing Back the Boundaries

3.1 Introduction

The first series of experiments with cesium were designed to demonstrate our ability to study quantum chaos in regimes that were out of reach of the previous experiments in sodium. There were two important differences. First, we made significant technical improvements which gave us a better quality signal with a higher signal-to-noise ratio. Second, fundamental differences in the new system, which will be explained shortly, allowed us to push out the classical momentum boundary imposed by the finite pulse duration of our interaction beam [13].

Figure 3.1 demonstrates the effectiveness of our new apparatus on a typical data run. The momentum distribution on the top is from the sodium experiment and shows a dynamic range of about 40 in the measured fluorescence intensity. The bottom distribution from the new experiment has a dynamic range of about 400, and a much cleaner signal. Most of this improvement can probably be attributed to the chamber windows being larger, facilitating the use of larger trapping beams, and having anti-reflection coatings. Both changes contribute to less fringes being imposed on the beams due to diffraction and multiple reflection interference (responsible for the shoulder on the sodium distribution), and both reduce the amount of scattered light in the chamber, improving the signal-to-noise ratio. What cannot be seen on

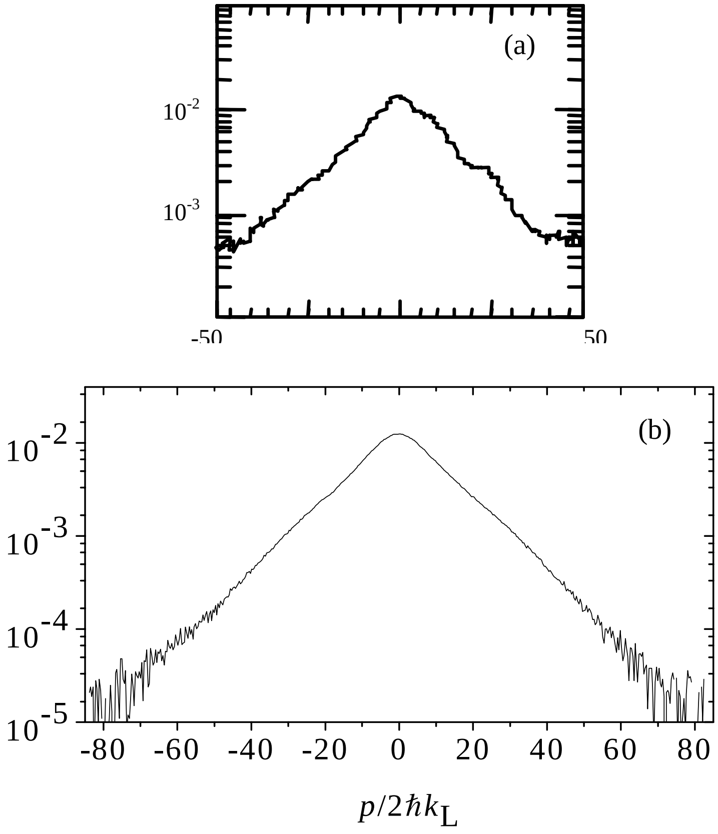

Figure 3.1: Comparison of sodium data (a) [7] to cesium data (b). Both distributions are localized momentum distributions. The vertical axes are intensity in arbitrary units. The horizontal axes are in momentum units of two double-photon recoils (w.r.t. each element). Notice that the signal to noise ratio is significantly improved in the lower graph, and a much wider momentum range is possible.

here is the effect of the boundary.

3.2 Classical Analysis of the Momentum Boundary

It turns out that even if the apparatus were the same, the sodium data shown here could not have extended any further because there was a classical momentum boundary in phase space, at $p/2\hbar k_{\mathrm{L}} = 50$, beyond which the classical dynamics are predominantly regular. The origin of this boundary can be explained with a simple classical model which provides us with relevant scaling parameters and makes clear the advantage of using cesium rather than sodium.

Consider an atom with a velocity v such that it travels one period of the standing wave during a kick of duration t_{p}. Then the momentum transferred to the atom by the potential averages to zero, and the particle no longer diffuses. This situation occurs when $vt_{\mathrm{p}} = \lambda/2$, and hence provides an estimate for the boundary location given by

$$\frac{p_{\mathrm{boundary}}}{2\hbar k_{\mathrm{L}}} = \frac{M\lambda^2}{8\pi\hbar t_{\mathrm{p}}}. \tag{3.1}$$

From this equation we see that the larger mass of cesium and longer optical wavelength of the cesium transition provide a twelve-fold increase over sodium in the momentum boundary location for a given pulse width.

A more precise description of the boundary and its dependence on pulse width can be obtained from a Fourier analysis of the interaction potential. We accomplish this by rewriting the sequence of kicks as a discrete Fourier series and analyzing the amplitudes of the primary resonances of the system. Applying this to the scaled Hamiltonian (1.31), we have

$$H = \rho^2/2 + \kappa \sum_{m=-\infty}^{\infty} \tilde{f}(2\pi m)\cos(\phi - 2\pi m\tau), \tag{3.2}$$

where $\tilde{f}(2\pi r)$ is the Fourier transform of the pulse function $f(\tau)$. This Hamiltonian has primary resonances located at $\rho = d\phi/dt = 2\pi m$. Therefore, the Fourier transform evaluated at $m = \rho/2\pi$ modifies the effective stochasticity parameter K_{eff} as a function of momentum such that

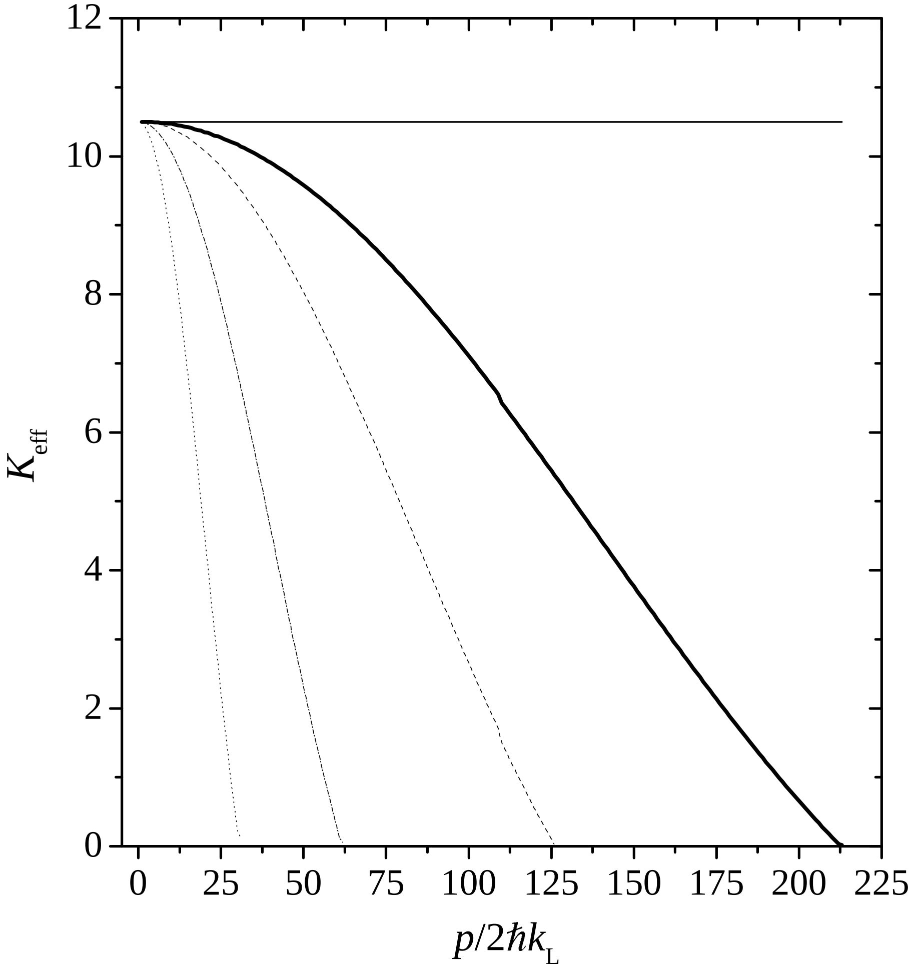

Figure 3.2: Classical calculation of the effective stochasticity parameter K_{eff} as a function of momentum for square pulses of various temporal widths. The horizontal line represents the δ-kick case. The other curves represent square pulses with widths $\alpha = 0.014$ (heavy solid line), $\alpha = 0.024$ (dashed), $\alpha = 0.049$ (dash-dot), and $\alpha = 0.099$ (dotted). The well depth is adjusted in each case to give the same maximum value of $K_{\mathrm{eff}} = 10.5$ at $p/2\hbar k_{\mathrm{L}} = 0$. The point where K_{eff} drops to $\sim$1 in each case is the classical momentum boundary. The typical limit of our momentum measurements is $|p/2\hbar k_{\mathrm{L}}| \approx 80$. Note that we have suppressed the curves after their first zero-crossing.

$$K_{\text{eff}}(\rho) = \kappa\tilde{f}(\rho) \tag{3.3}$$

Notice that for $\rho = 0$ this is just the Fourier transform evaluated at the origin, which is the area under the pulse. Recalling Eq. 1.30 for α we have

$$K_{\text{eff}}(0) = \kappa\tilde{f}(0) = \kappa \int\limits_{-\infty}^{\infty} f(\tau)\mathrm{d}\tau = \kappa\alpha. \tag{3.4}$$

Therefore, the effective stochasticity parameter for small momentum values is proportional to the total energy in each pulse of the interaction beam, independent of the shape.

For a square pulse, which approximates the pulse used in our experiments, the effective kick strength can be written as

$$K_{\text{eff}} = \alpha k \frac{\sin(\alpha\rho/2)}{\alpha\rho/2}, \tag{3.5}$$

where $K_{\text{eff}}(\rho = 0) = \alpha\kappa$ agrees with the general estimate above for the stochasticity parameter K of the δ-kicked rotor.

This dependence of K_{eff} on momentum is displayed in Fig. 3.2, which compares several square-pulse cases to the δ-kick case. Notice that the first zero-crossing of this expression corresponds to the value obtained from Eq. (3.1). Recall from Section 1.3.3 that as the stochasticity parameter increases from zero the last KAM surface bounding the momentum transport is broken at $K \sim 1$. Therefore the dynamics of the finite pulse system undergo a transition as K_{eff} drops to $\sim$1, because of the presence of these KAM surfaces that span the phase space and act as a barrier against momentum diffusion.

This momentum boundary is illustrated in Fig. 3.3, which shows classical phase portraits for the δ-kicked rotor (Fig. 3.3a) and two square-pulse cases (Figs. 3.3b and 3.3c). The phase portrait of Fig. 3.3b is typical of our

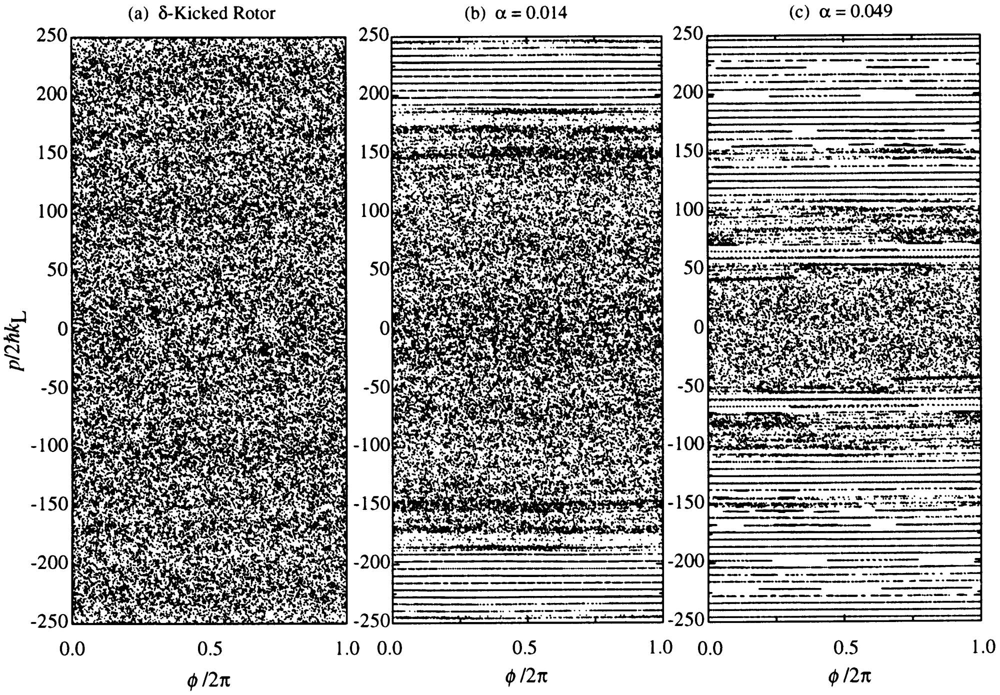

Figure 3.3: Classical phase portraits for the kicked rotor with $K = 10.5$, comparing δ-kicks (a) to square pulses of widths $\alpha = 0.014$ (b) and $\alpha = 0.049$ (c). Case (b) is typical for our localization experiments. This case mimics the δ-kicked rotor for a momentum region much larger than that used in our experiments ($|p/2\hbar k_\mathrm{L}| \lesssim 80$).

current cesium experiment, and the boundaries are well outside the range of detectable atomic momenta, $|p/2\hbar k_\mathrm{L}| \lesssim 80$. Our group's previous experimental work in sodium was limited to a bounded chaotic region similar to that in Fig. 3.3c. While this situation enabled the observation of the transition from the short time classical diffusion to the exponential localization of the momentum distribution after the quantum break time, it could not be used to explore any continued momentum growth beyond that point which might be caused by some source of delocalization.

Fig. 3.4 shows momentum distributions from classical Monte-Carlo simulations (with 2×10^5 particles) of the same systems as in Fig. 3.3. The momentum distributions after 68 kicks are plotted here. The distributions are similar in the central region, but the boundary suppresses diffusion in the wings of the distributions in the square-pulse cases, especially in the case with the widest pulses ($\alpha = 0.049$). The nearly Gaussian initial momentum distribution is also plotted, and it corresponds to the initial distribution in the experiments.

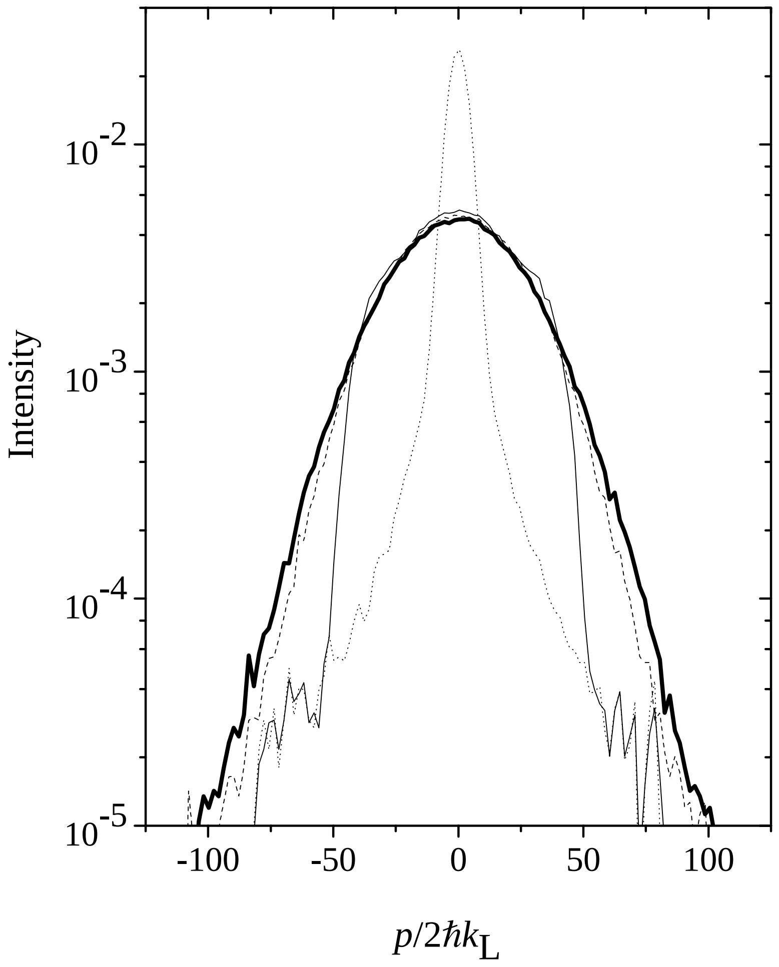

Figure 3.4: Comparison of momentum distributions from classical simulations for different pulse widths after 68 kicks, with $K = 10.5$. The nearly Gaussian initial condition is shown as a dotted line. Notice that even for $\alpha = 0.014$ (dashed), the classical growth is slowed. For $\alpha = 0.049$ (light solid) the initial condition is unaffected outside the boundary. The heavy line is a classical simulation for the δ-kicked rotor. The vertical scale is logarithmic and in arbitrary units.

3.3 Experimental Parameters

The experiments are conducted as described in Chapter 2, with the momentum given in units of $2\hbar k_{\rm L}$. The maximum momentum that we can measure is primarily limited by the size of the CCD detector in our camera. For a 15 ms drift time, we can detect momenta within $|p/2\hbar k_{\rm L}| \approx 80$. Using shorter drift times, we could measure larger momenta at the expense of resolution.

The pulse period was $T = 20\,\mu$s, corresponding to $\bar{k} = 2.08$. The kick strength κ was chosen to provide the best exponentially-localized momentum distributions. For the shortest pulses ($t_{\rm p} = 0.283\ \mu$s) we used $V_0/h = 3.55$ MHz, yielding a classical stochasticity parameter of $K = 13.1$. For the longest pulses ($t_{\rm p} = 1.975\ \mu$s) we used $V_0/h = 0.94$ MHz, corresponding to $K = 24$. The absolute uncertainty in K is ±10%, and the largest contributions are due to the measurement of beam profile and the absolute laser power calibration.

The momentum boundary due to the nonzero pulse width is $|p/2\hbar k_{\rm L}| = 213$ for our typical operating parameters. This value is a factor of four larger than in our group's earlier sodium experiments. The corresponding reduction in the effective value of K is only 6% out to $|p/2\hbar k_{\rm L}| = 40$ and 25% at our maximum detectable momentum of $|p/2\hbar k_{\rm L}| \approx 80$.

We can also estimate the effects of collisions from the experimental work of Dalibard and coworkers [46], who measured a collision cross section of $5 \times 10^{-11}\,\text{cm}^2$ for cesium atoms prepared in the $F = 4$, $m_F = 4$ ground sublevel with a temperature of 5 μK. In our initial distribution, the density is about 10^{11} cm^{-3}, and the mean velocity is 5 cm/s. These figures lead to a collision probability of only 2.5% in 1 ms, or 0.05% per kick period. This result actually overestimates the collision probability because our atoms are distributed among the various m_F sublevels, and so the actual collision cross section is smaller than the figure used here.

3.4 Results

The results presented here illustrate the capabilities of the cesium setup. As a starting point we needed to reproduce dynamical localization in the kicked rotor system. We then used this as a baseline to characterize the effects of the momentum boundary. The resulting momentum distributions are compared with classical simulations.

In Fig. 3.5 we see the time evolution for a typical kicked rotor experiment, from the initial distribution through 68 kicks. The momentum distribution starts out with a Gaussian profile, which makes a rapid transition to a broader, exponential distribution. We observe a continued slow growth in the momentum distribution until the end of the experiment, with the distributions remaining exponential.

An overlay version of five momentum distributions for an experiment with similar parameters, taken at increments of 17 kicks, is shown in Fig. 3.6a. Note that the distribution remains exponential over the nearly three orders of magnitude in intensity that are resolvable in our experiment. The slow growth of the localized distribution is also evident in this figure.

Fig. 3.6 compares experiments using four different pulse widths with the corresponding momentum boundaries as predicted by Eq. (3.1). In the first case, Fig. 3.6a, the boundary of $|p/2\hbar k_\mathrm{L}| = 213$ is three times larger than the $|p/2\hbar k_\mathrm{L}| = 70$ resolvable width of our distribution. This situation is ideal for experimental studies of the quantum kicked rotor, since the momentum distribution remains well within the boundary.

In Fig. 3.6b, we see that although the distance between the boundaries at $|p/2\hbar k_\mathrm{L}| = 125$ is less than twice the width of the final distribution, there is little effect on the shapes of the distributions.

In Fig. 3.6c, the boundary is located at $|p/2\hbar k_\mathrm{L}| = 61$, and it has a

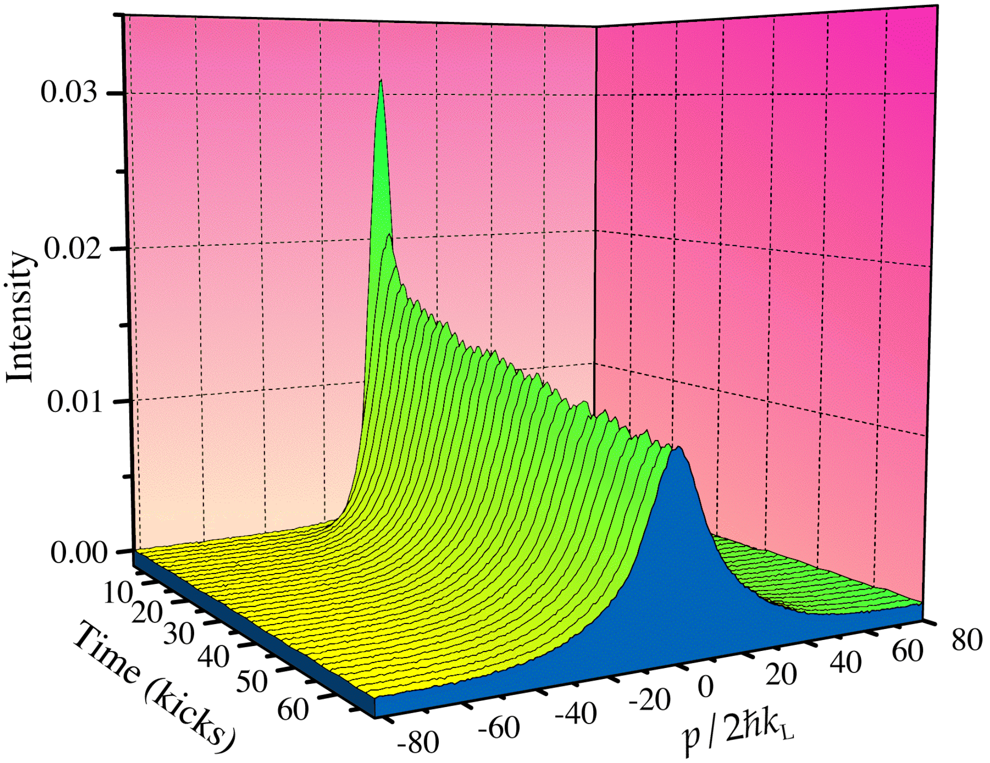

Figure 3.5: Time evolution of a typical kicked rotor experiment for $K = 11.5 \pm 10\%$, $T = 20\,\mu$s, 0.283 μs pulse width, and $k\!\!\!^{-} = 2.08$. The initial distribution is nearly Gaussian with $\sigma_p/2\hbar k_{\rm L} = 4.4$. The final distribution is exponential with a localization length of 13. Note that the vertical axis is linear and in arbitrary units, and the time increment between distributions is 2 kicks.

clear effect on the wings of the distributions. Notice, however, that after 17 kicks the distribution still looks exponential.

Finally, Fig. 3.6d shows a case where the boundary at $|p/2\hbar k_{\rm L}| = 30$ is well within the exponential distributions shown in Fig. 7a. In this case, the distribution quickly reaches the boundary, and the diffusion process halts before quantum localization sets in.

It is also interesting to note that the portions of the initial distributions

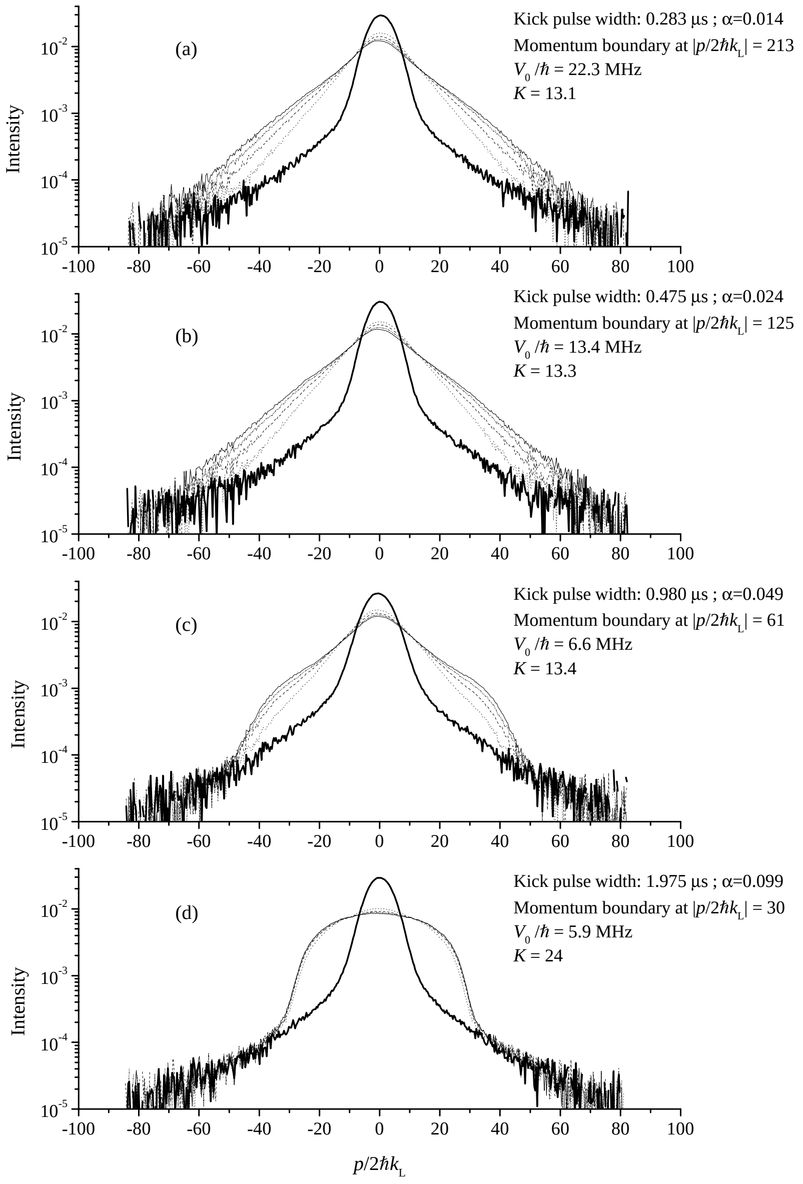

Figure 3.6: Comparison of momentum distribution evolution for 4 different kick pulsewidths from 0.3 μs to 2 μs. Distributions for 5 different times are shown on each graph: 0 kicks (heavy solid line), 17 kicks (dotted), 34 kicks (dashed), 51 kicks (dash-dot), and 62 kicks (solid).

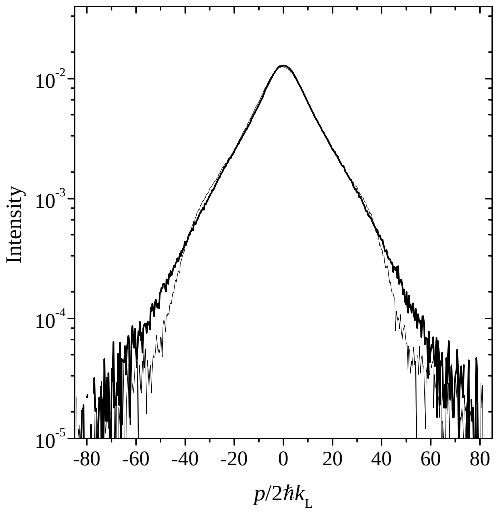

Figure 3.7: Comparison of experimental momentum distributions after 51 kicks for two different pulse widths, $\alpha = 0.014$ (heavy line) and $\alpha = 0.049$ (thin line). In the $\alpha = 0.014$ case, also shown in Fig. 7a, the boundary is at $|p/2\hbar k_{\mathrm{L}}| = 213$. This boundary width is much larger than the width of the distribution, and hence the boundary does not significantly affect the exponential distribution. In the $\alpha = 0.049$ case, also shown in Fig. 7c, the boundary is located at $|p/2\hbar k_{\mathrm{L}}| = 61$. This boundary width is clearly inside the base of the exponential distribution; the momentum distribution is now distorted in its wings, while the shape at the center is nearly identical to the first case. Note that the vertical scale is logarithmic and in arbitrary units.

that are outside the boundary in Figs. 7c and 7d remain stationary. This behavior is a result of the presence of the invariant curves past the boundary, as shown in Fig. 2, that strongly inhibit momentum transport. These observations are consistent with a previous theoretical study of the kicked rotor with finite pulses [47].

The dynamics near the center of the distribution appear to be relatively insensitive to the location of the boundary. Fig. 3.7 compares the distributions after 51 kicks from Figs. 3.6a and 3.6c. It is clear that the portion of the distribution in the central region remains unaffected by the boundary, but

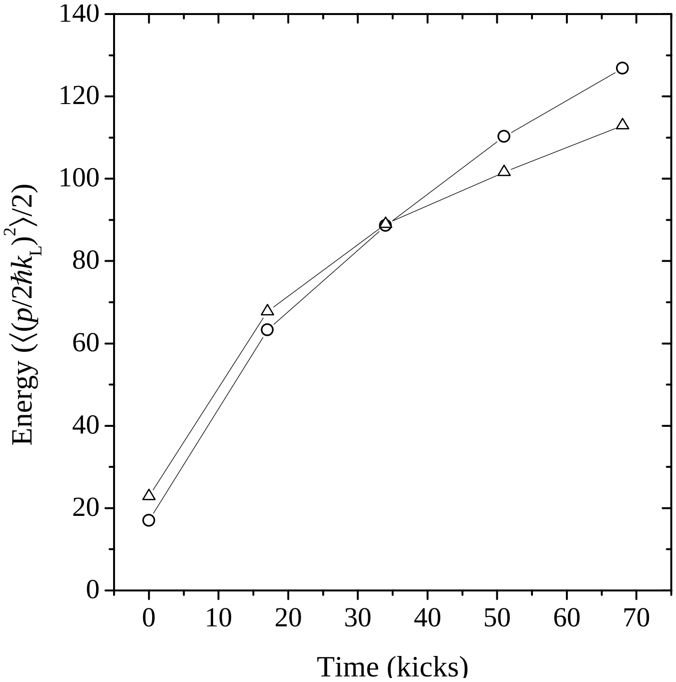

Figure 3.8: Growth of energy with time for the cases in Fig. 8. The momentum boundaries are $|p/2\hbar k_{\mathrm{L}}| = 213$ for the case $\alpha = 0.014$ (circles) and $|p/2\hbar k_{\mathrm{L}}| = 61$ for the case $\alpha = 0.049$ (triangles). Note that the initial growth rate is the same until the distributions diffuse out to larger momenta where K_{eff} begins to drop sharply for the $\alpha = 0.049$ case.

there is substantial deviation between the two cases in the wings of the distributions. Fig. 3.8 shows that the initial energy growth rate is the same for the two boundary locations in Fig. 3.7. It is only as the distribution nears the boundary that further growth is inhibited. This point is significant because much of the theoretical analysis of this system has been done using the long-term diffusion in energy, which is especially sensitive to the high-momentum tails of the distribution.

In Fig. 3.9 we compare the intermediate case of Fig. 3.6c ($\alpha = 0.049$) to the classical simulation shown in Fig. 3.4. The distributions shown correspond to 68 kicks. There are several important features in this comparison. First, the

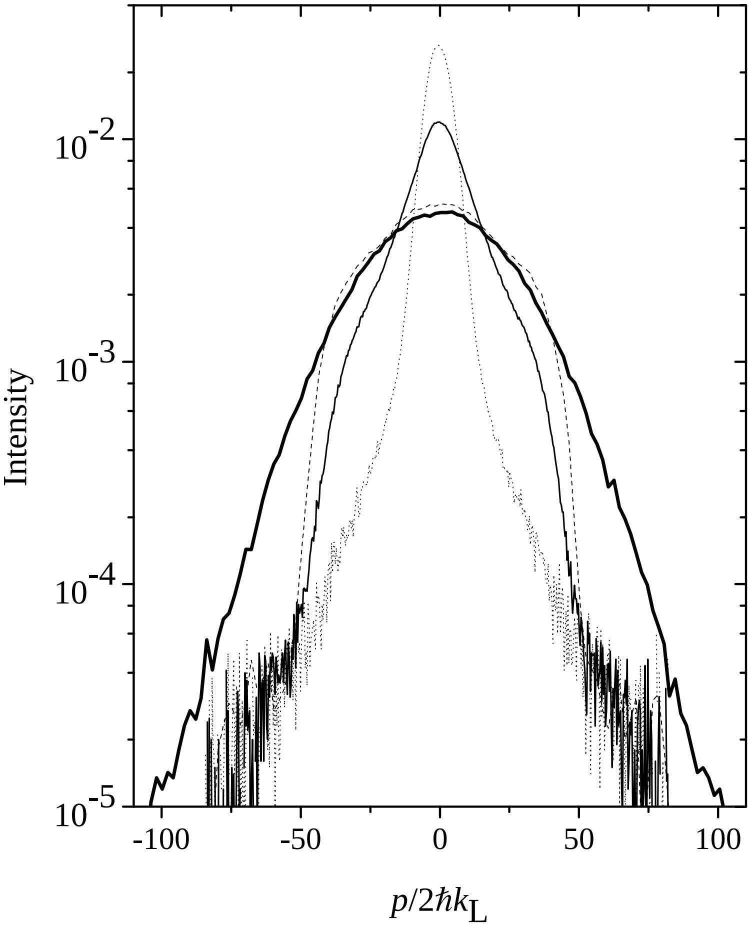

Figure 3.9: Comparison of experimental momentum distributions after 68 kicks to the classical simulations of Fig. 3.4. Both square-pulse cases, the experiment (light solid line) and the simulation (dashed line), have the same pulse width $\alpha = 0.049$ and hence the same boundary, although K is slightly different between the two cases ($K = 11.1$ and 10.5, respectively). The experimental data clearly manifests its quantum nature through a characteristic exponential profile in the central region. The classical square-pulse simulation instead matches the classical δ-kicked rotor simulation (heavy solid line) in the central region. The initial distribution (dotted line) remains unchanged outside the boundary. Note that the vertical scale is logarithmic and in arbitrary units.

classical square-pulse case follows the δ-kick case out to the boundary. Second, the experimental distribution is characteristically exponential near its center, and then it drops off at the boundary as in the classical simulation. Finally, the initial conditions in both the classical simulation and the experiment remain unchanged outside the boundary. Therefore, in the central region, both the classical simulation and the experiment behave as they would in the limit of δ-kicks, displaying classical diffusion and quantum localization, respectively. Their behavior near the boundary, however, is quite similar.

The presence of a boundary in the classical phase space provides a purely classical suppression of momentum diffusion. Recalling the discussion in Section 1.4, one of the requirements to observe dynamical localization was that we need to work in a predominantly chaotic (classical) phase space. If diffusion is suppressed classically by residual stable islands, or by KAM boundaries, identification of the suppression quantum effects would be ambiguous. Likewise, the investigation of any phenomenon that is expected to show enhanced momentum growth from that of a localized distribution requires that there is no fundamental barrier to this growth.

The following chapters address two such topics. The first is to study the effects of noise and dissipation on dynamical localization. The signature in this case is the destruction of localization, with subsequent diffusive growth in momentum [48, 49, 50]. The second is the study of quantum dynamics in a region of classical anomalous diffusion. Here the prediction is that the localization length of the quantum system will increase in correspondence to the enhanced classical diffusion in these regions [16, 51, 52].

Chapter 4

Noise and Dissipation

4.1 Introduction

The role of noise and dissipation in quantum evolution has become an important area of study in recent years. The destruction of quantum interference, referred to as decoherence, is thought to be responsible for the classical nature of the macroscopic world [53]. Decoherence in the context of quantum chaos is particularly intriguing, because it exposes subtle questions about the correspondence limit, and so this topic has been the focus of much theoretical work [32, 48, 49, 50, 54].

On the experimental side, the effects of nonzero temperature on conductance fluctuations in mesoscopic structures [55] and the effects of noise on ionization of Rydberg atoms in microwave fields [28, 56, 57] have been studied. Nevertheless, there remain many open questions, and new experiments on decoherence in quantum chaos are clearly needed. In this chapter we present the results of our initial investigation into the effects of noise and dissipation momentum transport in the quantum kicked rotor. We found that in both cases dynamical localization was destroyed for sufficiently large perturbations, resulting in nearly Gaussian momentum distributions [14].

4.2 Experimental Parameters

We now consider two important modifications to the interaction described in the last chapter. The first is to replace the fixed kick amplitude κ with a random, step-dependent kick amplitude k_n, to introduce *amplitude noise* in the kicks. The second change, carried out in a separate experiment, is to add a weak, resonant interaction that will induce a small number of spontaneous scattering events, primarily between kicks. The latter change introduces *dissipation* into the system.

We introduce amplitude noise with random pulse intensities k_n, which have a uniform distribution on an interval centered about the zero-noise intensity level as depicted in Fig. 4.1. The width of this interval represents the amount of amplitude noise and is given as a percent of this mean level. In the dissipation experiments we introduced a small amount of near-resonant (molasses) light, still detuned by 39 MHz, is leaked into the chamber by AOM1 during the interaction with the pulsed light. We calculated photon scattering rates from the measured intensities based on the assumption that the atoms are illuminated uniformly with all polarizations, so that the result is independent of how the magnetic sublevels are populated. Using this assumption we can use Eq. 2.2 with $I_{\text{sat}} = 2.70$ mW/cm^2 corresponding to a near-resonant beam at the $(6\text{S}_{1/2}, F = 4) \longrightarrow (6\text{P}_{3/2}, F' = 5)$ transition. The intensities used in the experiment were 0, 27, 94, and 246 μW/cm$^2 \pm 20\%$, corresponding to 0%, 1.2%, 5.0%, and 13.0% probability of a spontaneous emission event per kick.

The pulse period for both cases was $T = 20\,\mu$s, corresponding to $\bar{k} = 2.08$. The kick strength κ was again chosen to provide the best exponentially-localized momentum distributions in the zero-noise case. For the amplitude noise data we used $V_0/h = 3.3\,$MHz, corresponding to $K = 12.8$. For the dissipation case we used $V_0/h = 3.12\,$MHz, corresponding to $K = 11.9$. For

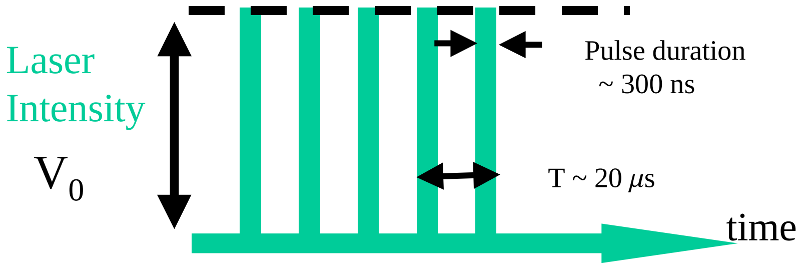

Pulse sequence without noise

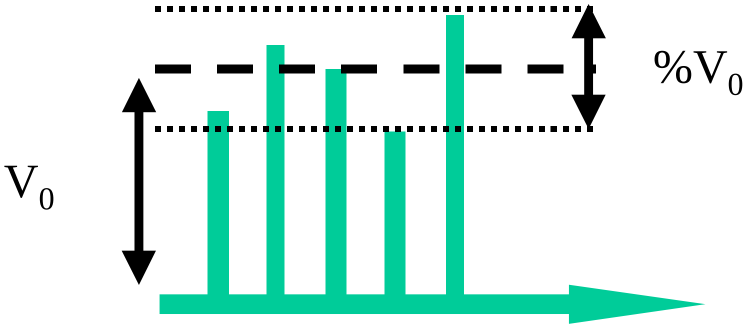

Pulse sequence with amplitude noise

Figure 4.1: Depiction of amplitude noise. The normal pulse sequence on top is altered to produce the noisy sequence shown on the bottom by programming random amplitudes distributed uniformly within the chosen range, $\pm\%V_0/2$. Four different random sequences were done at each time step to obtain an average.

these experiments the reduction in the effective K value was as described in the last chapter. It was only 6% out to $|p/2\hbar k_{\mathrm{L}}| = 40$ and 25% at our maximum detectable momentum of $|p/2\hbar k_{\mathrm{L}}| = 80$.

4.3 Results

We first consider the momentum evolution with no added noise or dissipation, shown in Fig. 4.2(a). The initial distribution is Gaussian except for the pedestal described in Section 2.5. The distribution is also shown at later times, where it takes on the exponential profile characteristic of dynamical localization.

The corresponding growth of energy as a function of time is shown in Fig. 4.3. It is important to note that the calculation of the energy, $\langle p^2 \rangle/2$, from a distribution is highly sensitive to the behavior at large p. For this reason we exclude from the calculation any points below a chosen cutoff, representing the noise floor that dominates at high momenta. Our cutoff level is at 0.25% of the peak value, representing a 400:1 signal-to-noise ratio. We checked the validity of our $\langle p^2 \rangle$ calculation by comparing it to the $\langle p^2 \rangle$ of an exponential fit to our localized distributions. These values typically agree to within 5%.

The energy measurements presented here suffer from a timing problem discovered near the time of this writing. The repump laser had been shutting off during the MOT load time allowing 10% to 20% of the atoms to transfer to the $F = 3$ ground state. These atoms therefore did not interact as strongly with the interaction beam and consequently did not diffuse out as far in momentum. This effect would cause the average energy to be lower by an amount roughly proportional to the amount in the $F = 3$ state. This does not affect the qualitative interpretation of these measurements. Since it did affect the appearance of the momentum distributions, we repeated the measurements to produce the momentum distributions presented here after the problem was remedied [58].

Although the distribution in Fig. 4.2(a) is exponential, we find that as the kicks continue, the sides start to “bulge out.” This continued momentum

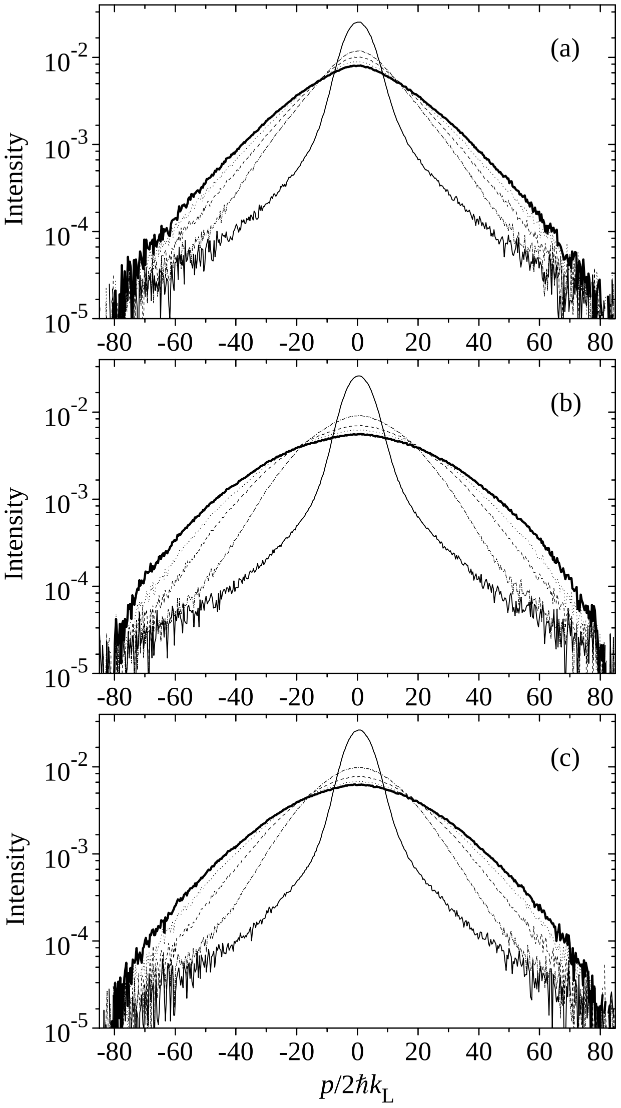

Figure 4.2: Comparison of the momentum distribution evolution for the cases of (a) no noise, (b) 62.5% amplitude noise, and (c) dissipation from 13%/kick spontaneous scattering probability. Time steps shown are 0 kicks (light solid), 17 kicks (dash-dot), 34 kicks (dashed), 51 kicks (dotted), and 68 kicks (heavy solid) for (a) and (c), and 0, 16, 32, 52, and 68 kicks, respectively, for (b). The vertical scale is logarithmic and in arbitrary units.

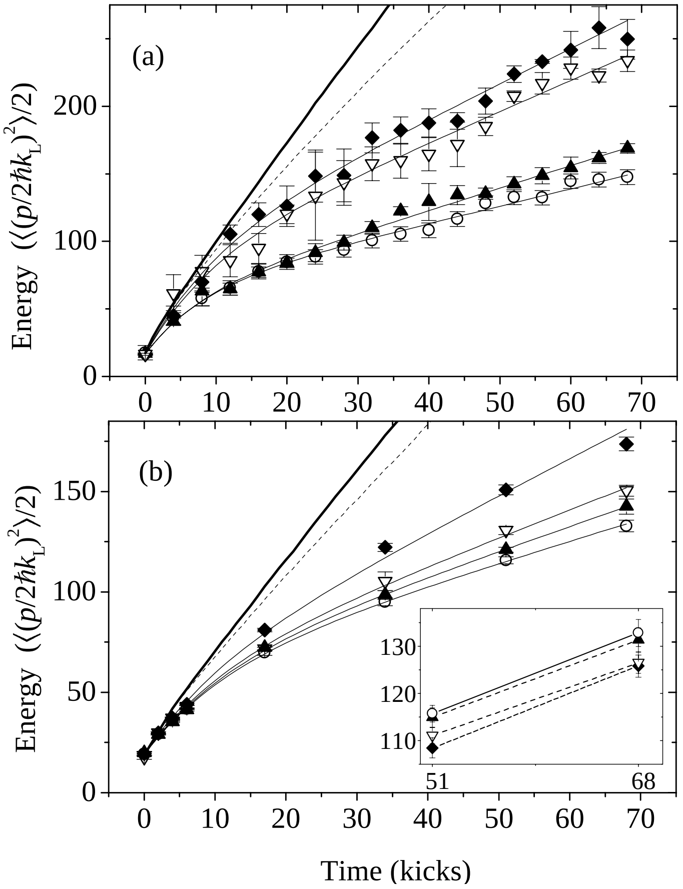

Figure 4.3: Energy vs. time plots for increasing amounts of amplitude noise (a) and spontaneous scattering probability (b). The values for (a) are 0%, 25%, 50%, and 62.5% noise (circles, filled triangles, open triangles, and diamonds, respectively). The values for (b) are 0%, 1.2%, 5.0%, and 13% per kick (circles, filled triangles, open triangles, and diamonds, respectively). Error bars indicate a statistical uncertainty of 1 standard deviation, but do not account for the ±8% systematic uncertainty in the measured energy. Solid lines are curve fits using the model (4.1). Also shown are classical simulations of the δ-kicked rotor (heavy solid line) and the square-pulse kicked rotor (dashed) corresponding to the fit parameters. Inset shows the cooling effect when the molasses beams are added *after* the interaction time (same symbols); the solid line indicates the reference case of no added interaction.

diffusion, also seen in the corresponding plot of the energy growth in Fig. 4.3, may be due to a variety of systematic noise sources mentioned in Section 2.5. For our operating parameters, effects due to the fluctuating dipole force [59] and atom-atom collisions are negligible.

The effects of external noise and dissipation are shown in Fig. 4.2(b,c). In Fig. 4.2(b), noise in the kick amplitude was imposed, with a peak-to-peak deviation of 62.5% about the mean. In Fig. 4.2(c), the probability of spontaneous scattering was 13% per kick, with an absolute uncertainty of 20%. Both cases exhibit clear deviations from the exponential form.

Fig. 4.3(a) displays the growth of energy as a function of time for different noise levels. The data plotted here represents an average over four distinct random kick sequences. Fig. 4.3(b) displays the growth of energy as a function of time for different levels of spontaneous scattering.

To quantify the growth of energy, we analyzed the data in Fig. 4.3 by employing a diffusion model suggested by Cohen [60]

$$D(t) = D_0 \tau \left[\frac{1}{t_{\mathrm{c}}} + \frac{1}{t^*} \exp\left(-\frac{t}{\tau} \right) \right], \tag{4.1}$$

where $\tau^{-1} = {t_{\mathrm{c}}}^{-1} + {t^*}^{-1}$, and fit the data to $E(t) = \int_0^t D(t')dt'$. In this model, D_0 is the initial diffusion rate, t^* is the quantum break time, and t_{c} is the coherence time [32]. We take D_0 and $\ln t_{\mathrm{c}}$ as our fitting parameters, and we make the ansatz $D_0 = t^* \beta^{-1}$, where β is an additional fitting parameter constrained to be the same among the four simultaneous fits to the data sets in each of Figs. 4.3(a) and (b). The initial energy in each fit was constrained to be the average of the zero-kick measurements, which was 16.6 for the amplitude noise data and 19.1 for the spontaneous scattering data. The results of our fits to the data are shown in Table 4.3.

In order to compare our results to the predicted behavior we use some higher order terms to describe the dependence of D on K, rather than simply

Table 4.1: Fit results for the data presented in Fig. 2. Note that the fitting errors were typically around 5% in the noise experiments, and were around 2% in the dissipation experiments. However, these fitting errors do not include the systematic uncertainties discussed in the text.

Amplitude noise			**Spontaneous Scattering**		
Noise level	D_0	$\ln t_c$	Probability	D_0	$\ln t_c$
0%	6.98	3.78	0%	4.61	3.91
25%	7.00	3.45	1.2%	4.70	3.79
50%	9.14	3.65	5.0%	4.82	3.69
62.5%	9.70	3.62	13%	5.19	3.45
$\beta = 1.40$			$\beta = 3.32$		

the quasilinear term given in Eq. (1.37). These terms, and the $\bar{k}$ dependence are discussed in the next chapter. The result is that the fits for $D_0(K) = D_{\mathrm{cl}}[K \sin(\bar{k}/2)/(\bar{k}/2)]$ [16, 32] give $K = 13.8$ and 12.9 for the amplitude noise and spontaneous scattering data, respectively. Here, we have used $D_{\mathrm{cl}}(K) \simeq (K^2/2)(1/2 - J_2(K) + J_2^2(K))$ [61], where J_2 is an ordinary Bessel function. These values for K are within the uncertainty of those determined from the experimental parameters. Also, the fitted values of D_0 are relatively insensitive to the noise level, and the coherence time t_c decreases with increasing noise, except for the two largest amplitude noise cases. In these cases the fitted values for D_0 are anomalously high compared to the case with no noise, and the coherence times are longer than in the 25% case, indicating a breakdown of the fits for large amplitude noise levels. Recall also that these data suffer from the problem of having a fraction in the $F = 3$ state which reduces the average measured energy. This is not accounted for in the fit, but the main purpose of the fit at this point is to demonstrate a qualitative agreement with theory. Future work will attempt to provide better quantitative measurements.

In order to claim that the increased diffusion for the case of spontaneous scattering is due to decoherence, it is essential to characterize the role of recoil heating, which could also lead to momentum diffusion. To address this question experimentally, we measured the effect of turning on the molasses beams *after* the kick sequence instead of during the kick sequence. This measurement was repeated at each level of spontaneous scattering for the same durations as the kick sequences. The results are displayed as an inset of Fig. 4.3(b). We find that the molasses beams produce a weak *cooling* effect that is substantially smaller than the growth seen when they are concurrent with the kicks. Hence, our observations provide clear experimental evidence for decoherence.

Chapter 5

Anomalous Diffusion

5.1 Introduction

In this chapter we consider the effects of small structures of the classical kicked rotor phase space on the global momentum transport in various quantum regimes. One particularly interesting aspect of the kicked rotor system is the existence of *accelerator modes*, which lead to Lévy flights in generic phase-space trajectories [62, 63]. These Lévy flights can have a strong influence on the global transport properties of a system, and have been recently employed in the understanding of a subrecoil laser cooling scheme for atoms [64] and the motion of particles in a nonuniform fluid flow [65]. In the classical kicked rotor, accelerator modes become important in the long-time limit, because they account for a small area in phase space. Our data, however, suggests that they may play a role even in the short time for the quantum case.

This experiment studies the time evolution of atomic momentum distributions as a function of the pulse amplitude and period. We observe the oscillations in the momentum distribution widths that are expected from theory. We also observe that for certain kick amplitudes where accelerator modes are present in the classical phase space, the momentum distributions do not have the expected exponential form over the time scale of our experiment [15]. These results suggest a correlation between classical anomalous diffusion and the observed quantum dynamics.

5.2 Theory and Background

In the scaled units the variations of pulse amplitude and period correspond to variations in the system parameters $K \propto V_0 T$ and $\bar{k} \propto T$. Although the classical phase space is predominantly chaotic for $K > 4$, there are many small stable structures that influence the system dynamics, even for large K values. In particular, when K is near $2\pi j$, where j is a positive integer, there exist stable accelerator modes that result from the periodicity of the phase space in momentum [23]. Note that other smaller accelerator modes exist for other values of K, a number of which have been catalogued by Karney [66]. A trajectory inside one of these accelerator modes changes its momentum by $|\Delta\rho| = 2\pi j$ at each kick. This acceleration ($p(t) \propto 2\pi j t$) manifests itself as a *streaming* behavior along the momentum direction of the phase space.

An example of a phase space containing the largest accelerator modes ($K \approx 2\pi$) is shown in Fig. 5.1 where it is compared to a more generic phase ($K = 10$). The figure shows the phase space extended to several periods in momentum in order to illustrate the effect of the accelerator modes. At $K = 10$ an initial distribution at the bottom of the figure would spread to higher momenta values via diffusion only, a random walk type process. At $K \approx 2\pi$ the figure depicts both the diffusion of the population in the stochastic sea, and the streaming behavior of trajectories starting in accelerator modes as they find themselves kicked to the next higher island in momentum. Fig. 5.1 is a little misleading because at the momentum values of $2\pi j$ of these accelerator modes a trajectory also, of course, moves over j spatial periods before the next kick. Our experiment is not sensitive to spatial movement on the order of even hundreds of standing wave periods.

There are actually two sets of accelerator modes, the set on the left accelerate toward positive momentum, and the set on the right toward negative momentum. Understanding existence of these large accelerator modes at $K =$

$2\pi j$ is intuitively simple if one considers that they are located at $\rho = 2\pi j_\rho$, and $\phi = (\pi/2)(2j_\phi + 1)$, ($j_\rho, j_\phi$ integers). This is where the standing wave has its highest gradient, applying an impulse of the full $\pm 2\pi j$ in momentum at the next kick. Likewise, the momentum of $2\pi j_\rho$ will translate the position by j_ρ spatial periods keeping the trajectory trapped in the accelerator mode. The equations of motion (1.34) for the DKR bear this out directly.

This streaming is not the whole story however. Additionally, trajectories that begin outside the accelerator modes will eventually wander near them and "stick" to their boundary for a finite, but possibly large number of kicks. This is conjectured to be due to the very complicated self-similar structure of the phase space at the boundary of regular orbits [62]. This sticking results in the Lévy-flight-like trajectories mentioned above, where random-walk behavior is interspersed with strings of many correlated steps in the same direction. The suffix *like* is added to include trajectories where the statistics of the flight lengths may not correspond to the strict definition of Lévy-flights given elsewhere [67]. We are more interested in the generic behavior. An example of this type of behavior is shown in the single particle DKR trajectory in Fig. 5.2. This trajectory was initiated in the stochastic region of a phase space containing accelerator modes. Notice that the motion is dominated by a few large flights in momentum. Thus, directly or indirectly, the accelerator modes change the global nature of phase-space transport from diffusion, characterized by random-walk trajectories, to anomalous diffusion, characterized by Lévy-flight trajectories and streaming.

The diffusive behavior is described by a linear growth in energy, $E \equiv \langle (p/2\hbar k_{\mathrm{L}})^2/2 \rangle = Dt$, where D is the diffusion coefficient, whereas anomalous diffusion has a modified dependence $E = Dt^\mu$, where $\mu \neq 1$. A classical calculation of the diffusion coefficient results in a series of time step correlations. The first few of these were calculated by Rechester, Rosenbluth, and White

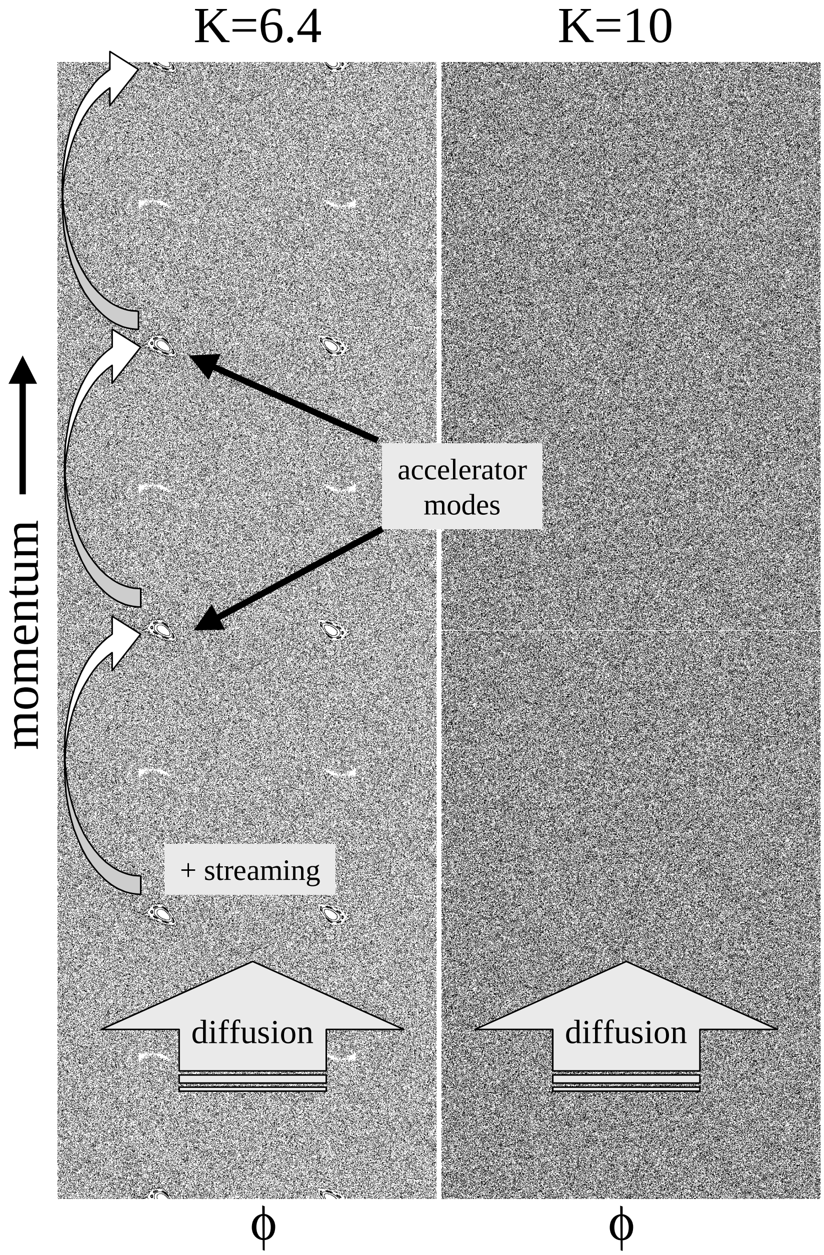
K=6.4
K=10
momentum
accelerator
modes
+ streaming
diffusion
diffusion
ϕ
ϕ

Figure 5.1: DKR surface of sections for $K = 6.4$ and $K = 10$. This figure illustrates size and location of accelerator modes and shows homogeneity of the phase space at $K = 10$.

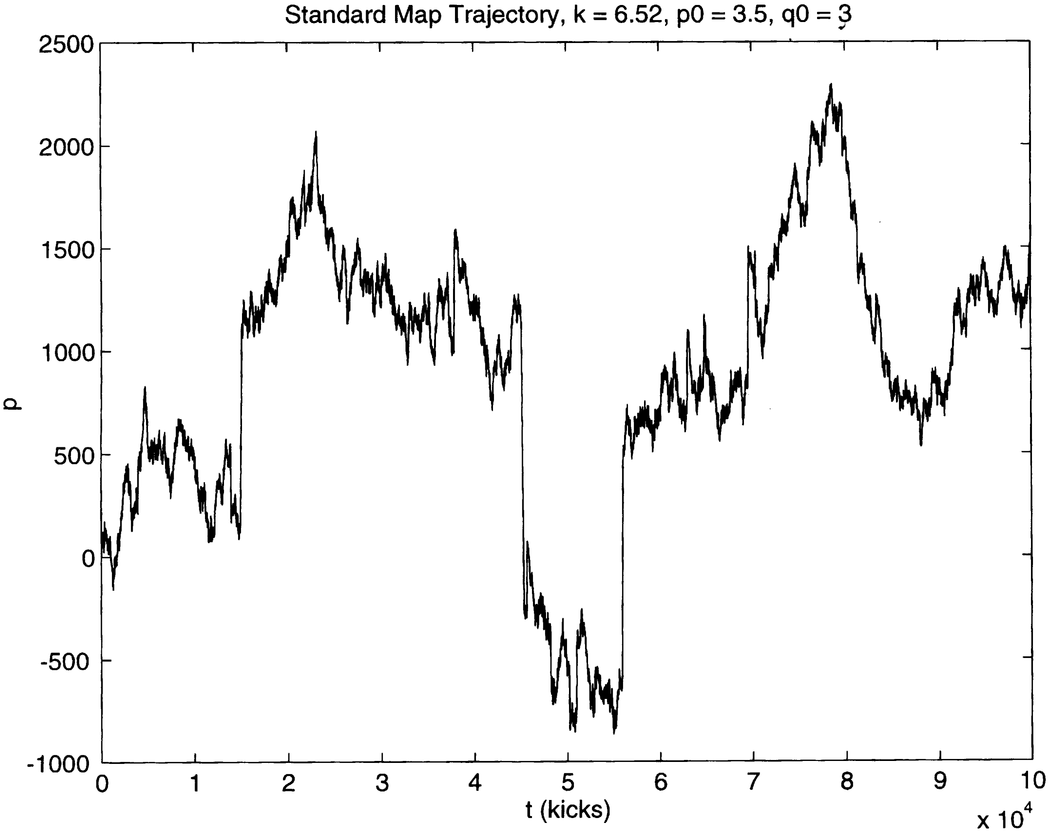

Figure 5.2: Simulation of a single particle DKR trajectory showing Levy flights

and show an oscillatory dependence on K [23, 61],

$$D(K) = \frac{K^2}{2}\left(\frac{1}{2} - J_2(K) + J_2^2(K) + O(K^{-3/2})\right), \tag{5.1}$$

where $J_2(K)$ is an ordinary Bessel function. This function, which is valid both in the absence of accelerator modes and for short times in the presence of accelerator modes, is plotted in Fig. 5.5. The maxima of this function coincide with the existence of the stable accelerator modes. As higher order correlations are added, corresponding to longer times, the dominance of the accelerator modes becomes more apparent where they exist.

Although the DKR is presented as general model for many aspects of chaotic dynamics, accelerator modes are a particular characteristic of the DKR, and only exist because of the periodicity in momentum. It was shown in Chapter 3 that because of the non-zero duration of the pulses used in our experiment, the phase space is not exactly periodic in momentum, and hence our system does not have *true* accelerator modes. However, our system has "quasiaccelerator modes" [23], which behave like accelerator modes over a bounded region of phase space. A graph of a classical simulation, including finite pulses, is shown in Fig. 5.3 in comparison to the approximation in Eq. (5.1). This demonstrates the effect that the pulsewidth used in our experiment is expected have on the oscillations in the momentum diffusion.

The quantum mechanical case, which applies to our experiment, exhibits behavior that is quite different from the classical case. In contrast to the long-time diffusion or super-diffusion of the classical case, the quantum system diffuses for only a short time and then stops when the momentum distribution reaches a characteristic exponential form [10]. Shepelyansky has predicted that the initial quantum diffusion rate D_0, and hence the characteristic length l of the localized distributions (the "localization length"), follows the classical case when K is replaced by K_q, with [16, 32]

$$K_\mathrm{q} = K\left(\frac{2}{k\!\!\!{}^{-}}\right)\sin\left(\frac{k\!\!\!{}^{-}}{2}\right). \tag{5.2}$$

In this case $D_0(K) = D(K_\mathrm{q})/k\!\!\!{}^{-2}$ and $l = 2\beta D_0$, where β has been determined to be $\sim$1/2 via numerical simulations [16]. Notice that the zero-crossings of (5.2) for integer $k\!\!\!{}^{-}/2\pi$ correspond to *quantum resonances*, where a plane wave at $p = 0$ undergoes ballistic growth in momentum, and exponential localization does not occur [10].

The quantum dynamics of the kicked rotor in the presence of accelerator modes has been studied theoretically by Hanson, Ott, and Antonsen [52]. In this work, the authors observed that any population contained within an

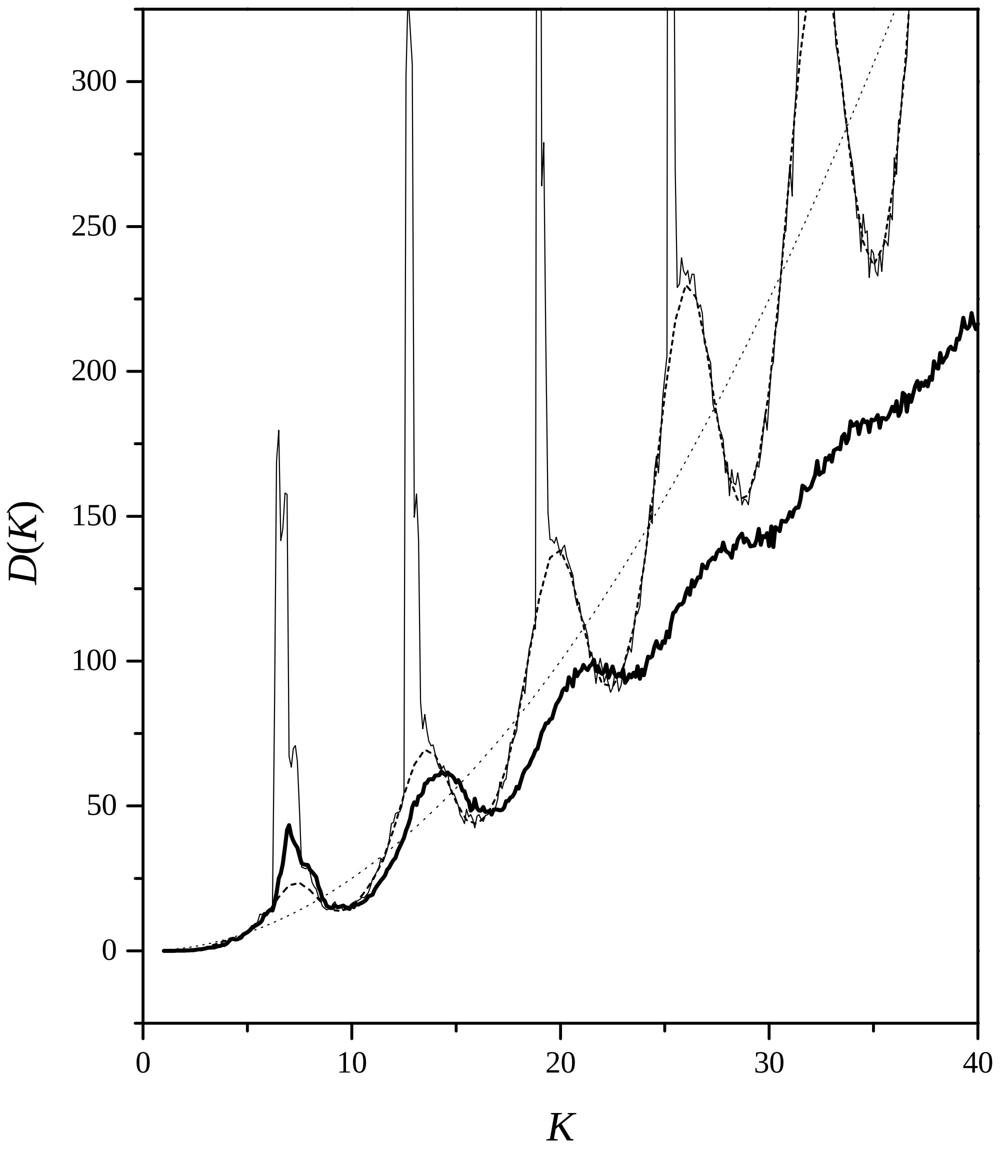

Figure 5.3: Comparison of D(K) as determined by theory versus classical simulations. Theoretical curves include the quasi-linear approximation (dotted) and the Rechester *et al.* curve from Eq. 5.1 (dashed). Simulations are shown for the DKR (light solid), and finite pulse kicked rotor with $\alpha = .014$ (bold solid). Both simulations take the average diffusion after 50 kicks.

accelerator mode would decay exponentially due to tunneling, and they developed a model for global momentum transport in the presence of accelerator modes. However, their simulations used small values of $ƛ$, typically an order of magnitude smaller than those used in our experiment. A more recent theoretical investigation by Sundaram and Zaslavsky [68] focused on values of $ƛ$ comparable to those used in our experiment as well as smaller values. In this work, the authors found evidence that accelerator modes enhance fluctuations in the localization length of the quasienergy states.

5.3 Experimental Parameters

This experiment was run like the boundary experiments except that instead of varying the pulse width and number of kicks, we varied the pulse period and kick amplitude. For the experiments presented here the pulse period was varied from $T = 10$ to 60 μs, corresponding to the range $\bar{k} \sim 1$ to 2π, with less than 4 ns variation per pulse period. The pulse width was fixed at 283 ns and the number of kicks for a given run was generally set at 35. Two special cases used values of 24 and 28 kicks, as described in Fig. 5.5.

As in the noise experiment, our energy data suffers from a systematic reduction due to a fraction of atoms in the $F = 3$ ground state. For the energy data in Fig. 5.5, the $F = 3$ ground state is again around 10-20% populated; however, this mixed population leads only to a systematic reduction in the measured energy (on the order of 10-20%), and does not affect the locations of the observed peaks. This energy data has additional systematic uncertainties of as much as 20-30% due to the high K values used in some cases. These worst-case errors correspond to measurements where $K_{\mathrm{q}} > 15$, since the distribution tails reach the edge of our detection system. This again contributes to an underestimate of the true energy.

The momentum distributions, as opposed to the energy measurments in Fig. 5.5, were accomplished as in Chapter 4 by turning off the repump laser light 100 μs after the trapping laser light. This ensured that all of the atoms were in the $F = 4$ state at the beginning of the interaction.

5.4 Results

A typical exponentially localized momentum distribution for $K_{\mathrm{q}} = 9.1$ is shown in Fig. 5.4(a). This distribution is what one would expect for dynamical localization. Fig. 5.4(b), which corresponds to $K_{\mathrm{q}} = 7.9$, shows a typical example of the observed distributions that are clearly not exponential. We observe the exponential distributions near the minima of the $D(K_{\mathrm{q}})$ function from Eqs. (5.1, 5.2), while nonexponential distributions like that of Fig. 5.4(b) occur near the maxima. Also, in the case of Fig. 5.4(b), it is interesting to note that the momentum distribution at short and intermediate times grows significantly more quickly than in the exponentially localizing case of Fig. 5.4(a). This behavior is especially evident from the "shoulders" on the distribution in Fig. 5.4(b) after 10 kicks, which are absent in the corresponding distribution in Fig. 5.4(a).

In order to observe the oscillations of the distribution widths versus K_{q}, we measured the distribution energies after 35 kicks as a function of K for several different values of $\bar{k}$. We note that although the theory is given in terms of localization length l, the presence of nonexponential distributions at the maxima of $D(K_{\mathrm{q}})$ make meaningful fits of the localization length questionable. However, the distribution energy E scales as l^2, so the energy is a sensible measure of the momentum distributions for comparison with theory. The results are shown in Fig. 5.5, where the energy is plotted against K_{q}. The classical diffusion curve from Eq. (5.1) is also shown for comparison. Because the maxima of the energy curves match for the different $\bar{k}$ cases, these data show that these classical oscillations are present in the quantum kicked rotor and closely match the estimated quantum scaling factor in Eq. (5.2). The data in Fig. 5.5 that is "bunched" near $K_{\mathrm{q}} = 0$ corresponds to $\bar{k} = 6.24$, which is near the quantum resonance. In this case, as in our earlier work [10], we observe little growth in these momentum distributions. We also note that one

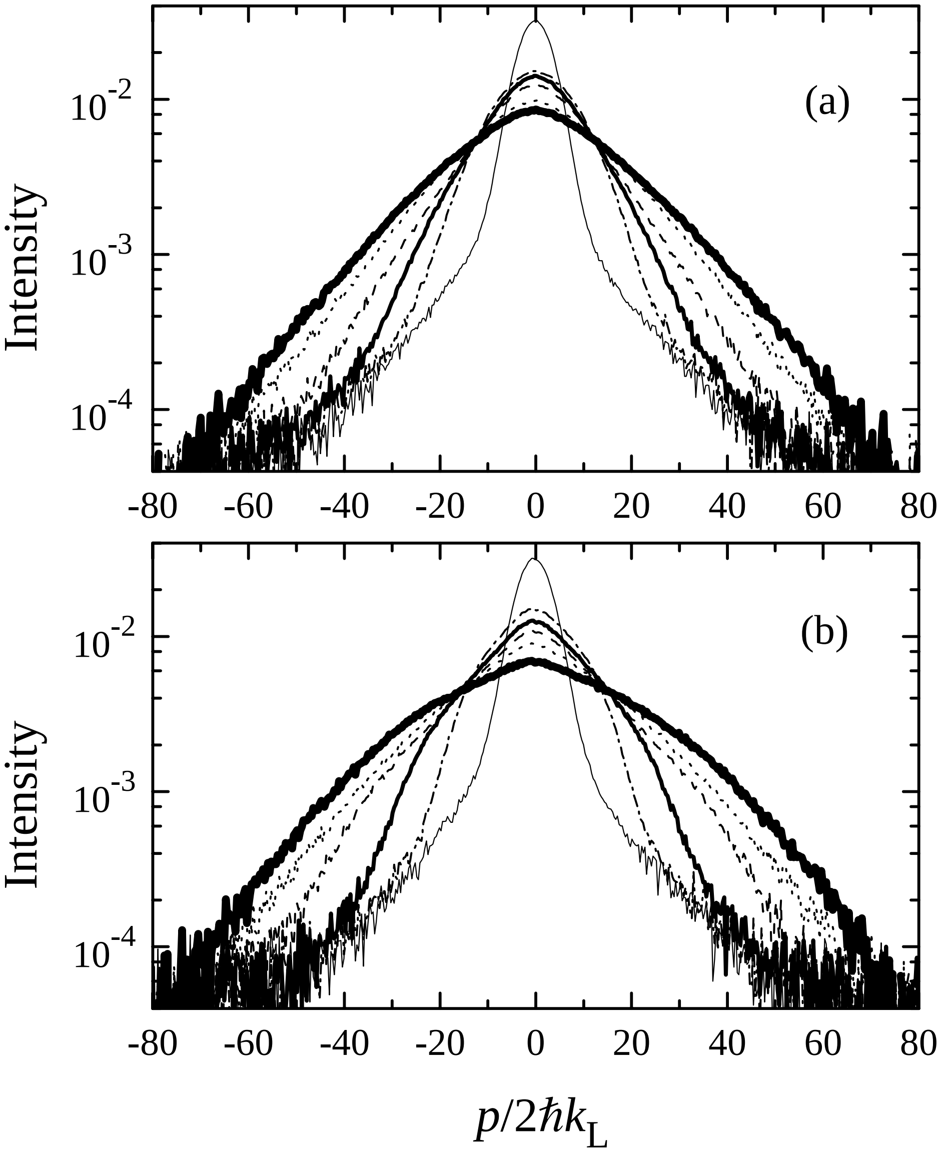

Figure 5.4: Comparison of the momentum distribution evolution with $\bar{k} = 2.08$ for the cases (a) $K_\mathrm{q} = 9.1$, (b) $K_\mathrm{q} = 7.9$. Time steps shown are 0 kicks (light solid), 5 kicks (dash-dot), 10 kicks (bold), 20 kicks (dashed), 45 kicks (dotted), and 70 kicks (heavy bold). The vertical scale is logarithmic and in arbitrary units.

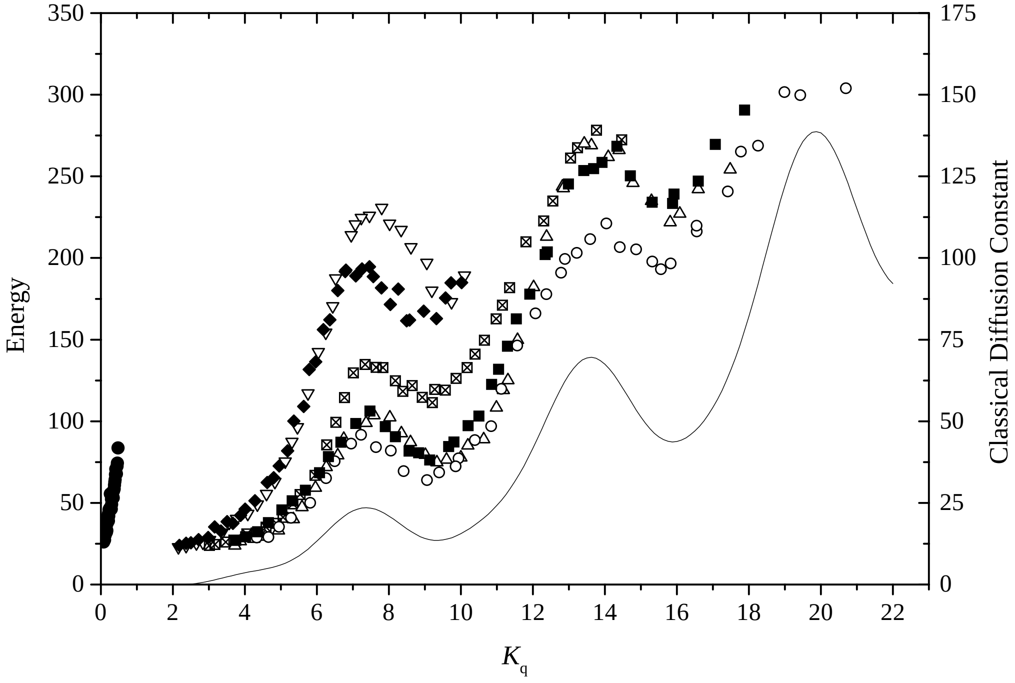

Figure 5.5: Oscillations in the growth of energy as a function of K_q for various values of $\bar{k}$. Data shows the average energy after 35 kicks for the cases $\bar{k} = 1.04$ (inverted triangles), 1.56 (crossed squares), 2.08 (triangles), 3.12 (open circles), 4.16 (filled squares); 28 kicks for $\bar{k} = 5.20$ (filled diamonds); and 24 kicks for $\bar{k} = 6.24$ (filled circles). The solid line is a plot of Eq. (3), the classical energy diffusion rate, showing the peaks related to anomalous diffusion. The correspondence of energy growth in the quantum case to the classical diffusion constant is consistent for all values of $\bar{k}$, supporting the validity of the scaling of the quantum kick strength K_q.

may expect the energy data to have an overall growth as K_q^4 because, as noted above, the localization length l grows as K_q^2. However, we do not observe this scaling behavior in our experiment, and in fact our data has a similar overall growth to that of $D(K_q)$, which grows as K_q^2. This observed behavior is partly a result of the nonzero duration of our pulses, which inhibits momentum transport at large momenta and hence reduces the energies measured at larger K_q as shown in Fig. 5.3. Additionally, the reduction in the measured energy due to the $F = 3$ population problem will be largest for the widest distributions (i.e., the highest energy values).

In conclusion, we have studied quantum transport in the quantum kicked rotor. We have observed the oscillatory dependence of the average energy growth on the kick strength and period. To our knowledge, this is the first experimental observation of these periodic variations in momentum transport in this system and the first experimental confirmation of the predicted quantum scaling of K. While the dependence of energy growth on K and $\hbar\!\!\!/$ is in good qualitative agreement with theoretical expectations, the observed deviation of the momentum distributions for certain intervals in K from their expected, exponentially localized form was both surprising and interesting. We hope that this work will stimulate better theoretical understanding of the momentum distributions in the quantum kicked rotor.

Bibliography

[1] P. L. Gould, A. Ruff, and D. E. Pritchard, "Diffraction of atoms by light: The near-resonant Kapitza-Dirac effect," *Phys. Rev. Lett.* **56**, 827 (1986).

[2] C. Salomon, J. Dalibard, A. Aspect, H. Metcalf, and C. Cohen-Tannoudji, "Channeling atoms in a laser standing wave," *Phys. Rev. Lett.* **59**, 1659 (1987).

[3] P. L. Gould, B. G. Oldaker, A. H. Miklich, and D. E. Pritchard, "Diffraction of atoms moving through a standing light wave," *Phys. Rev. A* **36**, 2495 (1992).

[4] P. J. Martin, B. G. Oldaker, A. H. Miklich, and D. E. Pritchard, "Bragg scattering of atoms from a standing light wave," *Phys. Rev. Lett.* **60**, 515 (1988).

[5] R. Graham, M. Schlautmann, and P. Zoller, "Dynamical localization of atomic-beam deflection by a modulated standing light wave," *Phys. Rev. A* **45**, R19 (1992).

[6] F. L. Moore, J. C. Robinson, C. Bharucha, P. E. Williams, and M. G. Raizen, "Observation of dynamical localization in atomic momentum transfer: A new testing ground for quantum chaos," *Phys. Rev. Lett.* **73**, 2974 (1994).

[7] John Charles Robinson, *Atom Optics, A New Testing Ground for Quantum Chaos*, Ph.D. Dissertation, University of Texas at Austin (1995).

[8] Cyrus Farrokh Bharucha, *Experiments in Dynamical Localization of Ultra-Cold Sodium Atoms Using Time-Dependent Optical Potentials*, Ph.D. Dissertation, University of Texas at Austin (1997).

[9] J. C. Robinson, C. Bharucha, F. L. Moore, R. Jahnke, G. A. Georgakis, Q. Niu, M. G. Raizen, and Bala Sundaram, "Study of quantum dynamics in the transition from classical stability to chaos," *Phys. Rev. Lett.* **74**, 3963 (1995).

[10] F. L. Moore, J. C. Robinson, C. Bharucha, Bala Sundaram, and M. G. Raizen, "Atom optics realization of the quantum-kicked rotor," *Phys. Rev. Lett.* **75**, 4598 (1995).

[11] J. C. Robinson, C. F. Bharucha, K. W. Madison, F. L. Moore, Bala Sundaram, S. R. Wilkinson, and M. G. Raizen, "Can a single-pulse standing wave induce chaos in atomic motion?" *Phys. Rev. Lett.* **76**, 3304 (1996).

[12] Kirk William Madison, *Quantum Transport in Optical Lattices*, Ph.D. Dissertation, University of Texas at Austin (1998).

[13] B. G. Klappauf, W. H. Oskay, D. A. Steck, and M. G. Raizen, "Quantum chaos with cesium atoms: pushing the boundaries," To appear in *Physica D*.

[14] B. G. Klappauf, W. H. Oskay, D. A. Steck, and M. G. Raizen, "Observation of noise and dissipation effects on dynamical localization," *Phys. Rev. Lett.* **81**, 1203 (1998).

[15] B. G. Klappauf, W. H. Oskay, D. A. Steck, and M. G. Raizen, "Experimental study of quantum dynamics in a regime of classical anomalous diffusion," *Phys. Rev. Lett.* **81**, 1 (1998).

[16] D. L. Shepelyansky, "Localization of diffusive excitation in multi-level systems," *Physica D* **28**, 103 (1987).

[17] C. Cohen-Tannoudji and W. D. Phillips, "New mechanisms for laser cooling," *Phys. Today* **43**, 33 (1990).

[18] Steven Chu, "Laser manipulation of atoms and particles," *Science* **253**, 861 (1991).

[19] Patrick Russsell Morrow, *Quantum Tunneling of Atoms in an Optical Potential*, Ph.D. Dissertation, University of Texas at Austin (1997).

[20] Daniel A. Steck, "Atomic motion in a standing wave of far-detuned light," unpublished (Oct. 1998).

[21] Daniel A. Steck, "Cesium D_2 line data," unpublished (Aug. 1998).

[22] Robert C. Hilborn, *Chaos and Nonlinear Dynamics, An Introduction for Scientists and Engineers* (Oxford University Press, 1994).

[23] A. J. Lichtenberg and M. A. Lieberman, *Regular and Chaotic Dynamics*, vol. 38 of *Applied Mathematical Sciences* (Springer-Verlag, 1992), 2nd ed.

[24] Alfredo M. Ozorio de Almeida, *Hamiltonian Systems: Chaos and Quantization* (Cambridge University Press, 1992).

[25] R. Blümel and W. P. Reinhardt, *Chaos in Atomic Physics* (Cambridge University Press, 1997).

[26] G. Casati, B. V. Chirikov, J. Ford, and F. M. Izrailev, "Stochastic behavior of a quantum pendulum under a periodic perturbation," in *Stochastic Behaviour in Classical and Quantum Hamiltonian Systems*, G. Casati and J. Ford, eds., no. 93 in Lecture Notes in Physics, 334 (Springer, New

York, 1979). Earliest published investigation of dynamics of quantum kicked rotor.

[27] J. E. Bayfield and P. M. Koch, “Multiphoton ionization of highly excited hydrogen atoms,” *Phys. Rev. Lett.* **33**, 258 (1974).

[28] R. Blümel, R. Graham, L. Sirko, U. Smilansky, H. Walther, and K. Yamada, “Microwave excitation of Rydberg atoms in the presence of noise,” *Phys. Rev. Lett.* **62**, 341 (1989).

[29] Shmuel Fishman, D. R. Grempel, and R. E. Prange, “Chaos, quantum recurrences, and Anderson localization,” *Phys. Rev. Lett.* **29**, 509 (1982).

[30] J. Bellissard and A. Barelli, “Dynamical localization mathematical framework,” in *Quantum Chaos - Quantum Measurement*, P. Cvitanovic, I. Percival, and A. Wirzba, eds., NATO ASI, 105 (Kluwer Academic Publishers, Dordrecht, Netherlands, 1992).

[31] Shmuel Fishman, “Quantum localization,” Tech. rep., Lecture Notes for the 44th Scottish Universities Summer School in Physics on Quantum Dynamics of Simple Systems, Stirling, Scotland (1994).

[32] Doron Cohen, “Localization, dynamical correlations, and the effect of colored noise on coherence,” *Phys. Rev. A* **44**, 2292 (1991).

[33] B. Chirikov, F. M. Izrailev, and D.L. Shepelyansky, “Dynamical stochasticity in classical and quantum mechanics,” *Sov. Sci. Rev C* **2**, 209 (1981).

[34] B. V. Chirikov, “A theory of quantum diffusion localization,” *Chaos* **1**, 95 (1991).

[35] J. E. Bayfield, G. Casati, I. Guarneri, and D. W. Sokol, “Localization of classically chaotic diffusion for hydrogen atoms in microwave fields,” *Phys. Rev. Lett.* **63**, 364 (1989).

[36] E. J. Galvez, B. E. Sauer, L. Moorman, P. M. Koch, and D. Richards, “Microwave ionization of H atoms: Breakdown of classical dynamics for high frequencies,” *Phys. Rev. Lett.* **61**, 2011 (1988).

[37] Carl E. Wieman and Leo Hollberg, “Using diode lasers for atomic physics,” *Rev. Sci. Instrum.* **62**, 1 (1991).

[38] K. B. MacAdam, A. Steinbach, and Carl E. Wieman, “A narrow-band tunable diode laser system with grating feedback, and a saturated absorption spectrometer for Cs and Rb,” *Am. J. Phys.* **60**, 1098 (1992).

[39] Patrick McNicholl and Harold J. Metcalf, “Synchronous cavity mode and feedback wavelength scanning in dye laser oscillators with gratings,” *Applied Optics* **24**, 2757 (1985).

[40] M. de Labachelerie, H. Sasada, and G. Passedat, “Mode-hop suppression of Littrow grating-tuned lasers: erratum,” *Applied Optics* **33**, 3817 (1994).

[41] Martin Christian Fischer, *Design and Performance of a Ring Dye Laser*, Master’s thesis, University of Texas at Austin (1993).

[42] T. W. Hänsch and B. Couillaud, “Laser frequency stabilization by polarization spectroscopy of a reflecting reference cavity,” *Optics Comm.* **35**, 441 (1980).

[43] C. Salomon, J. Dalibard, W. D. Phillips, A. Clairon, and S. Guellati, “Laser cooling of cesium atoms below 3 μK,” *Europhys. Lett.* **12**, 683 (1990).

[44] J. Dalibard and C. Cohen-Tannoudji, "Laser cooling below the doppler limit by polarization gradients: simple theoretical models," *J. Opt. Soc. Am. B* **6**, 2023 (1989).

[45] R. Graham and A. R. Kolovsky, "Dynamical localization for a kicked atom in two standing waves," *Phys. Lett. A* **222**, 47 (1996).

[46] M. Arndt, M. Ben Dahan, D. Guéry-Odelin, M. W. Reynolds, and J. Dalibard, "Observation of a zero-energy resonance in cs-cs collisions," *Phys. Rev. Lett.* **79**, 625 (1997).

[47] R. Blümel, S. Fishman, and U. Smilansky, "Excitation of molecular rotation by periodic microwave pulses. a testing ground for Anderson localization," *J. Chem. Phys.* **84**, 2604 (1986).

[48] E. Ott, T. M. Antonsen, and J. D. Hanson, "Effect of noise on time-dependent quantum chaos," *Phys. Rev. Lett.* **53**, 2187 (1984).

[49] T. Dittrich and T. Graham, "Quantum effects in the steady state of the dissipative standard map," *Europhys. Lett.* **4**, 263 (1987).

[50] S. Fishman and D. L. Shepelyanski, "Manifestation of localization in noise-induced ionization and dissociation," *Europhys. Lett.* **16**, 643 (1991).

[51] D. L. Shepelyanski, "Localization of quasienergy eigenfunctions in action space," *Phys. Rev. Lett.* **56**, 677 (1986).

[52] J. D. Hanson, E. Ott, and T. M. Antonsen, "Influence of finite wavelength on the quantum kicked rotator in the semiclassical regime," *Phys. Rev. A* **29**, 819 (1984).

[53] W. H. Zurek, "Decoherence and the transition from quantum to classical," *Phys. Today* **44**, 36 (1991).

[54] S. Dyrting and G. J. Milburn, "Dissipative nonlinear quantum dynamics in atomic optics," *Phys. Rev. A* **51**, 3136 (1995).

[55] R. M. Clarke, I. H. Chan, C. M. Marcus, C. I. Duruöz, J. S. Harris, Jr., K. Campman, and A. C. Gossard, "Temperature dependence of phase breaking in ballistic quantum dots," *Phys. Rev. B* **52**, 2656 (1995).

[56] M. Arndt, A. Buchleitner, R. N. Mantegna, and H. Walther, "Experimental study of quantum and classical limits in microwave ionization of rubidium rydberg atoms," *Phys. Rev. Lett.* **67**, 2435 (1991).

[57] L. Sirko, M. R. W. Bellermann, A. Haffmans, P. M. Koch, and D. Richards, "Probing quantal dynamics of mixed phase space systems with noise," *Phys. Rev. Lett.* **71**, 2895 (1993).

[58] B. G. Klappauf, W. H. Oskay, D. A. Steck, and M. G. Raizen, "Erratum: Observation of noise and dissipation effects on dynamical localization, *Phys. Rev. Lett.* **81**, 1203 (1998)," Submitted to Phys. Rev. Lett.

[59] J. P. Gordon and A. Ashkin, "Motion of atoms in a radiation trap," *Phys. Rev. A* **21**, 1606 (1980).

[60] Doron Cohen (private communication).

[61] A. B Rechester, M. N. Rosenbluth, and R. B. White, "Fourier-space paths applied to the calculation of diffusion for the Chirikov-Taylor model," *Phys. Rev. A* **23**, 2664 (1981).

[62] G. M. Zaslavsky, M. Edelman, and B. A. Niyazov, "Self-similarity, renormalization, and phase space nonuniformity of Hamiltonian chaotic dynamics," *Chaos* **7**, 159 (1997).

[63] Joseph Klafter, Michael F. Schlesingerd, and Gert Zumofen, "Beyond brownian motion," *Phys. Today* **49**, 33 (1996).

[64] F. Bardou, J. P. Bouchaud, A. Aspect O. Emile, and C. Cohen-Tannoudji, "Subrecoil laser cooling and Lévy flights," *Phys. Rev. Lett.* **72**, 203 (1994).

[65] T. H. Solomon, E. R. Weeks, and H. L. Swinney, "Observation of anomalous diffusion and Lévy flights in a two-dimensional rotating flow," *Phys. Rev. Lett.* **71**, 3975 (1993).

[66] F. F. Karney, A. B. Rechester, and R. B. White, "Effect of noise on the standard mapping," *Physica D* 425 (1982).

[67] Eric R. Weeks, *Experimental studies of Anomalous Diffusion, Blocking Phenomena, and Two-dimensional Turbulence*, Ph.D. Dissertation, University of Texas at Austin (1997). Contains a nice description of Lévy-flight statistics and their role in many physical systems.

[68] Bala Sundaram and G. M. Zaslavsky, "Anomalous transport and quantum-classical correspondence," Submitted for publication.

Vita

Bruce George Klappauf was born to Leonard and Jeanette Klappauf in Greenbay, Wisconsin on April 2, 1961. After graduating from J. I. Case High School in Racine, Wisconsin, he started at a local university, the University of Wisconsin Parkside. Three years later he transferred to the University of Wisconsin at Madison where he completed Bachelor's degrees in Mathematics and Physics in 1984. He then joined the Air Force as a Second Lieutenant, earning his wings as a Navigator, and being assigned to fly as an Electronic Warfare Officer in the backseat of the F4-G Phantom II, Wild Weasel aircraft. After 5 years in Europe, 6 months in the Persian Gulf, and nearly 1000 hours of flying time he was selected to earn an Air Force Master's degree in Engineering Physics at the Air Force Institute of Technology, Wright-Patterson AFB, Ohio. In 1993, one year into the program, he separated from the Air Force and began a doctoral program in physics at the University of Texas at Austin, where he completed the work presented here.

Permanent address: 7205 John Blocker Dr.
Austin, Texas 78749

This dissertation was typeset with LaTeX[‡] by the author.

[‡] LaTeX is a document preparation system developed by Leslie Lamport as a special version of Donald Knuth's TeX Program.